



UNIVERSIDADE FEDERAL DE SANTA CATARINA  
CENTRO TECNOLÓGICO  
PROGRAMA DE PÓS-GRADUAÇÃO EM ENGENHARIA MECÂNICA

Rodrigo Cavalcanti Alvarez

**THERMAL AND HYDRAULIC ANALYSIS OF A DIFFUSION-BONDED  
HEAT EXCHANGER**

FLORIANÓPOLIS

2021

Rodrigo Cavalcanti Alvarez

**THERMAL AND HYDRAULIC ANALYSIS OF A DIFFUSION-BONDED HEAT  
EXCHANGER**

Dissertação submetido(a) ao Programa de Pós-Graduação em Engenharia Mecânica da Universidade Federal de Santa Catarina para a obtenção do título de Mestre em Engenharia Mecânica

Orientador: Profa. Dra. Marcia B. H. Mantelli

Florianópolis

2021

Ficha de identificação da obra elaborada pelo autor,  
através do Programa de Geração Automática da Biblioteca Universitária da UFSC.

Cavalcanti Alvarez, Rodrigo  
Thermal and hydraulic analysis of a diffusion-bonded  
heat exchanger / Rodrigo Cavalcanti Alvarez ; orientadora,  
Marcia Barbosa Henriques Mantelli, 2021.  
123 p.

Dissertação (mestrado) - Universidade Federal de Santa  
Catarina, Centro Tecnológico, Programa de Pós-Graduação em  
Engenharia Mecânica, Florianópolis, 2021.

Inclui referências.

1. Engenharia Mecânica. 2. Trocador de Calor Unido por  
Difusão. 3. Desempenho térmico e hidráulico. 4. Correlação  
de número de Nusselt. 5. Correlação de fator de Atrito de  
Fanning. I. Barbosa Henriques Mantelli, Marcia. II.  
Universidade Federal de Santa Catarina. Programa de Pós  
Graduação em Engenharia Mecânica. III. Título.

Rodrigo Cavalcanti Alvarez

**THERMAL AND HYDRAULIC ANALYSIS OF A DIFFUSION-BONDED HEAT  
EXCHANGER**

O presente trabalho em nível de mestrado foi avaliado e aprovado por banca  
examinadora composta pelos seguintes membros:

Prof. Marcos Rojas-Cárdenas, Dr.  
Institut National des Sciences Appliquées de Toulouse

Prof. Emilio Ernesto Paladino, Dr.  
Universidade Federal de Santa Catarina

Certificamos que esta é a **versão original e final** do trabalho de conclusão que foi  
julgado adequado para obtenção do título de mestre em Engenharia Mecânica.

---

Prof. Paulo de Tarso Rocha de Mendonça, Dr  
Coordenador do Programa de Pós Graduação

---

Prof. Marcia B. H. Mantelli, Dra.  
Orientadora

Florianópolis, 2021.

*To my family.*

## ACKNOWLEDGEMENTS

Firstly, I would like to express my gratitude to my advisor, Prof. Marcia B. H. Mantelli, for welcoming me as a Master's student at her research group, for her technical support and especially for the opportunities given me during my research activities under her guidance – her encouragement to my academic career was crucial for my professional development. I extend my gratitude to Dr. Andrés P. S. Cajamarca, Dr. Luis H. R. Cistern and Prof. Fernando H. Milanese for the technical discussions, their guidance through my research activities and collaboration in the accomplishment of my work.

I would like to thank the members of this defense committee, Prof. Marcos R. Cárdenas and Prof. Emilio E. Paladino, for their availability in reading and evaluating this manuscript and for their valuable suggested improvements to the final manuscript.

I am deeply thankful for the excellent academic education received within the Graduate Program in Mechanical Engineering at the Federal University of Santa Catarina, Brazil. In addition to a qualified faculty, both the technical and administrative staff, as well as the structure offered by the University, made it a formative and outstanding experience.

I would like to give a special thanks to all the *Labtucal* team for the technical and administrative support, besides the nurtured friendship during lunches and coffees. Specifically, I would like to thank Pamela M. Hulse and Gian M. Gatti, for the hours of unraveling, fixing, building and running the tests on the experimental bench. Charles N. da Silva, Gregori Rosinski, Leandro da Silva, and Luiz Domingos, for the prototype development and practical teachings. Ana Roberta, Andreza Souza and Kenia Milanez, for the administrative survival aid. Antônio Alexandre, Carol Antunes, Dijane Ferreira, Felipe Gotardo, Felipe Telles, Fernando Gonçalves, Gabriel Serafin, Guilherme Carqueja, João Batista, Joel Moreira, Juan Mera, Luis Betancur, Nelson Londoño, Nicolas Rodio, Pedro Bellani, Priscila Gonçalves, Victor Soares and Wellington de Almeida, for the technical discussions and advices.

I also thank the financial support from the Brazilian oil and gas company *PETROBRAS*, which funded my scholarship within the research cooperation regarding the national development of diffusion-bonded heat exchangers, in partnership with *Labtucal*.

Moreover, several friends accompanied me on this journey indirectly contributing to the realization of this work. Specifically, I would like to thank Jakeline Tomazi, Lara Brasil, Thainara Piller and Vinicius Macedo, patient flatmates I had the joy of living together. Also, thanks to Guilherme Schowantz, coffee-time and sports mate. And symbolically thanks to all

the *forró* dance partners and musicians I met weekly on the pre-pandemic times, to the sound of *Trio Erva Rasteira*, reminding me of life and happiness beyond work.

Lastly, and perhaps most importantly, I am deeply grateful to my family for the emotional support and encouragement to face my Master's. My parents Denise P. Cavalcanti and Fernando Alvarez, the inspiration of scientists and human beings. My sister, Luciana C. Alvarez, for her closeness despite our physical distance. And my partner, Alessandra J. de Almeida, for walking alongside me in the discoveries of the profession and life. Thank you for everything, and I am happy to share this achievement with you!

*Corra, não pare, não pense demais  
Repare essas velas no cais  
Que a vida é cigana  
É caravana  
É pedra de gelo ao sol*

Geraldo Azevedo e Alceu Valença. "Caravana". 1974.

## ABSTRACT

Heat exchangers are equipment that transfers thermal energy between two or more fluids. This equipment is widely used in different fields, from automobile and avionics to petrol-chemical and power-engineering. Among the existing types of heat exchangers, the printed-circuit heat exchanger is a high efficiency equipment, in addition to withstanding high pressures and temperatures. This highly-engineered equipment can stand pressures up to 50 MPa and temperatures up to 800°C, present large heat transfer surface areas, high compactness, and the possibility of modularization. However, most scientific investigations focus on its application with carbon dioxide and helium as working fluids. In the current study, a diffusion-bonded heat exchanger, with a novel zigzag channel is thermally and hydraulically evaluated. Two different layout configurations are explored. First, the prototype is tested with water in both fluid streams. Through the variation on the inlet flow conditions, the thermal performance of the prototype is evaluated. The heat transfer capabilities of its channel geometry are synthesized through the development of a Nusselt number correlation for water, based on dimensionless Reynolds and Prandtl numbers, covering laminar to turbulent flow regimes. In the laminar regime, the current geometry increases the Nusselt number up to 4.1 times when compared to a straight channel. Second, the prototype is tested in an air-water layout. The thermal and hydraulic performance is evaluated as a function of the airflow. The heat transfer and the pressure drop are evaluated by correlation involving the Nusselt number and the Fanning friction factor. Data from similar diffusion-bonded heat exchangers with different zigzag channels is revisited and used to compare with the performance of the current prototype. The current geometry rises the Fanning friction factor up to 10 times when compared to a straight channel one. This assessment of results, including different fluids, flow regimes, and channel geometries, allows for a better understanding of the thermal and hydraulic performance of diffusion-bonded heat exchangers.

**Keywords:** Diffusion-bonded heat exchanger. Thermal and hydraulic performance. Nusselt number and Fanning friction factor correlation.

## RESUMO

Trocadores de calor são equipamentos que transferem energia térmica entre dois ou mais fluidos. Estes equipamentos são amplamente difundidos em diferentes áreas, desde automotivo e aeronáutico até indústrias petroquímicas e de produção de energia. Trocadores de calor unidos por difusão são candidatos promissores à trocadores de alta eficiência. Estes equipamentos podem suportar pressões de até 50 MPa e temperaturas de até 800 ° C, apresentam grandes áreas de superfície de transferência de calor, alta compactidade e possibilidade de modularização. No entanto, a maior parte das investigações científicas concentram-se em aplicações envolvendo os fluidos dióxido de carbono e hélio. No presente estudo, um trocador de calor unido por difusão, com um novo canal em zigue-zague, fabricado de maneira análoga aos do tipo “circuito impresso” é testado térmica e hidráulicamente. Duas combinações de fluidos são exploradas. Primeiro, o protótipo é testado com água em ambas as correntes de fluido. Através da variação nas condições de vazão de entrada, o desempenho térmico do protótipo é avaliado. Uma correlação do número de Nusselt envolvendo os números adimensionais de Reynolds e Prandtl é desenvolvida para a transferência de calor para água, abrangendo os regimes de fluxo de laminar à turbulento. No regime laminar, o número de Nusselt relativo à geometria proposta é cerca de 4,1 vezes maior do que o observado para um canal reto. Na segunda combinação, o protótipo é testado com ar e água, sendo seu desempenho térmico e hidráulico avaliado em função do fluxo de ar. As características de transferência de calor e queda de pressão são correlacionadas com o número de Nusselt e o fator de atrito de Fanning. Dados de trocadores de calor unidos por difusão semelhantes ao do presente trabalho, porém com geometrias de canais distintas, são revisitados e usados como comparação com o protótipo atual. Observa-se que a geometria proposta apresenta um fator de atrito Fanning até 9,9 vezes maior quando comparada à um canal reto. Esta avaliação dos resultados, incluindo diferentes fluidos, regimes de fluxo e geometrias de canal, permite uma melhor compreensão do desempenho térmico e hidráulico de trocadores de calor unidos por difusão.

**Palavras-chave:** Trocador de calor unido por difusão. Desempenho térmico e hidráulico. Correlação do número de Nusselt e do fator de atrito de Fanning.

## RESUMO EXPANDIDO

### Introdução

Em um cenário global de diminuição dos recursos energéticos e aumento dos custos de energia e das preocupações ambientais, a conservação de energia é considerada um fator chave na agenda econômica mundial. Aliado a esses fatores, o constante aumento das demandas energéticas mundiais intensifica a busca por modelos de desenvolvimento sustentável que passam, entre outras ações, pelo constante aperfeiçoamento tecnológico dos equipamentos industriais. Dentre os dispositivos em constante melhoramento, os trocadores de calor, equipamentos que transferem energia térmica entre dois ou mais fluidos, aparecem como equipamentos industriais de grande interesse de desenvolvimento. Exemplos onde trocadores de calor são utilizados são na geração de energia, indústria petroquímica, indústria alimentícia, eletrônicos, automotivo, aeroespacial, dentre outros, em aplicações como evaporadores, condensadores, radiadores, regeneradores, etc. Assim, diversas pesquisas buscam o aprimoramento dos trocadores de calor através do aumento de suas taxas de transferência térmica. Dentre os diferentes tipos existentes, o trocador de calor do tipo circuito-impresso aparece como um equipamento de alta efetividade. Neste, canais de seção semicircular são usinados em placas metálicas através do ataque fotoquímico. Posteriormente, essas placas são sobrepostas e soldadas umas às outras através do processo de união por difusão, produzindo o núcleo do equipamento. Finalmente, os bocais e demais elementos de distribuição são acoplados ao núcleo, finalizando o trocador de calor. Devido ao seu processo de fabricação, esse tipo de trocador de calor é um equipamento robusto, capaz de operar em pressões de até 50 Mpa e temperaturas de até 800°C, além de apresentar grandes áreas de superfície de transferência de calor, alta compactidade e possibilidade de modularização. Essa série de vantagens faz do trocador de calor do tipo circuito impresso um equipamento utilizado em plataformas marítimas de produção de petróleo e gás e ciclos de dióxido de carbono supercrítico. Alternativamente ao processo de ataque fotoquímico, outros processos de usinagem podem ser utilizados previamente à união por difusão, como por exemplo o corte à jato d'água. Neste caso, placas usinadas são intercaladas com placas não-usinadas, formando posteriormente um equipamento com canais de seção quadrada. Diversos estudos da literatura buscam caracterizar a geometria de diferentes trocadores de calor unidos por difusão através da avaliação de seu coeficiente de troca de calor convectivo e de seu coeficiente de fator de atrito. Porém, a maior parte desses estudos baseiam-se em experimentos conduzidos com os fluidos dióxido de carbono e hélio. Além disso, grande parte dos estudos existentes são realizados para baixos valores de número de Reynolds. Em certos casos, recorre-se à métodos de simulação numérica para se estender as faixas de validade das correlações de troca térmica e de fator de atrito. Porém, em tais casos as condições de contorno podem divergir das condições reais de operação dos equipamentos. Nota-se também um interesse crescente na utilização de trocadores de calor do tipo circuito impresso como pré-resfriadores em ciclos de dióxido de carbono supercríticos. Porém, são poucos os estudos que focam nas condições de operação da água, fluido frio desta configuração, na performance do equipamento. Assim, poucas correlações térmicas e hidráulicas estão disponíveis para a água para trocadores de calor do tipo circuito-impresso. Dentre as existentes, grande parte são baseadas em simulações numéricas, e há dados limitados para as faixas de escoamento transição-turbulento.

## Metodologia

O presente trabalho realiza um estudo térmico e hidráulico de um trocador de calor unido por difusão. Fabricado através da usinagem de placas metálicas por corte à jato d'água, o equipamento produzido possui um ângulo de zigue-zague de  $90^\circ$ . Sua performance é avaliada em uma bancada experimental através de duas combinações de fluidos. Em um primeiro momento, o protótipo é testado com água em ambos os ramais quente e frio, abrangendo os regimes de escoamento de laminar à turbulento, através da variação das condições de vazão de entrada. Além dos parâmetros de troca térmica, coeficiente global de transferência de calor, efetividade e número de unidades de transferência, uma correlação do número de Nusselt envolvendo os números adimensionais de Reynolds e Prandtl é desenvolvida para a água. Os resultados obtidos são comparados com correlações existentes da literatura para outras geometrias de canais. Em sua segunda configuração de fluidos, o protótipo é testado com o arranjo ar (fluido quente) – água (fluido frio), sendo seu desempenho térmico e hidráulico avaliado em função do fluxo de ar. As características de transferência de calor e queda de pressão são correlacionadas com o número de Nusselt e o fator de atrito de Fanning, respectivamente. Para a análise dos resultados térmicos das diferentes configurações de fluidos testados, distintas metodologias de tratamento dos dados são propostas, baseadas na análise das resistências térmicas dos fluidos envolvidos. Para a primeira configuração, água-água, as resistências convectivas possuem ordem de grandeza similar. Para o segundo arranjo de fluidos, ar-água, a resistência convectiva da água é desprezada frente a do ar. Em ambos os casos, a correlação de número de Nusselt é proposta através de uma regressão não-linear comparando o coeficiente global de transferência de calor quando calculado experimentalmente e analiticamente, através da análise de resistências térmicas. A análise hidráulica dos resultados experimentais avalia analiticamente as diferentes contribuições de variação de pressão estática do fluido ao longo de sua passagem pelo núcleo do trocador de calor. A contribuição de queda de pressão exclusiva aos canais no núcleo do equipamento é calculada, e uma correlação de fator de atrito de Fanning é proposta para o canal avaliado através de uma regressão não-linear. De modo a se avaliar a influência do ângulo de zigue-zague do presente protótipo em sua performance, dados de trocadores de calor unidos por difusão com canais zigue-zague de ângulos  $144^\circ$  e  $180^\circ$  são revisitados. Tais equipamentos foram testados com os mesmos fluidos, em condições e faixas de operação similar à do presente estudo. Os resultados de troca térmica e queda de pressão estática são comparados entre tais equipamentos.

## Resultados e Discussão

Como são esperadas divergências entre a geometria real do equipamento produzido e suas dimensões de projeto, uma análise de imagem prévia ao tratamento dos dados é realizada a partir de fotografias da seção de entrada do núcleo do equipamento. Os resultados desta análise mostraram que a altura e largura dos canais são menores do que as dimensões de projeto, sendo a altura a dimensão mais afetada. Em sua configuração água-água, o número de Reynolds dos canais quente e frio variou entre 1529-8313 e 1299-6618, respectivamente. A troca térmica total do protótipo testado variou entre 22 kW e 63 kW, sua efetividade entre 0,3 e 0,75 e o número de transferência de unidades entre 0,5 e 1,5, para as diferentes condições experimentais testadas. Uma nova correlação de troca térmica foi proposta através do número de Nusselt, baseada nos adimensionais de número de Reynolds e Prandtl, para uma faixa de escoamento do regime laminar ao turbulento. Para a análise dos resultados obtidos, correlações de número de Nusselt para distintas geometrias existentes na literatura foram utilizadas como comparação. No regime laminar, o protótipo testado apresenta um aumento médio de 4,1 vezes no número de Nusselt quando comparado a uma correlação para uma tubulação reta. Este aumento cai para 2,6 vezes na transição laminar-turbulento, e 1,5 vezes no escoamento turbulento. O aumento na queda de

pressão do protótipo testado, quando comparado a uma tubulação reta, é de até 16 vezes para o valor máximo de número de Reynolds testado. No segundo arranjo experimental avaliado, ar-água, devido à grande divergência entre as capacidades térmicas dos fluidos, o protótipo se mostrou termicamente superdimensionado para ser testado na bancada experimental. Para contornar este problema, apenas parte dos dados experimentais foi mantida na análise térmica subsequente. Já os resultados hidráulicos não foram impactados. Além dos dados dos trocadores com ângulos de zigue-zague de 144° e 180° revisitados, outros resultados da literatura para canais com distintos ângulos também foram utilizados na comparação dos resultados. O protótipo testado mostrou-se o mais suscetível ao aumento de troca térmica em resposta ao aumento das vazões de ar. De modo geral, nota-se o aumento do número de Nusselt ao passar de um canal reto a canais com o percurso de escoamento em zigue-zague. Em contrapartida, as perdas hidráulicas também se acentuam com os canais em zigue-zague. Para avaliar ambas contribuições, o fator de Colburn e o fator de atrito de Fanning são calculados para o protótipo testado e para as geometrias revisitadas. Quando comparado a um canal reto, para a faixa de Reynolds entre 2769 e 3175, o canal de 90° testado apresenta um aumento do fator de Colburn de 2,3 e um aumento no fator de atrito de Fanning de 9,9 vezes. Para a mesma faixa de escoamento, o canal com ângulo de zigue-zague de 144° apresenta um aumento no fator de Colburn de 1,9 vezes e um aumento no fator de atrito de Fanning de 2,4 vezes, quando comparado a um canal reto. Nota-se, portanto, que os canais de 90° e 144° oferecem aumentos de troca térmica próximos entre si, quando comparados a um canal reto. Porém, o aumento das perdas hidráulicas, diretamente relacionadas ao fator de atrito, são muito mais onerosas no canal de 90°. Em conclusão, a presente dissertação fornece correlações de troca térmica e de fator de atrito para distintas geometrias, que podem ser utilizadas para o projeto e/ou avaliação de trocadores de calor unidos por difusão para determinadas condições de operação. Para trabalhos futuros, destaca-se a sugestão de analisar os aumentos de troca térmica e de fator de atrito através de uma análise entrópica, a fim de se avaliar ambas as contribuições do ponto de vista energético.

**Palavras-chave:** Trocador de calor unido por difusão. Desempenho térmico e hidráulico. Correlação do número de Nusselt e do fator de atrito de Fanning.

## LIST OF FIGURES

FIGURE 1 – HEAT EXCHANGER BASIC CONCEPT AND COMMON APPLICATIONS. (LIENHARD, 2020) .....	27
FIGURE 2 – (A) PARALLEL OR COUNTERFLOW HEAT EXCHANGER CONFIGURATIONS, AND (B) CROSSFLOW HEAT EXCHANGER. ADAPTED FROM (LIENHARD, 2020).....	28
FIGURE 3 – OVERVIEW OF HEAT EXCHANGER COMPACTNESS. (LEE, 2010).....	29
FIGURE 4 – (A) PCHE CORE (B) 3D CUTAWAY SCHEMATIC OF A PCHE ASSEMBLY. ADAPTED FROM (CHAI; TASSOU, 2020).....	30
FIGURE 5 – (A) MICROGRAPH OF A PCHE WITH SEMI-CIRCULAR CROSS-SECTION CHANNELS AND (B) SCHEMATIC DIAGRAM OF FLOW CHANNELS. (DAVID SOUTHALL, 2008; HUANG ET AL., 2019).....	31
FIGURE 6 – COUNTERFLOW HEAT EXCHANGER BASIC THERMAL PARAMETERS. ADAPTED FROM (SHAH; SEKULIC, 2003).....	39
FIGURE 7 – THERMAL CIRCUIT MODEL OF A COUNTERFLOW HEAT EXCHANGER. ADAPTED FROM (LEE, 2010). .....	42
FIGURE 8 – TEMPERATURE DISTRIBUTION OF THE FLUIDS THROUGH THE HEAT EXCHANGER (A) COUNTERFLOW ARRANGEMENT, FLUIDS WITH FINITE DIFFERENT $cp$ , AND (B) COLD FLUID ON PHASE CHANGE (BOILING) ( $cp, c \rightarrow \infty$ ). ADAPTED FROM (BEJAN; KRAUS, 2003). .....	47
FIGURE 9 – HOT (ABOVE) AND COLD (BELOW) CAD PLATE SHEETS OF THE MANUFACTURED DBHE, AND DETAILED VIEW OF THE ZIGZAG CHANNEL GEOMETRY. ....	49
FIGURE 10 – SCHEMATICS OF THE HEAT EXCHANGER’S PLATE ORDER AND FLUID DIRECTION (A) AND THE FINAL CORE, (B), WITH DETAILED VIEWS OF THE CHANNELS’ DISTRIBUTION AT THE ENTRANCE OF EACH STREAM AND CROSS-SECTION VIEW. ....	50
FIGURE 11 – (A) SCHEMATIC OF THE INLET COLD VIEW INDICATING THE CHANNELS' MAIN DIMENSIONS WHEN SEEN PERPENDICULARLY TO THE ENTRANCE AND (B) CLARIFICATION OF THE CHANNEL WIDTH ASTERISK NOTATION WITH RESPECT TO THE CHANNEL ZIGZAG ANGLE. .....	51
FIGURE 12 – SCHEMATICS OF THE INLET HEADER ASSEMBLY CROSS-SECTION VIEW (A) AND THE FINAL HEAT EXCHANGER TEST SECTION (B). ....	51
FIGURE 13 – CAD VIEW OF THE COLD-BRANCH OF THE TEST FACILITY. ....	53
FIGURE 14 – CAD VIEW OF THE HOT-BRANCH OF THE TEST FACILITY. ....	54
FIGURE 15 – CAD VIEW OF THE HOT-BRANCH OF THE TEST FACILITY. ....	55
FIGURE 16 – EXPERIMENTAL WATER-WATER SETUP PHOTOGRAPH. ....	56

FIGURE 17 – ROLLOVER (OR DROP-OFF) PHENOMENON IN A $j$ vs. $Re$ CHARACTERISTIC OF A HEAT EXCHANGER SURFACE. ADAPTED FROM (SHAH; SEKULIC, 2003).....	62
FIGURE 18 – PRESSURE DROP ALONG A HEAT EXCHANGER CHANNEL. ADAPTED FROM (SHAH; SEKULIC, 2003). .....	63
FIGURE 19 – HEAT EXCHANGER BALANCE BETWEEN THE COLD AND HOT STREAMS (A) AND HEAT LOSS RATIO TO THE AVERAGE HEAT LOAD (B).....	71
FIGURE 20 – HEAT TRANSFER RATE (A) AND OVERALL HEAT TRANSFER COEFFICIENT (B) VS. REYNOLDS NUMBER ON THE HOT CHANNEL.....	72
FIGURE 21 – EFFECTIVENESS VS. NTU, (A), AND VS. THE REYNOLDS NUMBER OF THE HOT CHANNEL, (B). .....	74
FIGURE 22 – OVERALL HEAT TRANSFER COEFFICIENT COMPARISON BETWEEN THE FITTED MODEL VS. EXPERIMENTAL VALUE.....	74
FIGURE 23 – NUSSELT NUMBER COMPARISON BETWEEN THE EXPERIMENTAL DATA OF THE 90° ZIGZAG CHANNEL DBHE, A THEORETICAL STRAIGHT CHANNEL DBHE, AND A 90° ZIGZAG CHANNEL FROM THE LITERATURE. ....	76
FIGURE 24 – PROPOSED NUSSELT NUMBER CORRELATION FOR 90° ZIGZAG CHANNEL COMPARED WITH MODELS. (A) COMPARISON WITH 150° AND 100° ZIGZAG CHANNELS AND STRAIGHT CHANNEL CORRELATIONS FOR LAMINAR AND TRANSITION REGIMES. (B) COMPARISON WITH 100° ZIGZAG AND STRAIGHT CHANNEL CORRELATIONS FOR TURBULENT FLOW REGIME....	79
FIGURE 25 – EXPERIMENTAL 90° ZIGZAG ANGLE CHANNEL PRESSURE DROP COMPARISON WITH 100° AND 180° CHANNELS.....	81
FIGURE 26 – HEAT EXCHANGER BALANCE BETWEEN THE COLD AND HOT STREAMS (A) AND OUTLET HOT TEMPERATURE VS. COLD INLET TEMPERATURE. MODIFIED DATA FOLLOWING CORRECTION PARAMETER FROM EQ. (5.2) IN RED AND UNMODIFIED DATA IN BLUE.....	84
FIGURE 27 – HEAT TRANSFER RATE VS. (A) AIR REYNOLDS NUMBER, AND (B) WATER REYNOLDS NUMBER.....	85
FIGURE 28 – DBHE 90 REPRESENTATION. (A) FLUIDS ARRANGEMENT AND THERMOCOUPLES POSITIONING. (B) THERMOCOUPLES READING ON THE PROTOTYPE SURFACE. ....	86
FIGURE 29 – OVERALL HEAT TRANSFER COEFFICIENT COMPARISON BETWEEN THE FITTED MODEL VS. EXPERIMENTAL VALUE FOR THE DBHE 90 AIR-WATER EXPERIMENT. ....	89
FIGURE 30 – COMPARISON OF THE THEORETICAL OVERALL HEAT TRANSFER COEFFICIENT CALCULATED THROUGH MODEL 2 AND MODEL 3. ....	90

FIGURE 31 – OVERALL HEAT TRANSFER COEFFICIENT COMPARISON BETWEEN THE FITTED MODEL VS. EXPERIMENTAL FOR (A) DBHE 144 AND (B) DBHE 180 AIR-WATER EXPERIMENTS....	90
FIGURE 32 – THERMAL RESULTS COMPARISON BETWEEN DBHEs 90, 144 AND 180. (A) OVERALL HEAT TRANSFER COEFFICIENT VS. AIR SIDE REYNOLDS NUMBER. (B) EFFECTIVENESS VS. NTU. (C) EFFECTIVENESS VS. AIR SIDE REYNOLDS NUMBER.....	92
FIGURE 33 – NUSSELT NUMBER CORRELATIONS COMPARISON BETWEEN THE PRESENT 90° ZIGZAG CHANNEL, 144° ZIGZAG CHANNEL (DBHE 144), 180° ZIGZAG CHANNEL (DBHE 180), (KIM ET AL., 2016) 100° ZIGZAG CHANNEL, (CHEN ET AL., 2016B) 150° ZIGZAG CHANNEL , AND (GNIELINSKI, 2013) STRAIGHT DUCT. ....	94
FIGURE 34 – CORE PRESSURE DROP ALONG THE AIR-SIDE OF DBHEs 90, 144 AND 180. ....	95
FIGURE 35 – FANNING FRICTION FACTOR EXPERIMENTAL DATA FOR DBHEs 90, 144 AND 180.	96
FIGURE 36 – EXPERIMENTAL AND MODEL FANNING FICTION FACTOR COMPARISON FOR (A) DBHE 90, (B) DBHE 144, (C) DBHE 180. ....	97
FIGURE 37 – FANNING FRICTION FACTOR CORRELATION COMPARISON WITH CIRCULAR STRAIGHT TUBE (SHAH; SEKULIC, 2003), (CHEN ET AL., 2016B) FOR A 150° ZIGZAG CHANNEL AND (KIM ET AL., 2016) FOR A 100° ZIGZAG CHANNEL .....	99
FIGURE 38 – COLBURN FACTOR AND FANNING FRICTION FACTOR VS. AIR REYNOLDS NUMBER FOR DBHEs 90, 144 AND 180.....	100
FIGURE 39 – COLD (A) AND HOT (B) INLET PORTS OF THE 90° ZIGZAG CHANNEL DBHE. ....	119
FIGURE 40 – COLD INLET PORTS OF THE 144° ZIGZAG CHANNEL DBHE.....	120

## LIST OF TABLES

TABLE 1 – WATER-WATER EXPERIMENTAL TEST CONDITIONS.....	57
TABLE 2 – AIR-WATER EXPERIMENTAL TEST CONDITIONS.....	57
TABLE 3 – CHANNELS’ DIMENSION OF THE 90° ZIGZAG ANGLE PROTOTYPE. ....	70
TABLE 4 – WATER-WATER EXPERIMENTAL UNCERTAINTIES.....	71
TABLE 5 - CHENG ET AL. (2020) PCHE GEOMETRY AND TEST CONDITIONS. ADAPTED FROM (CHENG ET AL., 2020).....	77
TABLE 6 – COMPARISONS BETWEEN THE NUSSELT NUMBER OF THE FITTED EXPERIMENTAL (90°) ZIGZAG CHANNEL AND (SAEED ET AL., 2020) ZIGZAG MODEL, WITH (GNIELINSKI, 2013) AND (SARMIENTO ET AL., 2020B) CORRELATIONS FOR STRAIGHT CHANNELS (180°). ....	79
TABLE 7 – DBHEs 144 AND 180 MAIN DIMENSIONS.....	82
TABLE 8 – DBHE 90 AIR-WATER EXPERIMENTAL UNCERTAINTIES.....	87
TABLE 9 – DBHE 144 AIR-WATER EXPERIMENTAL UNCERTAINTIES.....	87
TABLE 10 – DBHE 180 AIR-WATER EXPERIMENTAL UNCERTAINTIES.....	88
TABLE 11 – DBHEs 90, 144 AND 180 COLBURN AND FANNING FRICTION FACTORS AVERAGE RATIO. ....	100
TABLE 12 – DBHE 90 WATER-WATER EXPERIMENTAL DATA. ....	110
TABLE 13 – DBHE 90 AIR-WATER EXPERIMENTAL DATA. ....	111
TABLE 14 – DBHE 144 AIR-WATER EXPERIMENTAL DATA. ....	121
TABLE 15 – DBHE 180 AIR-WATER EXPERIMENTAL DATA. ....	122

## LIST OF ABBREVIATIONS AND ACRONYMS

CAD	Computer-aided design
<i>DBHE</i>	Diffusion-bonded heat exchanger
He	Helium
<i>Labtucal</i>	Heat Pipe Laboratory (in its Portuguese acronym)
N/A	Not applicable
<i>PCHE</i>	Printed-circuit heat exchanger
PID	Proportional-integral-derivative
<i>PETROBRAS</i>	Brazilian oil and gas company
S-CO <sub>2</sub>	Supercritical CO <sub>2</sub>

## NOMENCLATURE

### Roman alphabet

$a$	constant in Nusselt number correlation in Eq. (4.4)
$A$	heat transfer area, $m^2$
$A_o$	minimum free flow (or open) area on one fluid side of an exchanger, $m^2$
$A_c$	cross-section area of the channel, $m^2$
$A_{fr}$	frontal (or face) area on one side of an exchanger, $m^2$
$b$	constant in Nusselt number correlation in Eq. (4.4)
$c_p$	specific heat capacity, $J.kg^{-1}.K^{-1}$
$C$	heat capacity, $J.K^{-1}.s^{-1}$
$\mathbb{C}$	constant in Nusselt number correlation in Eq. (4.4)
$C_r$	heat capacity ratio
$CT$	Temperature correction parameter in Eq. (5.2)
$d_h$	channel hydraulic diameter, $m$
$D$	pipe hydraulic diameter, $m$
$e$	thickness of the wall separating fluid streams, $m$
$E_i$	intercalated non-machined metal sheet plates thickness, $m$
$E_p$	hot and cold machined metal sheet plate thickness, $m$
$G$	fluid stream mass velocity, $kg.m^{-2}.s^{-1}$
$h$	convective heat transfer coefficient, $W.m^{-2}.K^{-1}$
$i$	specific enthalpy, $kJ.kg^{-1}$
$k$	thermal conductivity, $W.m^{-1}.K^{-1}$
$K_c$	contraction loss coefficient at the channel's entrance
$K_e$	expansion loss coefficient at the channel's exit
$L$	fluid path length, $m$
$\dot{m}$	mass flow rate, $kg.s^{-1}$
$n$	constant in Fanning friction factor correlation in Eq. (4.22)
$N$	constant in Fanning friction factor correlation in Eq. (4.22)
$NTU$	Number of transfer units
$Nu$	Nusselt number
$p$	zigzag pitch, $m$

$\delta Q$	heat transfer rate associated with infinitesimal state change, $W$
$Q$	heat transfer rate, $W$
$R$	thermal resistance, $^{\circ}C \cdot W^{-1}$
$\tilde{R}$	gas constant, $J \cdot kg^{-1} \cdot K^{-1}$
$Re$	Reynolds number
$R_w$	wall thermal resistance, $K \cdot W^{-1}$
$T$	temperature, $^{\circ}C$
$\Delta T$	temperature drop difference, $^{\circ}C$
$\Delta T_{lm}$	mean logarithmic temperature difference, $^{\circ}C$
$\Delta T_m$	mean temperature difference, $^{\circ}C$
$u$	fluid velocity, $m \cdot s^{-1}$
$U$	overall heat transfer coefficient, $W \cdot m^{-2} \cdot K^{-1}$
$w_c$	channel width, m
$w_f$	channel fin width, m

### Greek alphabet

$\alpha$	zigzag channel angle
$\beta$	heat transfer surface area density
$\varepsilon$	effectiveness
$\mu$	fluid dynamic viscosity, $kg \cdot m^{-1} \cdot s^{-1}$
$\sigma$	ratio of free flow area (or surface porosity)
$\rho$	fluid density, $kg \cdot m^{-3}$

### Subscripts

<i>avg</i>	average value
<i>c</i>	cold side
<i>cond</i>	conductive
<i>conv</i>	convective
<i>eff</i>	effective
<i>exp</i>	experimental value
<i>h</i>	hot side
<i>i</i>	fluid stream
<i>in</i>	inlet port of the heat exchanger

<i>loss</i>	losses to the ambient
<i>m</i>	mean value
<i>max</i>	maximum value
<i>min</i>	minimum value
<i>nozzles</i>	nozzles connecting fluid pipe to the heat exchanger entrance and exit section
<i>out</i>	outlet port of the heat exchanger
<i>pipe</i>	fluid discharge pipe to and from the heat exchanger
<i>the</i>	theoretical value
<i>tot</i>	total
<i>w</i>	wall

## CONTENTS

<b>1</b>	<b>INTRODUCTION .....</b>	<b>23</b>
1.1	MOTIVATION AND OBJECTIVES .....	24
1.2	OVERVIEW .....	25
<b>2</b>	<b>LITERATURE REVIEW .....</b>	<b>26</b>
2.1	HEAT EXCHANGERS .....	26
2.2	PRINTED-CIRCUIT HEAT EXCHANGER .....	29
2.2.1	<i>Printed-circuit heat exchanger literature review</i> .....	32
2.2.2	<i>The diffusion-bonded heat exchanger at Labtucal</i> .....	35
2.3	SUMMARY AND SPECIFIC OBJECTIVES .....	36
<b>3</b>	<b>HEAT EXCHANGER DESIGN THEORY .....</b>	<b>38</b>
3.1	GEOMETRICAL OVERVIEW .....	38
3.2	HEAT EXCHANGER PERFORMANCE EVALUATION .....	39
3.3	FLOW PROPERTIES .....	45
<b>4</b>	<b>EXPERIMENTAL METHODOLOGY .....</b>	<b>48</b>
4.1	DBHE FABRICATION .....	48
4.2	TEST FACILITY .....	52
4.3	EXPERIMENTAL PROCEDURE.....	56
4.4	NUSSELT NUMBER CORRELATION DATA REDUCTION METHOD .....	58
4.5	FANNING FRICTION FACTOR CORRELATION DATA REDUCTION METHOD.....	62
4.6	HEAT LOSS AND UNCERTAINTY ANALYSIS .....	67
<b>5</b>	<b>RESULTS AND DISCUSSION .....</b>	<b>69</b>
5.1	PROTOTYPE REAL DIMENSIONS .....	69
5.2	WATER-WATER ANALYSIS .....	70
5.2.1	<i>Water-water thermal analysis</i> .....	70
5.2.2	<i>Water-water hydraulic analysis</i> .....	80
5.3	AIR-WATER ANALYSIS .....	81
5.3.1	<i>Air-water thermal analysis</i> .....	82
5.3.2	<i>Air-water hydraulic analysis</i> .....	94
5.3.3	<i>Air-water thermal and hydraulic comparison: DBHEs 90, 144 and 180</i> 99	

<b>6 CONCLUSIONS AND FUTURE WORK.....</b>	<b>101</b>
<b>BIBLIOGRAPHY .....</b>	<b>105</b>
<b>APPENDIX A –EXPERIMENTAL DATA .....</b>	<b>110</b>
<b>APPENDIX B – UNCERTAINTY ANALYSIS.....</b>	<b>114</b>
<b>APPENDIX C – DBHES INLET PORTS PHOTOS. ....</b>	<b>119</b>
<b>ANNEX A – EXPERIMENTAL DATA DBHES 144 AND 180.....</b>	<b>121</b>



## 1 INTRODUCTION

In a global scenario of diminishing world energy resources, increasing energy costs and rising environmental concerns, energy conservation is considered one of the key points of the world economic agenda. As shown by the U.S. Energy Information Administration (EIA) the world energy consumption is expected to grow by nearly 50% between 2018 and 2050<sup>1</sup>. To achieve sustainable development, energy technologies need to be upgraded, with the renewal and/or development of equipment, for both fossil and renewable energy sources.

One of these technologies is the heat exchanger, a device that transfers heat between two or more fluids. This equipment is widely used, among other fields, in power engineering, petrol-chemical industries, process and food industries, automobile and avionics. They can be applied as evaporators, condensers, automobile radiators, air preheaters, etc. (Hesselgreaves; Law; Reay, 2016; Shah; Sekulic, 2003). Therefore, heat exchangers have been the target of investigations, aiming mainly the heat transfer efficiency enhancement, directly related to energy consumption.

Printed circuit heat exchangers (PCHEs) appear as promising candidates as high-efficiency heat exchangers. Named after the metal sheet plate machining process, in these heat exchangers, semi-circular channels are chemically etched in metal sheet plates. These plates are posteriorly stacked and welded by diffusion bonding technique. This highly engineered manufacturing process produces robust heat exchangers nuclei. Typically, PCHEs can stand pressures up to 50 MPa and temperatures up to 800°C, present large heat transfer surface areas, high compactness, and the possibility of modularization (Hesselgreaves; Law; Reay, 2016; Shah; Sekulic, 2003).

The advantages mentioned explain the utilization of PCHEs in a broad range of fields, such as offshore oil and gas processing, liquefied natural gas devices, high-temperature reactor intercoolers and supercritical carbon dioxide Brayton cycles, besides its potential application in fields such as new generation of nuclear power, solar thermal power, hydrogen energy, etc. (Huang et al., 2019).

---

<sup>1</sup> U.S. Energy Information Administration, International Energy Outlook 2019, Release data: September 24, 2019, Access date: April 23, 2021, <https://www.eia.gov/outlooks/archive/ieo19/>.

## 1.1 MOTIVATION AND OBJECTIVES

Following a similar manufacturing process employed in PCHEs, other diffusion-bonded heat exchangers (DBHEs) are reported in the literature. Specifically, square cross-section channels DBHEs are developed by replacing the chemical-etching machining process with the use of a water jet cutting machine, in a technology investigated at the Heat Pipe Laboratory (*Labtucal*, in its Portuguese acronym), in a partnership with *PETROBRAS* (Brazilian oil and gas company). This in-house developed technique consists of cutting slits in metal-sheet plates, which are posteriorly piled and intercalated with non-machined plates (Mortean et al., 2016; Mortean; Paiva; Mantelli, 2016).

The *Labtucal-PETROBRAS* cooperation program aims to develop nationally the technology of heat exchangers welded by diffusion. In this context, theoretical calculations of thermal-hydraulic performance of square cross-section DBHEs were conducted showing good agreement with experimental results (Sarmiento et al., 2020a). Furthermore, different flow arrangements and fluid flow paths were experimentally evaluated (Batista, 2017; Gatti, 2020; Hulse, 2020; Mortean et al., 2016). However, the thermal-hydraulic performance comparison of different channel flow path geometries has not been fully investigated in the mentioned works.

Therefore, the general objective of the current work is to analyze the thermal and hydraulic performance of different fluid flow path DBHEs operating in similar conditions. Moreover, in order to design heat exchangers, precise and accurate heat transfer and pressure drop correlations are required, whether the equipment has square or semi-circular channels. To this end, a DBHE prototype with a novel channel design was thermally and hydraulically tested. Correlations for the heat transfer and pressure drop of this prototype are proposed based on the experimental results obtained. Data from previous experiments of different fluid flow paths are revisited and analyzed following the methodology proposed in the current work. The set of correlations here proposed can be used for designing and rating heat exchangers' problems. The specific objectives of the current work are outlined at the end of the next chapter.

Most of the content presented in this Master's dissertation is based on the recently published paper, first-authored by this Master's candidate: *Heat transfer investigation of a 90° zigzag channel diffusion-bonded heat exchanger*, by R. Cavalcanti Alvarez, A. P. C. Sarmiento, L. H. R. Cisterna, F. H. Milanese, M. B. H. Mantelli, *Applied Thermal Engineering*, v. 190, 2021.

This work is part of the *Labtucal-PETROBRAS* partnership, under the diffusion-bonded heat exchangers project, developed at the Federal University of Santa Catarina, Florianópolis, Brazil.

## 1.2 OVERVIEW

The present work is structured as follows. In Chapter 2, the literature review regarding heat exchangers, more specifically diffusion-bonded heat exchangers, is presented. The specific objectives of the present investigation are posteriorly described. Chapter 3 presents the theory for the heat exchanger mathematical design. This includes the geometrical, thermo-hydraulic and fluid flow properties evaluation parameters. In Chapter 4, the experimental methodology is described. The DBHE main geometric parameters, the test facility and the experimental procedure employed in this work are presented. Then, the experimental data treatment is discussed. Finally, losses to the ambient and uncertainty analysis are described. In Chapter 5, sets of thermo-hydraulic results of the tested prototype, under two different combinations of fluids, i.e. water-water and air-water, are presented. The results obtained are compared with correlations from the literature. Furthermore, experimental data from the literature from similar equipment but with different channel geometries are revisited and used for comparison with the correlations. In Chapter 6 the main conclusions and recommendations for future works are discussed.

In addition to the main chapters, in Appendices A and B, all the experimental data obtained in the current work, as well as the detailed overview of the uncertainty analysis of the parameters, are presented.

## 2 LITERATURE REVIEW

This chapter presents the object of study of the present work, which is the heat exchanger. After its contextualization in the global scenario and a brief presentation of its different classifications, the diffusion bonded, including the printed-circuit heat exchangers, are presented. Then, an extensive literature review of this equipment is discussed, focusing on its thermal and hydraulic performance. Finally, a summary of the current state-of-the-art and the specific objectives of the current work is presented.

### 2.1 HEAT EXCHANGERS

Heat exchangers are devices that transfer heat between two or more fluids at different temperatures (Kakaç; Liu; Pramuanjaroenkij, 2002; Lee, 2010; Shah; Sekulic, 2003). In most cases, the fluids are separated through a thin wall (parting sheet or tube wall), in a configuration also called as direct transfer type, or simply recuperator. In such layout, heat is transferred by conduction through the separating wall and by convection from the hot fluid to the wall and from the wall to the cold fluid (Bejan; Kraus, 2003; Shah; Sekulic, 2003).

These devices are widely spread in different applications, such as power generation, process, chemical and food industries, electronics, refrigeration, space, among others (Kakaç; Liu; Pramuanjaroenkij, 2002). Common examples of heat exchangers are the shell-and-tube, automobile radiators, condensers, evaporators, air preheaters and cooling towers (Shah; Sekulic, 2003). The principal constituents of a heat exchanger are its core, also called matrix, which contains the heat transfer surface and the fluids distribution devices, such as headers, tanks, inlet and outlet nozzles or headers, etc. (Shah; Sekulic, 2003). The basic concept of a heat exchanger and common application examples are seen in Figure 1.

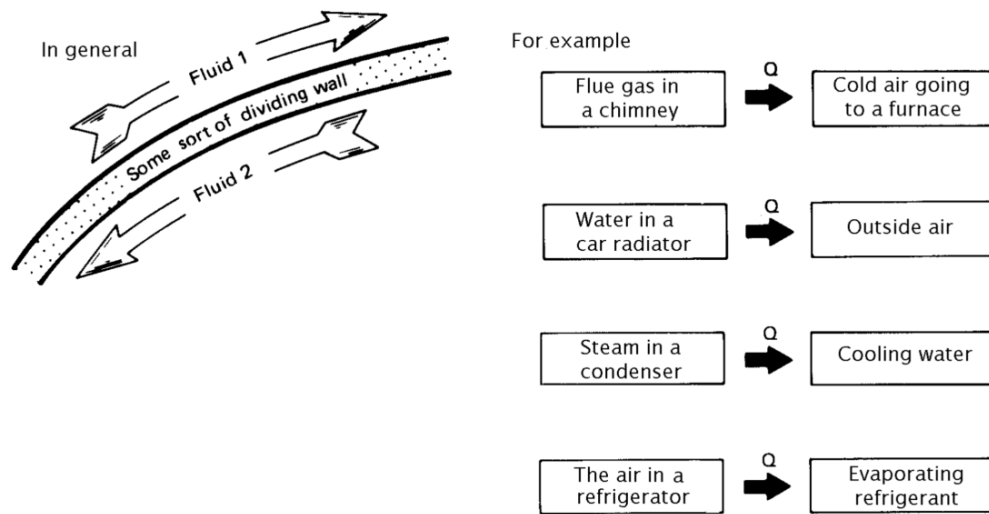


Figure 1 – Heat exchanger basic concept and common applications. (Lienhard, 2020)

Heat exchangers are classified in numerous ways, such as the number of fluids, heat transfer mechanisms, construction type, flow arrangement, or compactness. These classifications are briefly discussed hereafter. A complete characterization is found in Ref. (Shah; Sekulic, 2003).

i. Number of fluids

Although it exists heat exchangers with as many as 12 fluids streams used in some chemical process applications, most processes of heating, cooling, heat recovery or heat rejection applications occur in two-fluids heat exchangers (Shah; Sekulic, 2003).

ii. Construction type

The four major construction types are tubular, plate-type, extended surface and regenerative exchangers. Shell-and-tube, a tubular exchanger, is used in liquid-to-liquid, liquid-to-phase change, gas-to-liquid and gas-to-gas applications. Its main advantages are flexibility in design and the capability of operating at high pressures, relative to the environment or in between the fluids. On the other hand, plate-type heat exchangers are usually built of thin plates, which are welded, brazed or separated by gaskets. An advantage of a plate heat exchanger is that very high heat transfer coefficients are achieved, partially due to the small hydraulic diameter flow passages. Moreover, the surface area required for a plate heat exchanger can be one-half to one-third that of a shell-and-tube exchanger and its gross weight can be about one-sixth, for equivalent heat duty shell-and-tube equipment (Shah; Sekulic, 2003).

### iii. Flow arrangement

Parallel, counter and crossflow configurations are among the basic single pass heat exchangers flow arrangements. In parallel flow, the hot and cold fluid streams enter at the same extremity, flow in the same sense, and exit the equipment in an opposite extremity to the entrance. In the counter flow (or countercurrent) exchanger, the fluids flow parallel to each other, however, in the opposite sense. Therefore, the hot and cold entrance ports are in opposite extremities, as well as their exit ports. In the crossflow configuration, the fluids flow in a normal direction to each other and the streams may be mixed-unmixed or unmixed-unmixed. This last configuration simplifies the design of the headers, avoiding the overlapping of entrance and exit fluid streams. Figure 2 exemplifies these different heat exchangers' flow arrangements.

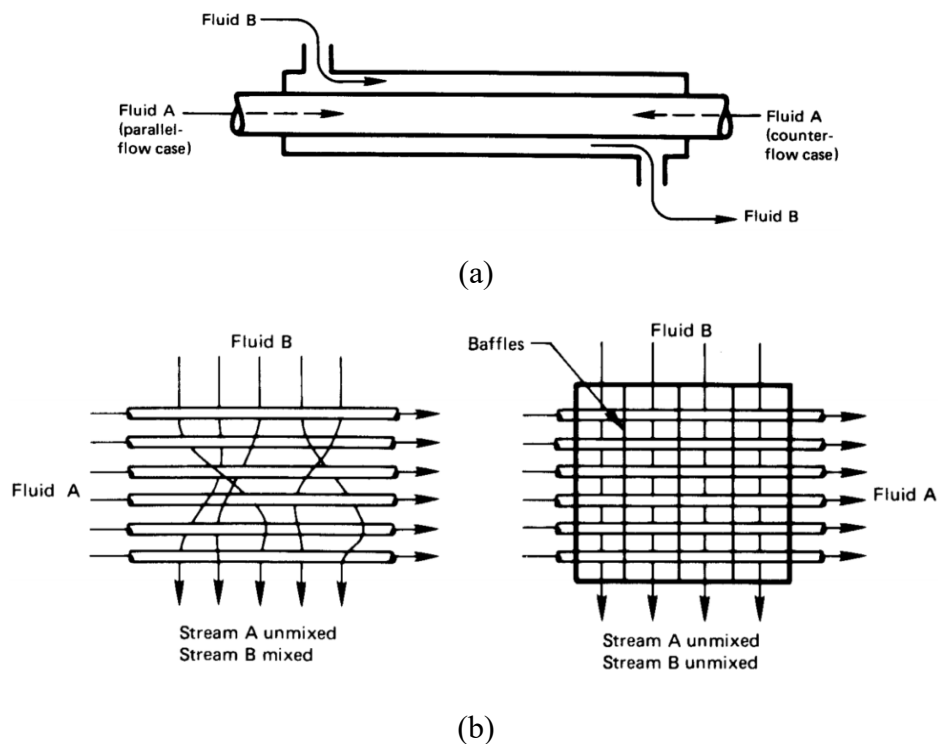


Figure 2 – (a) Parallel or counterflow heat exchanger configurations, and (b) crossflow heat exchanger. Adapted from (Lienhard, 2020).

### iv. Compactness

Compared to shell-and-tube exchangers, a compact heat exchanger is characterized by a large heat transfer surface area per unit of volume, resulting in reduced space, weight, energy requirements and cost (Shah; Sekulic, 2003). The compactness, or the surface area density of a heat exchanger,  $\beta$  [ $m^2/m^3$ ], is defined as the ratio of the heat exchanger heat transfer surface

to its volume. According to Hesselgreaves; Law and Reay (2016), a commonly accepted threshold value for  $\beta$  to be considered as compact is  $300 \text{ m}^2/\text{m}^3$ . For Lee (2010), a compact heat exchanger has a surface area density greater than about  $600 \text{ m}^2/\text{m}^3$  or a hydraulic diameter smaller than about  $6 \text{ mm}$ , operating in a gas stream, as seen in Figure 3. Indeed, as will be discussed, the surface area density is related to the channel hydraulic diameter.

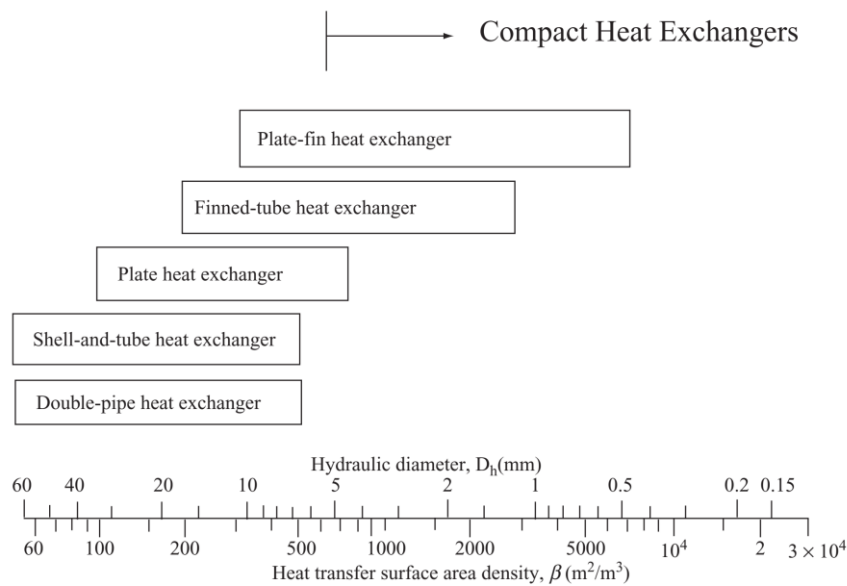


Figure 3 – Overview of heat exchanger compactness. (Lee, 2010)

## 2.2 PRINTED-CIRCUIT HEAT EXCHANGER

The printed-circuit heat exchanger (PCHE) is a plate-type, compact heat exchanger. In this equipment, metal sheet plates are photo-chemically milled to form fluid flow channels, in a process adapted from the electronic printed circuit boards. The machined plates are stacked and diffusion-bonded together, to form a metal solid block with engineered channels in its interior. The diffusion-bonding is a solid-state joining process through the atomic diffusion of the materials at an elevated temperature under a certain interfacial pressure for a period of time (Mortean, 2017). Different materials have been successfully used in producing PCHEs, including stainless steel, titanium, copper, nickel and nickel alloys (Shah; Sekulic, 2003). Several formed blocks can be welded together to form a larger core for higher heat duty applications. Headers and nozzles are posteriorly welded directly onto the final core block, to

form the final heat exchanger. Figure 4 shows a PCHE core section (a), and the final assembly of a PCHE with nozzles and headers distribution devices, in a schematic cutaway image of a crossflow arrangement, (b). As seen in Figure 4, the fluid streams inlet/outlet ports are side by side at a 90° angle, due to manufacturing requirements of parallel or crossflow arrangements.

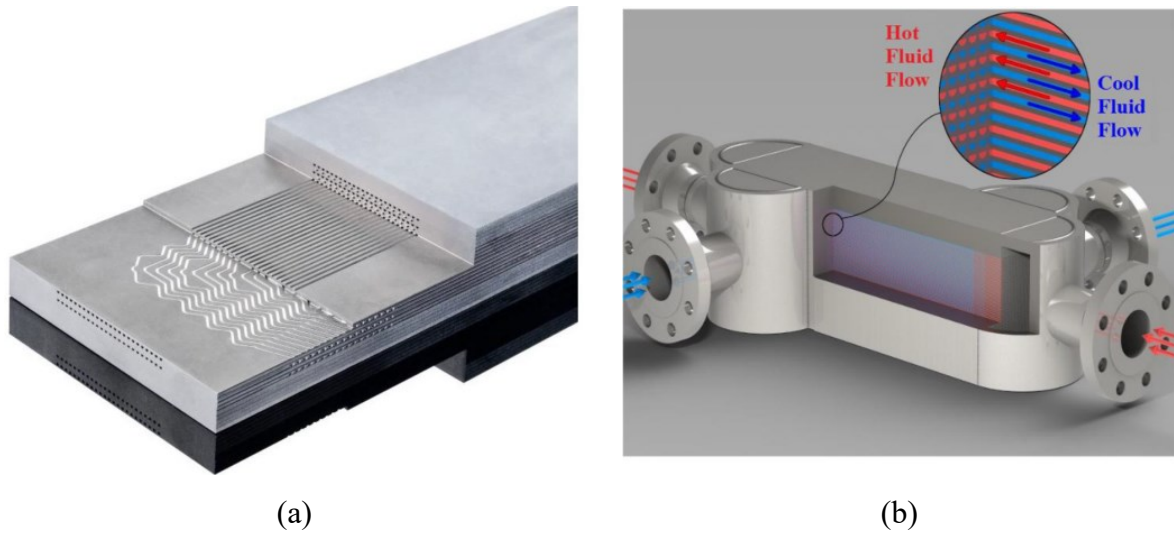


Figure 4 – (a) PCHE core (b) 3D cutaway schematic of a PCHE assembly. Adapted from (Chai; Tassou, 2020)

The photo-chemical etching produces approximately semi-circular cross-section channels, typically 1-2 mm wide and 0.5-1 mm depth, resulting in hydraulic diameters from 1.5 to 3 mm (Hesselgreaves; Law; Reay, 2016). High-surface area densities,  $650\text{-}1300\text{ m}^2/\text{m}^3$  are achievable, for operating pressures between 10 and 50 MPa and temperatures in the range of 150 to 800°C (Shah; Sekulic, 2003). Besides the main types of flow arrangements, i.e. parallel flow, counter flow and cross flow, a combination of these arrangements with multi-pass schemes and multi-streams are possible (Hesselgreaves; Law; Reay, 2016). The two main types of flow paths are continuous and discontinuous. Straight channel (Chen et al., 2016a) and zigzag-channel (Nikitin; Kato; Ngo, 2006) are examples of continuous flow paths, while S-shaped fins (Tsuzuki; Kato; Ishiduka, 2007) and airfoil (Kim et al., 2008) are examples discontinuous channels. Figure 5(a) shows a micrograph of the semi-circular cross-section channels etched plates, and in (b) a schematic diagram with some PCHE flow channels is shown.

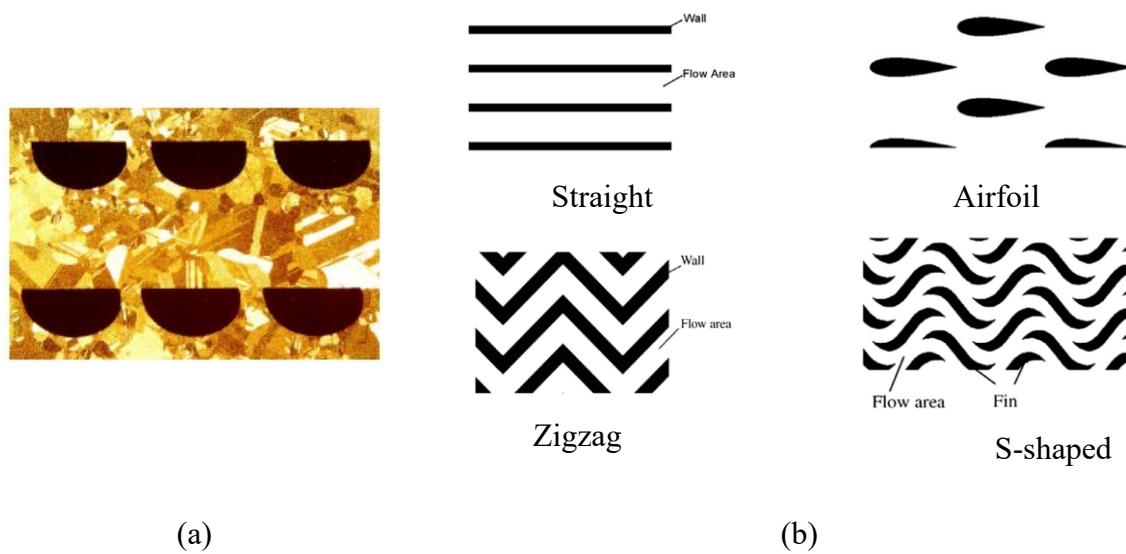


Figure 5 – (a) Micrograph of a PCHE with semi-circular cross-section channels and (b) Schematic diagram of flow channels. (David Southall, 2008; Huang et al., 2019)

PCHEs have been successfully used with gases, liquids and phase-change fluids, among the chemical processing, fuel processing, waste heat recovery, power and energy and refrigeration industries (Shah; Sekulic, 2003). PCHEs are also extensively used in offshore gas and oil platforms (Heatric, Access date: May 27, 2021; Shah; Sekulic, 2003). Besides these proven successful applications, PCHEs have a large potential to be used in other fields, such as advanced nuclear reactors (Chen et al., 2016b), steam generators in nuclear applications (Haratyk; Shirvan; Kazimi, 2015), concentrated solar power (Wang et al., 2019), etc.

Similar to the above presented printed-circuit heat exchanger (PCHE), diffusion-bonded heat exchanger (DBHE) have been successfully produced and tested at *Labtucal* (Mortean et al., 2016; Mortean; Paiva; Mantelli, 2016). As aforementioned, PCHEs are named after the metal sheet plates machining process, in which semi-circular channels are chemically etched. However, in the DBHEs developed at *Labtucal*, a water-jet cutter machine is employed to cut slits in plates, which are piled against full plates to form rectangular or square cross-section channels (Mortean et al., 2016; Mortean; Paiva; Mantelli, 2016). These plates are posteriorly stacked and bonded by diffusion bonding technique. Theoretical calculations of thermal-hydraulic performance of square-cross section DBHEs were conducted by Sarmiento et al. (2020a), showing good agreement with experimental results. This manufacturing process

permits innovative channel geometry designs, as addressed by researchers in the literature (Mortean et al., 2016; Mortean; Paiva; Mantelli, 2016; Sarmiento et al., 2020a).

### **2.2.1 Printed-circuit heat exchanger literature review**

Among the different applications addressed by researchers in which the use of PCHEs arises interest, supercritical CO<sub>2</sub> (S-CO<sub>2</sub>) Brayton cycles stand out on the scrutiny of scientific society. Indeed, S-CO<sub>2</sub> power cycles can be considered as alternatives among the conversion cycles, as the carbon-dioxide fluid characteristic, at its supercritical state, simultaneously presents liquid- and gas-like properties (high density and low viscosity) (Baik et al., 2017; Dostal, 2004). More specifically, the S-CO<sub>2</sub> Brayton cycle comprises both the Rankine and the Brayton cycles advantages, achieving high efficiency due to low pumping power near the critical point and higher inlet turbine temperature (Ahn; Lee, 2014). Therefore, the components of this cycle, such as compressors and heat exchangers, are subject to high pressures and temperatures. DBHEs present themselves as good candidates for these applications as they can bear extreme operation conditions.

Nikitin; Kato and Ngo (2006) experimentally investigated the heat transfer and the pressure drop characteristics of a zigzag PCHE in an S-CO<sub>2</sub> loop. Empirical correlations to predict the local heat transfer coefficient and pressure drop factor were proposed. Ngo et al. (2007) experimentally evaluated and compared the thermal-hydraulic characteristics of a fin S-shape PCHE and a zigzag-shape channel geometry, both in S-CO<sub>2</sub> loops. Empirical correlations for the Nusselt numbers and the friction factors were proposed. The results showed higher Nusselt numbers for the zigzag geometry, at the cost of higher pressure drops. Kim et al. (2008) numerically analyzed the heat transfer and the pressure drop characteristics of S-CO<sub>2</sub> flow in PCHEs. A zigzag geometry channel and a new air-foil-shaped fin were simulated and their results were compared. Similar heat transfer performance was obtained for the geometries, although the pressure drop factor was reduced in the air-foil-shaped fin, due to suppression of flow separation at the fin's surface. To quantify the effects of the thermal enhancement and the pressure losses, Guo and Huai (2017) conducted an entropy generation analysis in a straight channel PCHE employed as the regenerator of an S-CO<sub>2</sub> Brayton cycle. According to the authors, the total entropy generation is mostly caused by heat transfer irreversibility, with low friction force contributions. Saeed and Kim (2017) numerically compared different zigzag

PCHEs concluding that the thermal performance of 100° zigzag channel is higher when compared to a 130°.

As noted by Cheng et al. (2020), only a few studies on DBHEs used as a pre-cooler for S-CO<sub>2</sub> cycles are available, especially concerning the influence of the cold fluid on the cycle. In this configuration, before entering the compressor, S-CO<sub>2</sub> is cooled by a pre-cooler PCHE, which transfers energy to the water, on the cold side. Saeed et al. (2020) highlighted the great difficulty of finding Nusselt heat transfer correlations for zigzag channels' PCHE operating with water as working fluid. As demonstrated by Sarkar (2009), the efficiency of the cycle was more susceptible to the minimum compressor inlet temperature than to its maximum. Therefore, the knowledge of the pre-cooler thermal behavior, particularly the influence of its cold fluid flow (water), is of major importance to the design of Brayton cycles.

Kim and No (2011) experimentally investigated the thermal-hydraulic performance of a PCHE with zigzag channels in a helium-water configuration, operating in the laminar region. The operation range was expanded through numerical simulation to a Reynolds number of 2500, resulting in the proposition of Nusselt number and friction factor correlations. Seo et al. (2015) experimentally evaluated the performance of a straight channel PCHE tested with water as both hot and cold fluids, for Reynolds numbers up to 850. The hot-side inlet temperature was varied, while the cold-side inlet temperature was kept fixed. Empirical correlations were proposed for the heat transfer coefficient and the pressure drop friction factor.

Baik et al. (2017) experimentally and numerically investigated a PCHE operating with CO<sub>2</sub> and water, addressing its use as a pre-cooler in an S-CO<sub>2</sub> cycle. Tests under different inlet mass flow and temperature conditions were performed and heat transfer and pressure drop correlations for the CO<sub>2</sub> side were proposed for a wide range, for Reynolds numbers up to 80,000. However, for the water side, only a limited range of Reynolds numbers, from 50 to 200, was investigated. To extend the correlation range of application, the authors suggest a numerical approach, as described by (Kim et al., 2016). Chu et al. (2017) experimentally investigated the S-CO<sub>2</sub>-water heat transfer characteristics of a straight channel PCHE. A water-water configuration was also tested to find the correlations of the PCHE on the water side. The results showed an acceptable comparison with the Gnielinski correlation.

Cheng et al (2020) experimentally investigated a 100 kW class PCHE used as a pre-cooler for a CO<sub>2</sub> Brayton cycle, with zigzag channel geometry. The authors directed special

attention to the effects of the inlet temperatures and mass flow rates on the water side on the thermal and hydraulic performance of the PCHE. Variations on the heat transfer rate, overall heat transfer coefficient and pressure drop were quantified for the Reynolds number variation, however, no correlations for the heat transfer coefficient were proposed. Saeed et al. (2020) numerically investigated the thermal and hydraulic characteristics of zigzag geometry channels of PCHEs, operating under pre-cooler conditions of an S-CO<sub>2</sub> Brayton cycle. The authors proposed a new set of correlations for heat transfer and friction factor, for both water and CO<sub>2</sub>.

Beyond its use in S-CO<sub>2</sub> Brayton cycles, PCHEs have been also studied with Helium (He) as working fluid, for use as intermediate heat exchangers in very high-temperature reactors (Huang et al., 2019). Kim and No (2012) experimentally investigated a zigzag channel PCHE in a He test loop. A numerical model was validated against the experimental results and used for developing Nusselt number and Fanning friction factor correlations for different zigzag geometries, varying their angle, pitch and diameter. The maximum Reynolds number for the proposed correlations is near 2500. Further tests are realized in Kim and No (2013) experiments, in which a mixture gas with He and CO<sub>2</sub> is used. A Nusselt number and Fanning friction factor correlations are developed based on the He-He, He-Water and mixture-water test data, for a maximum Reynolds number near to 3000.

Mylavarapu et al. (2014) experimentally investigated a semicircular cross-section channel PCHE in a high-temperature He test facility. Pressure drop and heat transfer characteristics comparison with correlations in the literature for a circular duct showed a similar trend, but with lower values of critical Reynolds number marking the switch from laminar regime to transition flow. Chen et al. (2016a) performed experimental steady-state tests in a straight channel PCHE operating in a He loop. Two methodologies for calculating the Nusselt number correlation are proposed and compared, showing good agreement. Chen et al. (2016b), experimentally investigate the performance of a zigzag channel PCHE operating in a He-He configuration. Heat transfer and pressure drop correlations were developed for the tested zigzag geometry, for a maximum Reynolds number of approximately 3558. The zigzag channel showed little thermal advantage when compared with a straight circular channel in the laminar regime, but a significant advantage near the transition flow regime.

### 2.2.2 The diffusion-bonded heat exchanger at *Labtucal*

Mortean et al. (2016) proposed four different fabrication technologies coupled with the diffusion-bonding process of soldering. Sandwich of plates filled with parallel circular wires, rectangular wires, rectangular tubes and water machined plates were manufactured. This last resulted as the most promising fabrication technology. Mortean; Paiva and Mantelli (2016) produced and tested a cross-flow diffusion bonded heat exchanger through the water jet cutting machine technology. Water was used in both hot and cold streams for Reynolds numbers up to near 1230 and good agreement was obtained between experimental data and analytical models.

Carqueja (2017) and Batista (2017) experimentally investigated two similar DBHEs, with close outside dimensions and square cross-section channels, in an air-water test configuration. While the first had straight channels, the second presented a zigzag flow path pattern. Both authors demonstrated that the air's convective resistance was dominant over the water convective and the separating wall conductive resistances. The overall heat transfer coefficient and heat transfer rate were compared with data from the experimental tests performed, in which the air side Reynolds number varied from approximately 2500 to 8000. The zigzag channel provided superior heat transfer capabilities. The air side total pressure drop is reported, in measurements including the heat exchanger core and the fluids distribution devices, e.g. pipes and headers assembly. No Fanning friction factor correlations are reported for the tested geometries.

A complete thermal and pressure drop analysis of a square cross-section channel stainless-steel diffusion-bonded heat exchanger is performed by Mortean et al. (2019). An existing Nusselt number correlation is adapted for square channels, showing good convergence with the data. The heat exchange pressure drop is analyzed accounting for the contribution of the distribution devices. The analysis showed that the headers as responsible for at least half of the heat exchanger pressure drop. Mortean and Mantelli (2019) performed a theoretical and experimental thermal analysis of the laminar and transitional flow in a compact cross-flow diffusion-bonded heat exchanger. A Nusselt number correlation for the transition flow is proposed based on an asymptotic correlation method, which showed good agreement with the experimental data obtained.

Hulse (2020) and Gatti (2020) fabricated and tested a cross-flow PCHE and DBHE, respectively. Both equipment were tested in an air-water configuration. A complete thermal and hydraulic evaluation of the prototypes was presented. The experimental Nusselt number and Fanning friction factor data showed good agreement with Sarmiento et al. (2020b) correlations.

### 2.3 SUMMARY AND SPECIFIC OBJECTIVES

Huang et al. (2019) analysis on PCHEs summarizes the main conclusions drawn for the above literature review. Firstly, it is seen that the studies on PCHEs can be divided into two main groups: (1) to investigate the variation of the convective heat transfer coefficients for different channel geometries and operating conditions; and (2) to research the friction factor coefficient for the engineered channels. Secondly, some existing problems in the literature are concerned with low Reynolds-number flow experiments and few studies conducted with fluids other than CO<sub>2</sub> and He. Saeed et al. (2020) confirm this last observation, stating that most of the literature works on PCHEs are focused on fluids with low Prandtl numbers as most of the heat transfer correlations available are for  $Pr \leq 2.2$ . Besides, Kim et al. (2016) address the lack of high Reynolds number correlations by proposing a numerical approach for the extension of the existing heat transfer and pressure drop correlations.

Beyond these general guidelines, the above literature review also shows that, despite the extensive effort in the thermal-hydraulic characterization of zigzag PCHEs, its application as pre-cooler in S-CO<sub>2</sub> Brayton cycles is still incipient, and consequently water, the cooling working fluid used in this configuration, is poorly explored. Moreover, only a few correlations for high Reynolds numbers range are available. Most of the proposed correlations are based on numerical simulations, and, in these cases, the prescribed boundary conditions, material, and geometrical specifications may diverge from the real equipment operating conditions. Besides, limited data on the transitional and turbulent Reynolds number range are available. To the best knowledge of the present author, in the literature, there is only one correlation numerically developed for non-straight channels of PCHE (Saeed et al., 2020) operating with water, for high Reynolds number range.

Therefore, the present study seeks to contribute to the above research gaps by presenting a complete thermal and hydraulic experimental investigation of a novel DBHE zigzag channel. Two different fluid combinations are tested in this device, i.e. water-water and air-water, under different inlet mass flow conditions.

The specific objectives of the proposed work are the following:

1. To design and manufacture a novel zigzag channel geometry DBHE, with a square-cross section.
2. To provide a complete thermal characterization of the DBHE operating with water as the working fluid, in a Reynolds number range not yet experimentally investigated, by:
  - Covering the transition-to-turbulent and turbulent flow regime, addressing flow conditions poorly explored in the literature for DBHEs operating with water;
  - Evaluating the thermal parameters of the equipment, i.e. heat load, overall heat transfer coefficient, effectiveness and the number of transfer units, and their response to variations in the inlet fluid flow conditions.
  - Proposing a heat transfer correlation through the Nusselt number.
  - Comparing thermal performance with data from the literature.
3. To perform a thermal and hydraulic investigation of the DBHE operating in an air-water fluid configuration aiming the evaluation of the heat transfer enhancement and pressure drop rise in zigzag channels, based on previous studies conducted at LABTUCAL, by:
  - Evaluating the thermal parameters of the equipment and their response to variations in the inlet conditions.
  - Evaluating the pressure drop in the equipment.
  - Proposing a Nusselt number correlation to the air stream.
  - Proposing a Fanning friction factor correlation to the air stream.
  - Comparing with *Labtucal* and literature data.

The final objective is to develop heat transfer and pressure drop correlations for different fluid flow conditions, to guide engineers in the design and optimization of DBHEs. To this end, a review of the mathematical modeling of heat exchangers is revisited in the next chapter.

### 3 HEAT EXCHANGER DESIGN THEORY

This chapter presents the thermal and hydraulic heat exchanger model used in the analysis of the present work. Firstly, the geometrical overview of the heat exchanger's main parameters is presented. Then, the thermal performance theory is presented for the case currently investigated. Finally, a consideration on the analysis of the fluid flow properties for the current work is discussed.

#### 3.1 GEOMETRICAL OVERVIEW

The main geometrical aspects of a heat exchanger are the hydraulic diameter, surface porosity and the surface area density (Hermes, 2018; Hesselgreaves; Law; Reay, 2016), which are defined below.

The hydraulic diameter is defined as:

$$d_h = \frac{4 A_o L}{A}, \quad (3.1)$$

where  $A_o$  is the minimum free flow area for one fluid side,  $L$  is the fluid flow length and  $A$  is the total heat transfer surface area.

The ratio of the free-flow area (or surface porosity) is given by:

$$\sigma = \frac{A_o}{A_{fr}}, \quad (3.2)$$

where  $A_{fr}$  is the frontal area.

Finally, the heat transfer surface area density, defined as the ratio of the heat transfer to the heat exchanger volume,  $\beta = A/V$ , can be written related to the previously presented parameters, as:

$$\beta = 4 \frac{\sigma}{d_h}. \quad (3.3)$$

### 3.2 HEAT EXCHANGER PERFORMANCE EVALUATION

The basic thermal design equations are presented below, considering a two fluids heat exchanger operating in a counterflow arrangement, as shown in Figure 6.

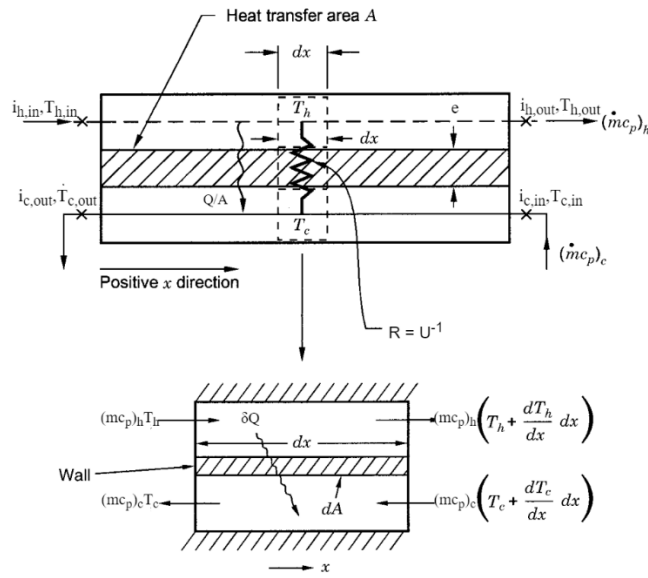


Figure 6 – Counterflow heat exchanger basic thermal parameters. Adapted from (Shah; Sekulic, 2003).

From the energy conservation equation for an open system, steady-state conditions, negligible potential and kinetic energy changes, the change of enthalpy of any of the fluid streams is given by (Kakaç; Liu; Pramuanjaroenkij, 2002):

$$\delta Q = \dot{m} di, \quad (3.4)$$

where  $\dot{m}$  is the mass flow rate,  $i$  is the specific enthalpy and  $\delta q$  is the heat transfer rate associated with the infinitesimal state change. Integration of Equation (3.4) gives:

$$Q = \dot{m}(i_{out} - i_{in}). \quad (3.5)$$

Assuming no heat losses to the ambient, integration of Equation (3.4) for both hot and cold fluids give:

$$Q_h = [\dot{m}(i_{in} - i_{out})]_h, \quad (3.6)$$

$$Q_c = [\dot{m}(i_{out} - i_{in})]_c, \quad (3.7)$$

where subscripts  $h$  and  $c$  stand for the hot and cold side, respectively. Disregarding phase change cases and assuming constant  $c_p$ , Equations (3.6) and (3.7) can be written as:

$$Q_h = [\dot{m}c_p(\Delta T)]_h, \quad (3.8)$$

$$Q_c = [\dot{m}c_p(\Delta T)]_c. \quad (3.9)$$

In experimental set-ups, where the adiabatic assumption may not be guaranteed, the heat transferred by the heat exchanger may be estimated through the arithmetic mean between the heat exchanged from each channel, as shown in:

$$Q_{avg} = \frac{Q_h + Q_c}{2}. \quad (3.10)$$

The overall heat transfer rate equation, for a differential element of area  $dA$  in Figure 6, is (Shah; Sekulic, 2003):

$$\delta Q = U(T_h - T_c)dA = U\Delta T dA, \quad (3.11)$$

where  $U$  is the local overall heat transfer coefficient. By rearranging the previous equation:

$$\int_Q \frac{dq}{\Delta T} = \int_A U dA. \quad (3.12)$$

The mean temperature difference and mean overall heat transfer coefficient are defined as follows (Shah; Sekulic, 2003):

$$\frac{1}{\Delta T_m} = \frac{1}{Q} \int_Q \frac{dQ}{\Delta T'} \quad (3.13)$$

$$U_m = \frac{1}{A} \int_A U dA, \quad (3.14)$$

where the subscript  $m$  denotes the mean value of the property evaluated. The overall heat transfer coefficient is considered as constant through the heat exchanger (Shah; Sekulic, 2003), and by substituting Equations (3.13) and (3.14) in Equation (3.12) yields:

$$Q = UA\Delta T_m. \quad (3.15)$$

An analogy between thermal and electrical entities is used to better understand Equation (3.15). An electric resistance is defined as the ratio between the electric potential difference and the corresponding electric current flow. Therefore, by defining resistance as the ratio between a driving potential and the associated flow rate (Bergman et al., 2011), a thermal resistance is given by  $R = \Delta T/Q$ , which after rearranging gives:

$$Q = \frac{\Delta T}{R}. \quad (3.16)$$

By comparing the corresponding terms in Equations (3.15) and (3.16), the thermal resistance  $R$  is related to the overall heat transfer coefficient as shown in:

$$\frac{1}{UA} = R. \quad (3.17)$$

Adapted from (Lee, 2010), the thermal circuit model of a steady-state counter flow two-fluid heat exchanger is shown in Figure 7.

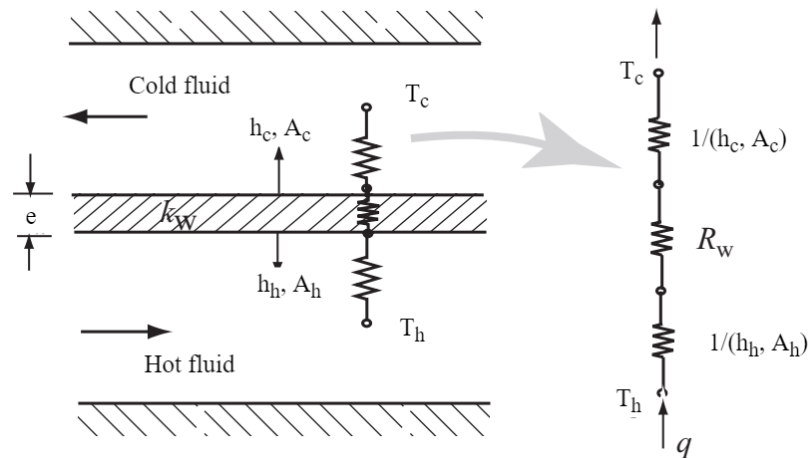


Figure 7 – Thermal circuit model of a counterflow heat exchanger. Adapted from (Lee, 2010).

As seen in Figure 7, heat is transferred from the hot stream to the cold stream by convection in the hot fluid, followed by conduction through the heat exchanger wall, and convection in the cold fluid. Although fouling resistances are not considered in the present case, they would contribute to conduction thermal resistances in their respective channels. The total thermal resistance,  $R_{tot}$ , consists of these corresponding partial resistances coupled in series, given by:

$$R_{tot} = R_{h,conv} + R_{w,cond} + R_{c,conv}. \quad (3.18)$$

The conductive thermal resistance for a flat wall and the convective thermal resistance of a given fluid are defined, respectively, as (Bergman et al., 2011):

$$R_{cond} = \frac{e_w}{k_w A'}, \quad (3.19)$$

$$R_{conv} = \frac{1}{h_i A'}, \quad (3.20)$$

where  $e$  is the thickness,  $k$  is the thermal conductivity,  $A$  is the surface of the wall normal to the heat transfer direction,  $h$  is the convective heat transfer coefficient and the subscripts  $i$  and  $w$  refer to the fluid evaluated and to the wall.

Applying Eq. (3.17) for the case represented in Figure 7 results in:

$$\frac{1}{UA} = R_{tot} = \frac{1}{h_h A} + R_{w,cond} + \frac{1}{h_c A}. \quad (3.21)$$

The mean temperature difference,  $\Delta T_m$ , in Equation (3.15) is determined for a counterflow heat exchanger by applying an energy balance to a differential area element  $dA$  in the hot and cold fluids, as shown in Figure 6. As given by Equations (3.8) and (3.9), and by introducing the heat capacity rate definition,  $C_i = (\dot{m}c_p)_i$ , the energy balance yields:

$$\delta Q = -[CdT]_h = -[CdT]_c. \quad (3.22)$$

From Equation (3.22), the differential temperature difference between the fluids can be written as:

$$dT_h - dT_c = d(\Delta T) = \delta Q \left( \frac{1}{C_c} - \frac{1}{C_h} \right). \quad (3.23)$$

By defining  $\Delta T_1$  and  $\Delta T_2$  as the temperature differences between the fluids at each end of the heat exchanger, in a counterflow arrangement as shown in Figure 6, yields in:

$$\begin{aligned} \Delta T_1 &= T_{h,in} - T_{c,out}, \\ \Delta T_2 &= T_{h,out} - T_{c,in}. \end{aligned} \quad (3.24)$$

Substituting  $\delta Q$  from Equation (3.11) in Equation (3.23), rearranging and integrating over the heat exchanger, with constant values of  $U$ ,  $C_h$  and  $C_c$ ,  $\int_1^2 \frac{d(\Delta T)}{\Delta T} = U \left( \frac{1}{C_c} - \frac{1}{C_h} \right) \int_1^2 dA$  results in:

$$\ln \frac{\Delta T_2}{\Delta T_1} = UA \left( \frac{1}{C_c} - \frac{1}{C_h} \right), \quad (3.25)$$

which by substituting the hot and cold heat capacity definition results in:

$$\begin{aligned} \ln \frac{\Delta T_2}{\Delta T_1} &= UA \left( \frac{T_{c,out} - T_{c,in}}{Q} - \frac{T_{h,in} - T_{h,out}}{Q} \right) = \\ &= \frac{UA}{Q} [(T_{h,out} - T_{c,in}) - (T_{h,out} - T_{c,in})], \end{aligned} \quad (3.26)$$

which solving for Q yields in:

$$Q = UA \frac{\Delta T_2 - \Delta T_1}{\ln (\Delta T_2 / \Delta T_1)}. \quad (3.27)$$

The comparison between Eqs. (3.27) and (3.15) shows that the appropriate average temperature difference for a counterflow arrangement is a logarithmic mean, defined as:

$$\Delta T_{lm} = \frac{\Delta T_2 - \Delta T_1}{\ln (\Delta T_2 / \Delta T_1)}. \quad (3.28)$$

Consequently:

$$Q = UA \Delta T_{lm}. \quad (3.29)$$

The heat exchanger effectiveness,  $\varepsilon$ , measures the thermal performance of a heat exchanger. It is defined as the ratio of the heat transfer of a specific heat exchanger to the maximum heat transfer rate possible, as shown in:

$$\varepsilon = \frac{Q}{Q_{max}} = \frac{Q}{C_{min}(T_{h,in} - T_{c,in})}, \quad (3.30)$$

where  $Q_{max}$  is the maximum heat transfer rate thermodynamically possible, given by  $Q_{max} = \min(C_i) \cdot (T_{h,in} - T_{c,in})$  (Shah; Sekulic, 2003), and  $Q$  is evaluated from Equations (3.8) or (3.9), or Equation (3.10) if the average heat transfer rate is used.

The number of transfer units is defined as the ratio of the overall heat thermal conductance to the minimum heat capacity rate, as in:

$$NTU = \frac{UA}{C_{min}}, \quad (3.31)$$

for constant U.

It can be shown that the effectiveness of a heat exchanger is a function of the flow arrangement, of NTU and of the heat capacity ratio ( $\varepsilon = f(\text{flow arrangement}, NTU, C_{min}/C_{max})$ ) (Kays; London, 1998). By defining  $C_r$  as the ratio of the smaller to the higher heat capacity of a two-fluid heat exchanger,  $C_r = C_{min}/C_{max}$ , the NTU for certain heat exchanger flow arrangements is shown below (Bergman et al., 2011):

$C_r < 1$ , counterflow arrangement:

$$NTU = \frac{1}{C_r - 1} \ln \left( \frac{\varepsilon - 1}{\varepsilon C_r - 1} \right). \quad (3.32)$$

$C_r = 1$ , counterflow arrangement:

$$NTU = \frac{\varepsilon}{1 - \varepsilon}. \quad (3.33)$$

$C_r = 0$ , special case valid for any flow arrangement:

$$NTU = -\ln(1 - \varepsilon). \quad (3.34)$$

### 3.3 FLOW PROPERTIES

The fluid stream mass velocity is defined as

$$G = \rho u_m, \quad (3.35)$$

where  $\rho$  [ $kg \cdot m^{-3}$ ] is the density of the fluid, and  $u_m$  [ $m \cdot s^{-1}$ ] is the fluid mean velocity. The mass flow rate is defined as:

$$\dot{m} = \rho u_m A_o = G A_o. \quad (3.36)$$

The Reynolds number is defined as:

$$Re = \frac{\dot{m} d_h}{\mu A_o}, \quad (3.37)$$

where  $\mu$  [ $kg \cdot m^{-1} \cdot s^{-1}$ ] is the fluid dynamic viscosity.

The fluid properties, i.e.  $\rho$ ,  $\mu$ ,  $c_p$ , are evaluated differently according to the operating conditions of the heat exchanger. Figure 8 shows the idealized temperature distribution of the fluids through the heat exchanger length for a counterflow arrangement with fluids with finite different  $c_p$ , (a), and a special case in which the cold fluid is on phase change ( $c_{p,c} \rightarrow \infty$ ), (b). In the case shown in Figure 8(a), the properties of the fluids are evaluated at the arithmetic average temperature, while in Figure 8(b) the hot fluid properties are evaluated at the log-mean average temperature, as defined by (Shah; Sekulic, 2003):

$$T_{a,lm} = T_s + \Delta T_{lm}. \quad (3.38)$$

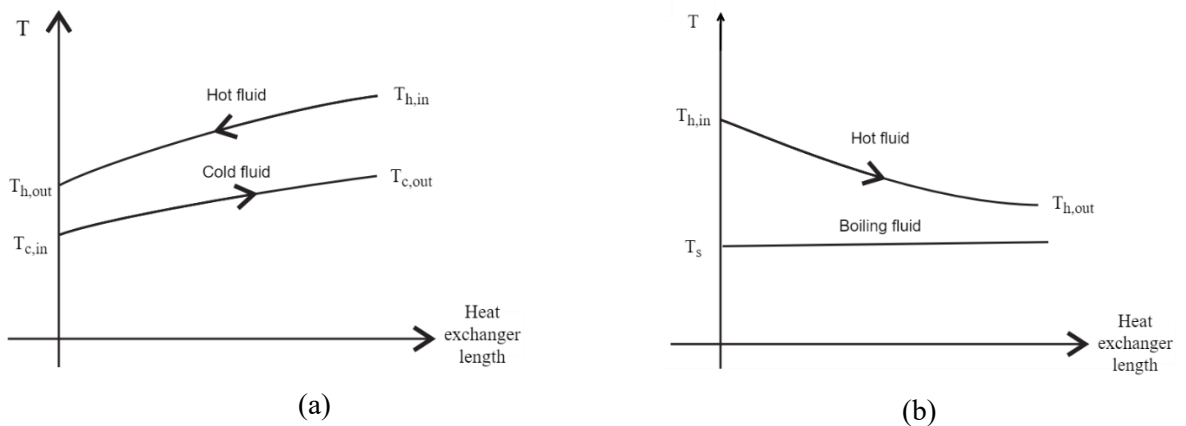


Figure 8 – Temperature distribution of the fluids through the heat exchanger (a) counterflow arrangement, fluids with finite different  $c_p$ , and (b) cold fluid on phase change (boiling) ( $c_{p,c} \rightarrow \infty$ ).

Adapted from (Bejan; Kraus, 2003).

Based on the afore presented theory, the experimental methodology of the present work is discussed in the next chapter.

## 4 EXPERIMENTAL METHODOLOGY

In the present chapter, the experimental methodology for the current investigation is presented. As previously described, the current work aims to thermally and hydraulically characterize a DBHE prototype with a novel channel geometry. Thereby, in the first part of the chapter, the prototype itself is described, presenting its main geometric aspects. After that, the test facility, in which the prototype is tested, is presented, focusing on its general layout and components, followed by the experimental procedure adopted for the tests. Then, the mathematical treatment of the experimental data towards the development of the heat transfer and pressure drop correlations is presented. Finally, considerations for the heat loss and uncertainty analysis of the current work are described.

### 4.1 DBHE FABRICATION

The prototype tested in this work was produced in 316L stainless steel plates. A total of fifteen channels were water machined in these plates with a  $90^\circ$  zigzag angle. Each hot or cold fluid flow layer of channels was formed by a sandwich of non-machined plates, interfiled with a slot plate. To form nine hot and cold layers, eighteen slot plates, intercalated with seventeen non-machined sheets, were stacked. Another two closing plates were added above and below the ensemble. Once assembled, the block was diffusion bonded, to form a solid metal block with the internal channels. Afterward, the excess of material was removed, resulting in the heat exchanger core. The machined plates had a thickness of  $E_p = 3.0 \text{ mm}$  while the non-machined plates have a  $E_i = 1.0 \text{ mm}$  thickness. The final core dimensions are approximately  $350 \text{ mm} \times 135 \text{ mm} \times 83 \text{ mm}$ . Four  $6.5 \text{ mm}$  diameter through-holes were also machined at each corner of the plates, in which pins were inserted before the diffusion bonding process to guarantee the correct alignment of the plates. The hot fluid flows along the longitudinal direction through  $\alpha = 90^\circ$  zigzag channels of a total length  $L_h$ , while the cold fluid paths are composed of  $90^\circ$  zigzag with an “S” shape, of a total length  $L_c$ . Figure 9 illustrates this geometry. The S shape fulfills a manufacturing requirement, avoiding the overlapping of the inlet and outlet fluid ports of both streams. Albeit the different fluid paths, the average hot-side and the cold-side fluids have the same total lengths, i.e.  $L_h = L_c = L$ .

The zigzag channels presented a square cross-section with a nominal width of  $w_c = 3 \text{ mm}$ , fin width of  $w_f = 1.5 \text{ mm}$ , and pitch of  $p = 13.51 \text{ mm}$ . The effective length of the

channels is determined considering the straight direction of the fluid paths,  $L$ , and the zigzag angle:  $L_{eff} = L / \cos \left( 90^\circ - \frac{\alpha}{2} \right)$ . A schematic of the plates and a detailed view of the zigzag channel are shown in Figure 9.

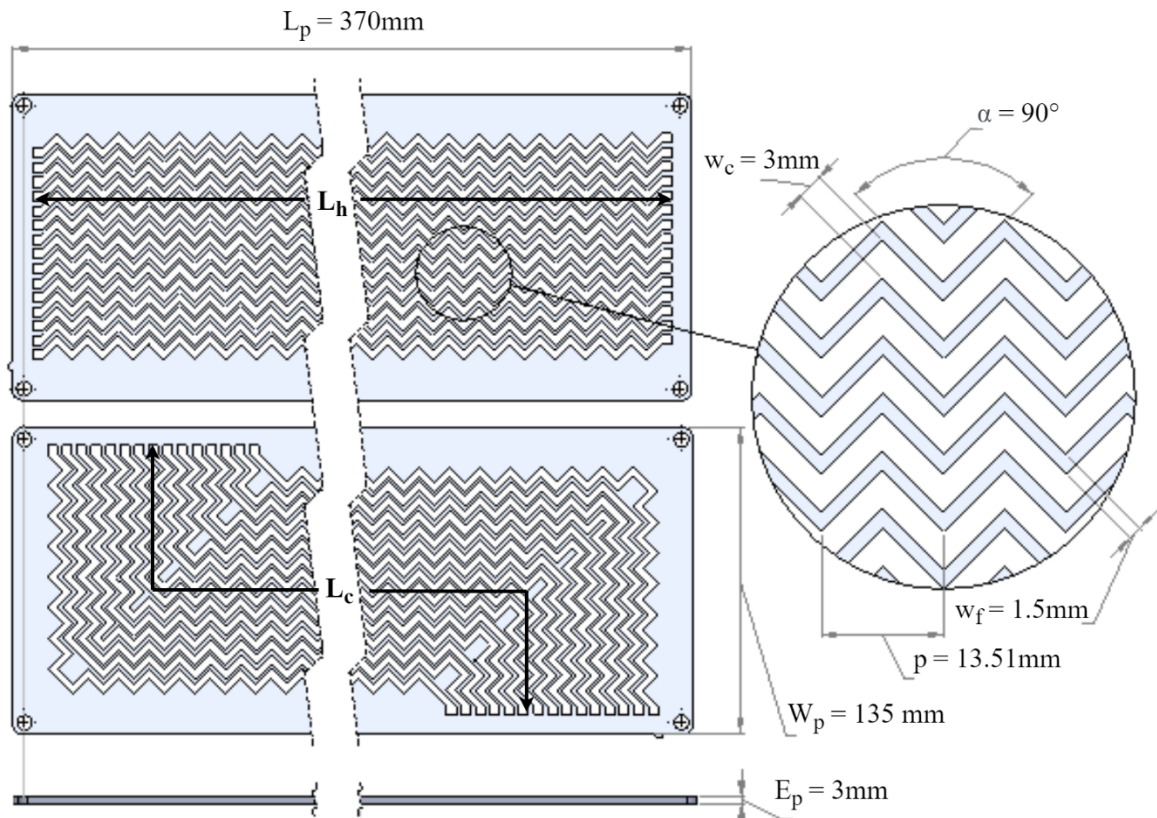


Figure 9 – Hot (above) and cold (below) CAD plate sheets of the manufactured DBHE, and detailed view of the zigzag channel geometry.

The schematics in Figure 10 show an exploded view of the plate's stacking order (a), and an overview of the resulting heat exchanger core (b), highlighting the square cross-section geometries of the hot (red) and cold (blue) channels.

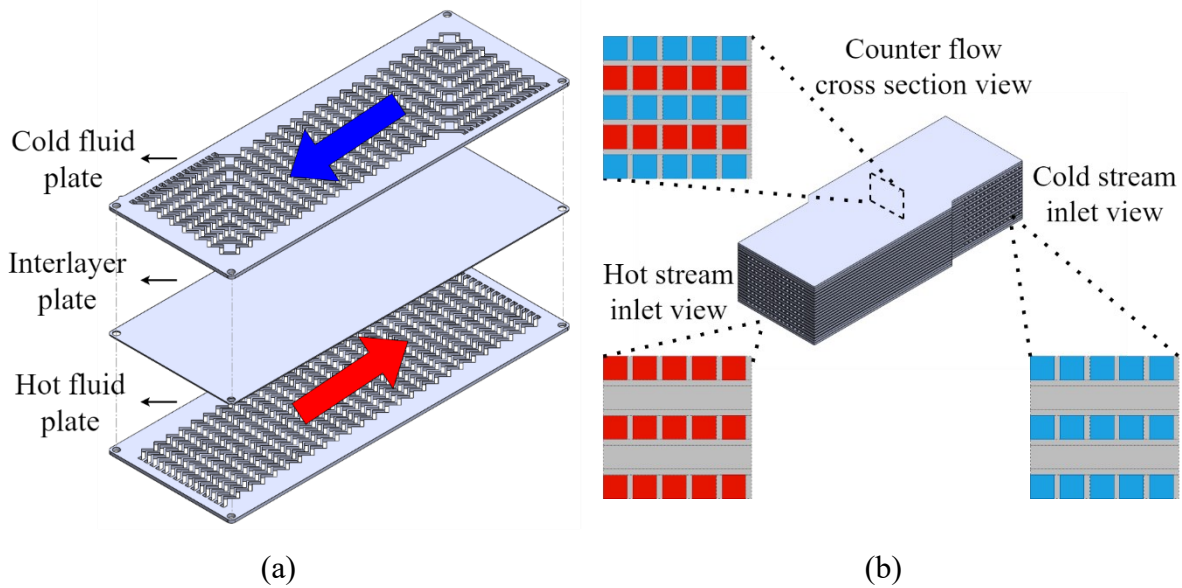


Figure 10 – Schematics of the heat exchanger's plate order and fluid direction (a) and the final core, (b), with detailed views of the channels' distribution at the entrance of each stream and cross-section view.

Figure 11(a) shows a schematic of the cross-section view of the cold fluid entrance, indicating the channels' main dimensions. The asterisk notations in the widths of the channel and wall are related to the transversal directions, as shown in Figure 11 (b). The channel width and the wall width are calculated as  $w_c = \sin\left(\frac{\alpha}{2}\right) \cdot w_c^*$  and  $w_f = \sin\left(\frac{\alpha}{2}\right) \cdot w_f^*$ , where  $\alpha$  is the zigzag angle. One should note that the channel height and the interlayer plate thickness,  $E_p$  and  $E_i$ , are not influenced by the zigzag angle. The channel and layer dimensions described in Figure 11 (b) are also valid for the cold fluid outlet port and the hot fluid inlet and outlet ports.

The fluid is supplied at the entrance and discharged at the exit through a header assembly. The inlet header assembly is composed of a divergent nozzle, two perforated plates, and a spacer frame. The outlet header assembly is composed of a convergent nozzle and a spacer frame. Figure 12 shows detailed views of the inlet header assembly (a), and the final heat exchanger assembly (b). The divergent nozzle is responsible for the transition from circular to rectangular cross-section areas, from the pipe line to the heat exchanger entrance. Since the cross-section change occurs abruptly, the liquid would not be evenly distributed along the transition cross-section area, resulting in a mass flow rate concentration at the center, with lower rates at the edges and corners of the rectangular section. To mitigate this problem, perforated plates are installed downstream of the divergent nozzle to redistribute the fluid along the section at the entrance of the heat exchanger channels, separated by a frame. As no uniform mass

distribution is required at the outlet of the heat exchanger, no perforated plates are used, so that the header assembly is simpler, composed only of a spacer frame and a convergent nozzle. To ensure the modularity of the assembly, the aforementioned parts of the headers are fixed through an external frame and bolt assembly to a flange welded to the heat exchanger core structure. Rubber gaskets are used between parts, to avoid leakages.

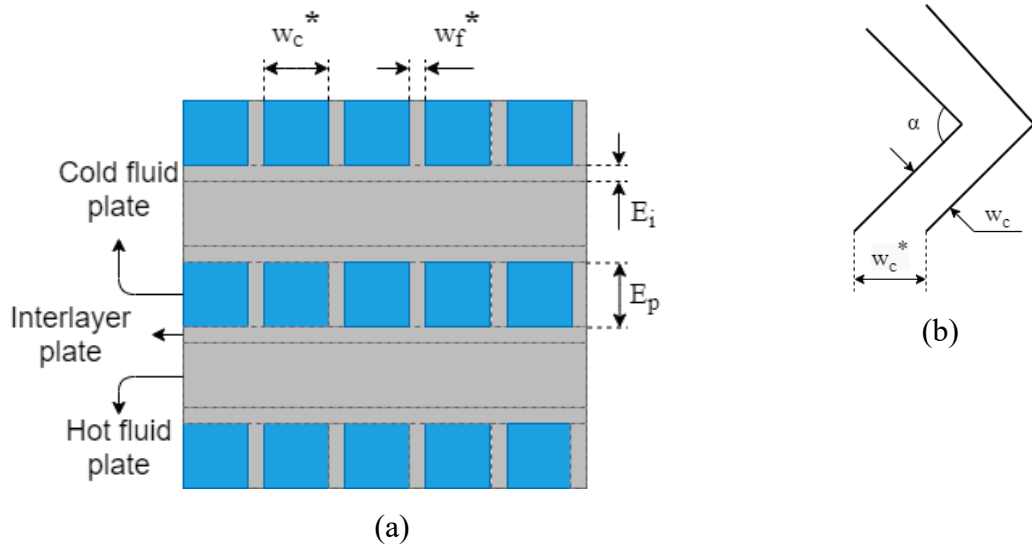


Figure 11 – (a) Schematic of the inlet cold view indicating the channels' main dimensions when seen perpendicularly to the entrance and (b) clarification of the channel width asterisk notation with respect to the channel zigzag angle.

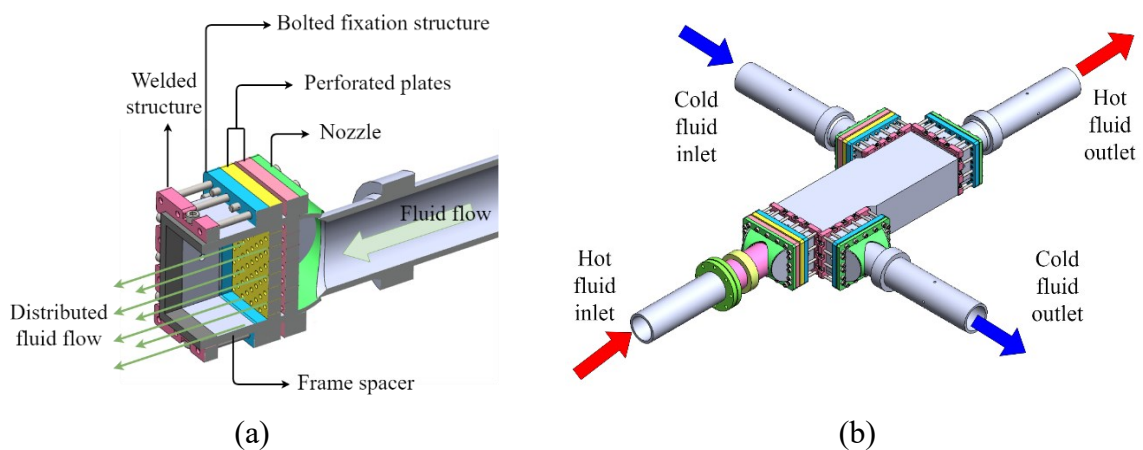


Figure 12 – Schematics of the inlet header assembly cross-section view (a) and the final heat exchanger test section (b).

## 4.2 TEST FACILITY

The test facility used to perform thermal-hydraulic tests in compact heat exchangers was available at the Heat Pipe Laboratory of the Federal University of Santa Catarina. Plate-type and diffusion-bonded heat exchangers were successfully tested in previous works in water-water (Ferreira, 2019) and air-water (Batista, 2017; Carqueja, 2017) configurations. However, Cavalcanti Alvarez et al. (2019) reported in a revisited work analyzing the air-water data that the air stream line was influenced by heating due to the testing apparatus. Indeed, parasitic heat from the motor of the centrifugal fan used to pump air through the line, heated the fluid (gas). This effect increased with increasing air flow. To work around this problem, the original set-up was modified to maintain the tests at a constant temperature. Understanding that there would be a maximum operating temperature when the fan was at its maximum flow, an electric heater was designed and coupled downstream of the fan, to maintain all the tests, including those with low mass flow, at the constant maximum temperature that would be reached in the maximum air flow. The air suction temperature at the inlet of the fan varied according to the ambient temperature, and the electric heater maintained the constant outlet temperature through a PID controller.

Next, the hot-air, hot-water and cold-water setups are presented. These stream setups compose the testing apparatus, for both configurations: water (cold stream)/water (hot stream) and air (hot stream)/water (cold stream).

i. Water cold-stream

The water cold-stream setup consists of a cooling-tower (Korper series-R) open to the atmosphere, a magnetic flowmeter (Rosemount-8732), water distribution pipes, rubber hoses, pipe fittings (valves, elbows, among others) and temperature sensors. Figure 13 shows the simplified layout of the cold-branch facility. The pumps of the cooling-tower are responsible for generating the necessary pressure difference for the fluid to flow through the cold line. The water leaves the cooling-tower in (0), passes through the magnetic flowmeter (1) the heat exchanger (2), where it receives energy from the hot stream and returns to the cooling-tower in (3) to be chilled. The mass flow rate is regulated through the opening and closure of the valves for the different test conditions.

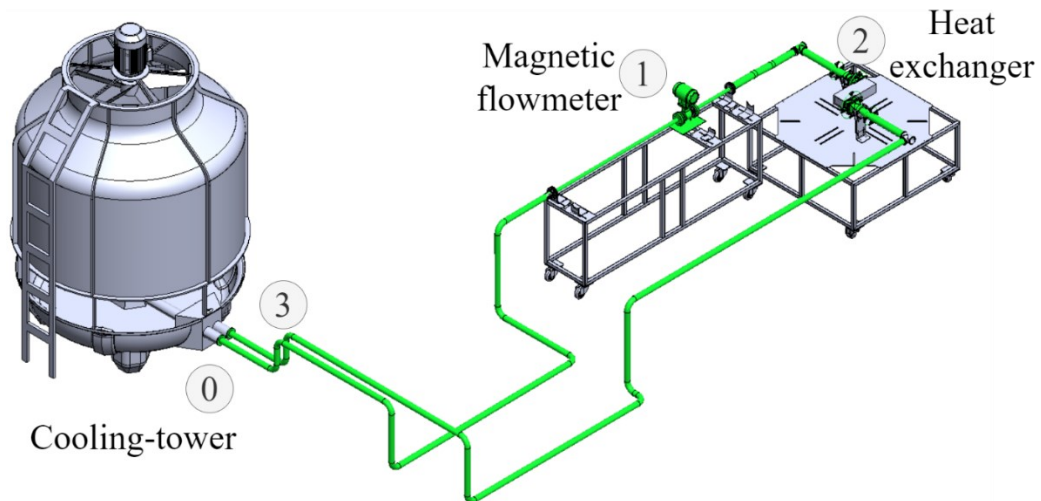


Figure 13 – CAD view of the cold-branch of the test facility.

ii. Water hot-stream

The water hot-stream line is composed of a water tank vented to the atmosphere, a hydraulic pump, an electric heater (heating capacity of 70 kW), a magnetic flowmeter (Rosemount-8732), water distribution pipes and rubber hoses, pipe fittings (valves, elbows, among others) and temperature sensors. Figure 14 shows the simplified layout of the hot-stream assembly. The water is heated by the electric heater in 0 and passes through the magnetic flowmeter in 1. Then the water flows through the heat exchanger 2, where it is cooled, and back to the water tank, 3, placed above the line by a structure. By gravity, the water reaches a hydraulic pump in 4, where it is pressurized again, re-entering in the electric heater to be warmed up and continue through the line. A frequency converter controls the hydraulic pump speed and provides the necessary pressure that pushes the water mass flow through the hot-stream line.

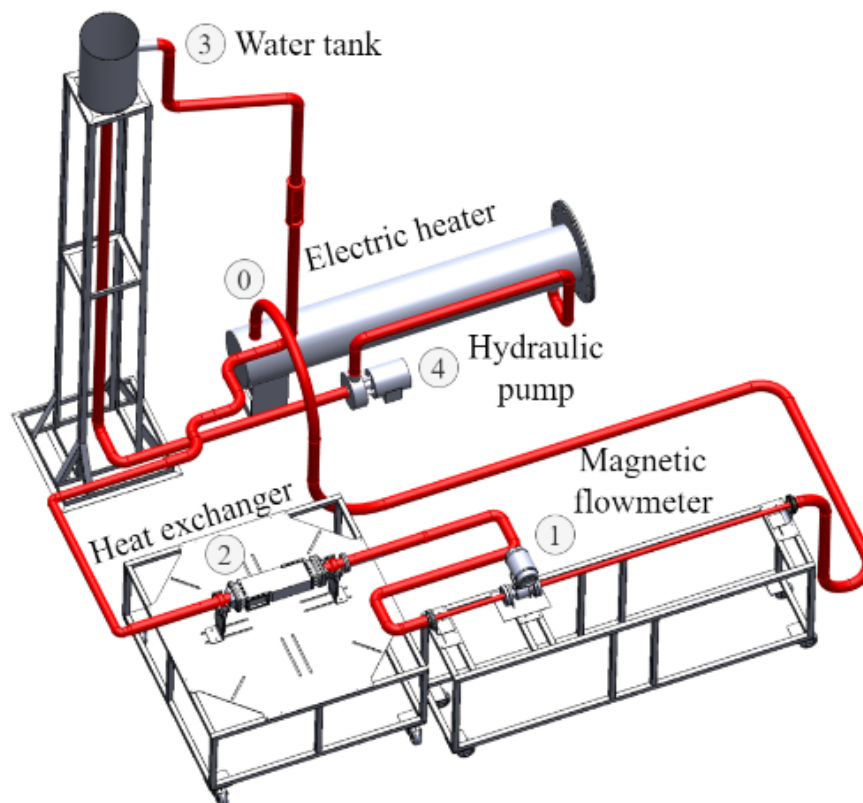


Figure 14 – CAD view of the hot-branch of the test facility.

iii. Air hot-stream

The air hot-stream line is composed of a centrifugal fan, an electric heater (heat capacity of 100 kW) and a Coriolis flow meter (ELITE® CMF200M). In this configuration, seen in Figure 15, the centrifugal fan generates the necessary pressure difference for the air to flow from the fan to the exit of the heat exchanger, discharging to the atmosphere. Departing from the fan, 0, the air passes through a pre-heater, 1, continuing to the Coriolis flow meter at 2 and arrives at the heat exchanger, 3. A frequency converter controls the fan's rotor speed, regulating the air mass flow rate.

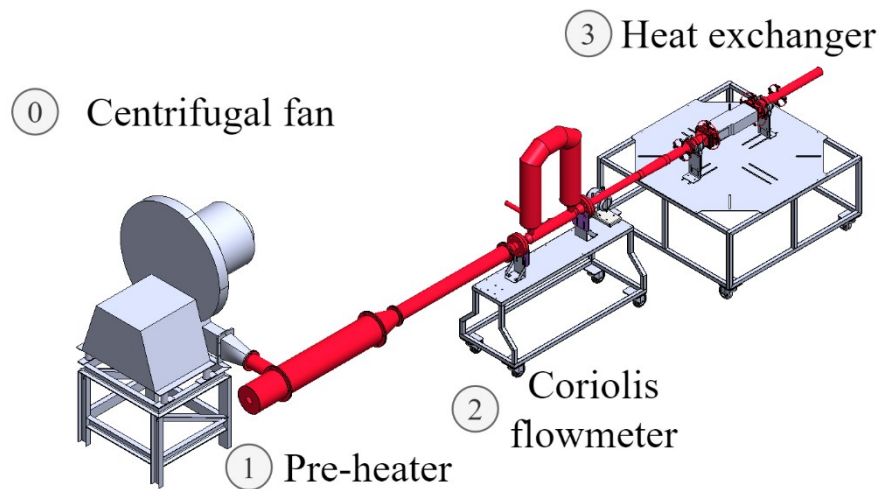


Figure 15 – CAD view of the hot-branch of the test facility.

The heat exchanger prototype was tested under two different flow configurations: water-water and air-water. In both configurations, the inlet and outlet fluid temperatures were measured with four RTD sensors (Omega, PT100) placed upstream and downstream of the heat exchanger's hot and cold branches. The pressure drop along the heat exchanger was evaluated through a differential pressure transducer (Omega, PX409) positioned upstream and downstream of the hot stream core. Different range-scale transducers were used for each fluid. The sensors used in the test were previously calibrated. The test section, composed of the heat exchanger, headers, inlet and outlet pipes, was thermally insulated to reduce the heat loss to the ambient. The tests were performed in steady stated conditions, which was considered achieved when the fluctuation of the temperature and flow rates were below the equipment uncertainty

for 5 minutes. The data acquisition system collected a total of 600 data points during 10 minutes testing period, for all tested configurations. A photograph of the experimental setup, in its water-water layout, is shown in Figure 16.

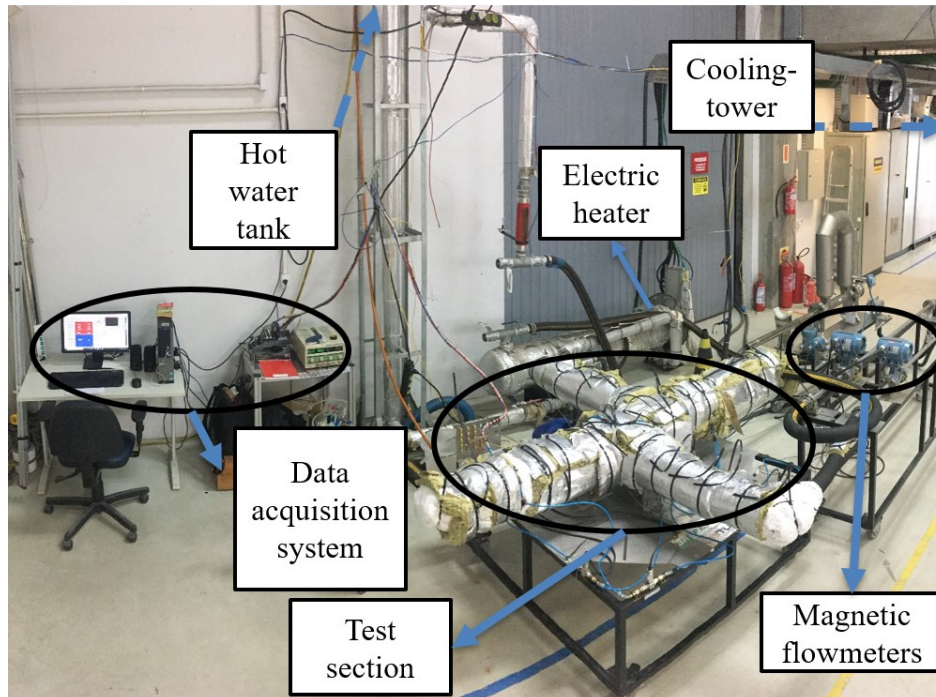


Figure 16 – Experimental water-water setup photograph.

#### 4.3 EXPERIMENTAL PROCEDURE

The experimental testing procedure followed the same principles for both water-water and air-water layout configurations. The water-water test procedure is briefly described hereafter. The mass flow rate for hot and cold streams varied in the range from  $0.4$  to  $1.9 \text{ kg} \cdot \text{s}^{-1}$  and from  $0.4$  to  $2.15 \text{ kg} \cdot \text{s}^{-1}$ , respectively, with increments of  $0.25 \text{ kg} \cdot \text{s}^{-1}$ . For a specific cold mass flow rate, the hot mass flow varied from a minimum to a maximum value, with equal steps. Once, for a specific cold mass flow rate, the device was tested for all hot mass flow rates, the cold flow rate was incremented, following the same hot mass flow increments. Every set of experiments consists of a given cold mass flow rate value, with the variation of the hot fluid flow rate from the minimum to the maximum values. The hot-stream inlet temperature was set at  $T_{hot,in} = 49^\circ\text{C}$  by the electric heaters. Since the cooling-tower is open to the ambient, the inlet cold temperature at the heat exchanger depends on the weather conditions and fluctuated around  $T_{cold,in} = 24^\circ\text{C} \pm 1.6^\circ\text{C}$  for the water-water layout, among

the different sets of experiments. However, during each test, the mean temperature variation was  $0.10\text{ }^{\circ}\text{C}$ , not impacting the experimental results.

The detailed experimental test conditions are given in Table 1. The thermophysical properties of the fluids are evaluated with the CoolProp database (Bell et al., 2014).

Table 1 – Water-water experimental test conditions.

Set number	1	2	3	4	5	6	7	8
Cold stream mass flow rate (water) (kg/s)	0.40	0.65	0.90	1.15	1.40	1.65	1.90	2.15
Hot stream mass flow rate (water) (kg/s)	0.40-1.90 with 0.25 kg/s increments (total of seven tests per set of experiments)							
$T_{hot,in} = 49^{\circ}\text{C}$								
$T_{cold,in} \cong 24^{\circ}\text{C}$								

As above mentioned, the air-water testing procedure was similar to the one just mentioned. The detailed air-water experimental test conditions are given in Table 2.

Table 2 – Air-water experimental test conditions.

Set number	1	2	3	4	5	6	7	8	9
Cold stream mass flow rate (water) (kg/s)	0.40	0.65	0.90	1.15	1.40	1.65	1.90	2.15	2.40
Hot stream mass flow rate (air) (kg/s)	0.0066-0.0206 with 0.002 kg/s increments (total of eight tests per set of experiments)								
$T_{hot,in} = 75^{\circ}\text{C}$									
$T_{cold,in} \cong 24^{\circ}\text{C}$									

#### 4.4 NUSSELT NUMBER CORRELATION DATA REDUCTION METHOD

Local fluid temperature measurements inside the channels were not performed. However, inlet and outlet stream temperatures are available, so that an average heat transfer coefficient can be obtained. Different methodologies are presented in the literature and, despite their particularities, they commonly rely on the comparison between the theoretical and the experimental overall thermal resistances (Chen et al., 2016a; Chen et al., 2016b; Kim; No, 2011; Ngo et al., 2007). In the present study, the experimental overall thermal resistance is calculated with the aid of Equation (3.29), which is rearranged as:

$$U_{exp} = \frac{q}{A\Delta T_{lm}} \quad (4.1)$$

Three different experimental cases are explored here. First, a heat exchanger operating with similar fluids and conditions, implying similar convective thermal resistances in the hot and cold channels. Next, a special case in which one of the fluid's convective thermal resistance can be disregarded is discussed. This case may occur when steam or other fluid which experiences small temperature variation is used. The third scenario discussed is that in which the heat transfer coefficient of one of the fluids is known *a priori*.

i. Similar convective thermal resistances among the fluids (model 1)

The overall thermal resistance of the heat exchanger is given by (Shah; Sekulic, 2003):

$$\frac{1}{(UA)_{the}} = \frac{1}{(hA)_h} + R_w + \frac{1}{(hA)_c}. \quad (4.2)$$

For the prototype analyzed in this work, the hot-side and the cold-side heat transfer areas can be considered as the same, i.e.  $A_h = A_c = A$ . Therefore, Eq. (4.2) can be rewritten as:

$$\frac{1}{U_{the}} = \frac{1}{h_h} + R_w A + \frac{1}{h_c}. \quad (4.3)$$

The Nusselt numbers of flows within channels are usually described as a function of Reynolds and Prandtl numbers, given by:

$$Nu_i = \mathbb{C}_i Re^{a_i} Pr^{b_i}, \quad (4.4)$$

where  $\mathbb{C}$ ,  $a$ , and  $b$  are constants, and subscript  $i$  refers to the fluid stream evaluated, i.e. hot or cold stream. The Nusselt number is also defined as:

$$Nu \equiv \frac{hd_h}{k}, \quad (4.5)$$

where  $k$  [ $W \cdot m^{-1} \cdot K^{-1}$ ] is the thermal conductivity of the fluid.

Following the methodology described by the authors: (Chen et al., 2016a; Chen et al., 2016b; Ngo et al., 2007), since the fluid paths have equal geometrical configurations and operate with the same fluid at similar conditions, the Nusselt number correlations are assumed to be identical. Therefore, the constants for the hot and cold streams are reduced to:  $\mathbb{C}_h = \mathbb{C}_c = \mathbb{C}$ ,  $a_h = a_c = a$ , and  $b_h = b_c = b$ . The substitution of Eqs. (4.4) and (4.5) in Eq. (4.3) yields in:

$$\frac{1}{U_{the}} = \frac{d_h}{\mathbb{C}(Re^a Pr^b k)_h} + R_w A + \frac{d_h}{\mathbb{C}(Re^a Pr^b k)_c}. \quad (4.6)$$

The three unknowns  $\mathbb{C}$ ,  $a$ , and  $b$  are solved using a non-linear regression method to minimize the difference between the experimental and the theoretical overall thermal resistance,  $S$ , using the expression:

$$S = \sum \left( \frac{1}{U_{exp}} - \frac{d_h}{\mathbb{C}(Re^a Pr^b k)_h} - R_w A - \frac{d_h}{\mathbb{C}(Re^a Pr^b k)_c} \right)^2. \quad (4.7)$$

The first term of the summation is calculated from Eq. (4.1).

In the above methodology, referred to as the *indirect method* (Chen et al., 2016a), the Reynolds number for the hot and cold sides are not restricted to equal values, as long as the convective thermal resistances are of the same order of magnitude.

Finally, the Nusselt number correlation for the hot or cold fluid stream is given by Eq. (4.4), with the respective constants  $\mathbb{C}$ ,  $a$ , and  $b$  evaluated through the minimization of  $S$  in Eq. (4.7).

ii. Negligible convective thermal resistance of one fluid (model 2)

For the current analysis, Eq. (4.3) is rewritten for the case in which the cold fluid convective thermal resistance is negligible compared to the wall and hot fluid thermal resistances, i.e.  $\frac{1}{(hA)_c} \ll \frac{1}{(hA)_h} + R_w$ , resulting in:

$$\frac{1}{(UA)_{the}} = \frac{1}{(hA)_h} + R_w. \quad (4.8)$$

Similar to the previous procedure, Eqs. (4.4) and (4.5) are used for the hot side thermal resistance in Eq. (4.8), yielding:

$$\frac{1}{U_{the}} = \frac{d_h}{\mathbb{C}(Re^a Pr^b k)_{h,air}} + R_w A, \quad (4.9)$$

and the unknowns  $\mathbb{C}$ ,  $a$  and  $b$  are solved through the minimization of  $S$  in:

$$S = \sum \left( \frac{1}{U_{exp}} - \frac{d_h}{\mathbb{C}(Re^a Pr^b k)_h} - R_w A \right)^2. \quad (4.10)$$

iii. Different thermal resistances between the fluids, with one of the convective heat transfer coefficients known a priori (model 3)

This procedure is similar to the first case discussed (model 1), with the difference that the convective thermal resistance of one of the fluids streams is known a priori. Assuming that is the case for the water side, the substitution of Eqs. (4.4) and (4.5) in Eq. (4.3) yields in:

$$\frac{1}{U_{the}} = \frac{d_h}{\mathbb{C}(Re^a Pr^b k)_h} + R_w A + \frac{1}{(Nu k)_c}. \quad (4.11)$$

In the present case, the only unknowns are related to the hot fluid side,  $\mathbb{C}$ ,  $a$ , and  $b$ , while the cold fluid thermal resistance can be calculated through its heat transfer coefficient, in this case, represented by the Nusselt number. These hot side unknowns are solved using a non-linear regression method to minimize the difference between the experimental and the theoretical overall thermal resistance,  $S$ , as shown in:

$$S = \sum \left( \frac{1}{U_{exp}} - \frac{d_h}{\mathbb{C}(Re^a Pr^b k)_h} - R_w A - \frac{1}{(Nu k)_c} \right)^2. \quad (4.12)$$

For the three cases presented, the Prandtl number can be incorporated to a constant if it does not vary significantly (Nikitin; Kato; Ngo, 2006), i.e., Eq. (4.4) can be written as  $Nu_i = \mathbb{C}_i Re^{a_i}$ .

The second and third methodologies presented to the calculus of the heat transfer coefficient (models 2 and 3) are very similar to the mathematical model proposed by (Kays; London, 1998). In this experimental technique, the characterization of compact heat exchanger surfaces, i.e. proposition of  $Nu$  and  $f$  correlations, is described. As presented by (Shah; Sekulic, 2003), this procedure is generally done in a crossflow heat exchanger, with a high heat capacity rate fluid in the “known fluid side”, for which the heat transfer rate is previously known. Generally, steam, chilled water, hot water or oils are used in this side, resulting in high values of  $(hA)_{known\ side}$ . On the “unknown fluid side”, whose heat transfer is to be determined, the fluid is generally air. The mathematical development is the same as the one presented above, and consists of neglecting the thermal resistance on the known side due to its high value of  $(hA)$  face to the unknown side. As reported by (Shah; Sekulic, 2003), this method can become quite inaccurate if the temperature measurement is inaccurate, and hence it is generally not used for high ( $>3$ ) or low ( $<0.5$ ) core  $NTU$ .

Indeed, to reduce the experimental uncertainty on the heat transfer coefficient, the following precautions must be taken, as proposed by (Shah; Sekulic, 2003): first, the thermal

resistances of the known side and the wall must be kept as small as possible, approaching a uniform wall temperature condition. Second, the  $NTU$  range for testing is generally restricted to  $0.5 < NTU < 3$ , or between  $40\% < \varepsilon < 90\%$ . For a given core, high  $NTU$  values occur at low airflow values, resulting in more inaccurate flow rate and temperature measurements. Since  $\varepsilon - NTU$  curves are very flat at high  $NTU$  values, the inaccuracies in the effectiveness will have a large impact on the  $NTU$  values and hence in the heat transfer coefficient,  $h$ , and in the Colburn factor,  $j$ , defined as  $j = Nu \cdot Pr^{-\frac{1}{3}} \cdot Re^{-1}$ . Indeed, this phenomenon is referred to as rollover or drop-off in  $j$ , since the  $j$  vs.  $Re$  curves drops off with decreasing Reynolds values, as shown in Figure 17.

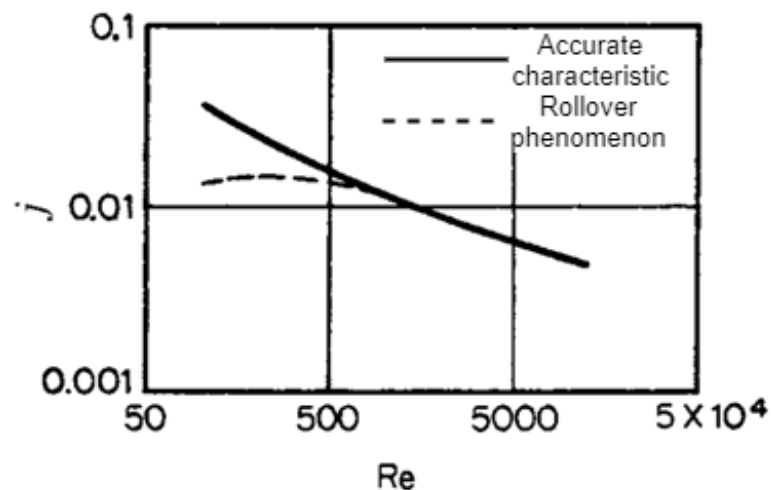


Figure 17 – Rollover (or drop-off) phenomenon in a  $j$  vs.  $Re$  characteristic of a heat exchanger surface. Adapted from (Shah; Sekulic, 2003).

#### 4.5 FANNING FRICTION FACTOR CORRELATION DATA REDUCTION METHOD

The flow friction characteristic of an unknown heat exchanger geometry may be determined through the evaluation of the following experimental measurements: core pressure drop, inlet and outlet fluid flow temperatures and inlet or outlet fluid flow pressures. The methodology presented in (Shah; Sekulic, 2003) is followed in the current work and relies on the evaluation of the different pressure drop contributions of the fluid flow along its passage through the heat exchanger core. These different pressures drop contributions are presented hereafter, before the reduction of the Fanning friction factor.

It is important to highlight that the following methodology is based on the measurement of the heat exchanger core pressure drop. If this portion cannot be experimentally

measured without the influence of fluid distribution elements, e.g. pipe losses, headers or bents, their respective contributions have to be taken into consideration. If this is the case, the measured pressure drop can be divided in:

$$\Delta P_{measured} = \Delta P_{total\ core} + \Delta P_{others}, \quad (4.13)$$

where  $\Delta P_{total\ core}$  is the total pressure drop contribution due to the heat exchanger core, and  $\Delta P_{others}$  refers to fitting and fluid distribution devices. Next, the core total pressure drop is discussed, followed by the pressure drop due to other components.

Based on (Shah; Sekulic, 2003) schematics, Figure 18 shows the one fluid flow passage through a channel in a plate-fin heat exchanger, along with its static pressure distribution. From 1 to 4, the fluid flow contracts at the entrance due to the free-flow area reduction, followed by flow separation and irreversible free expansion in its reattachment to the wall. In its passage through the core, the fluid experiences skin friction, and it may also be susceptible to the drag of an interrupted fin surface. Furthermore, the fluid density can be affected by heating or cooling that may happen during its passage through the core, causing velocity changes, i.e., fluid acceleration or deceleration may be observed. Finally, at the core's exit, free expansion of the fluid flow takes place, caused by the free-flow area's abrupt change.

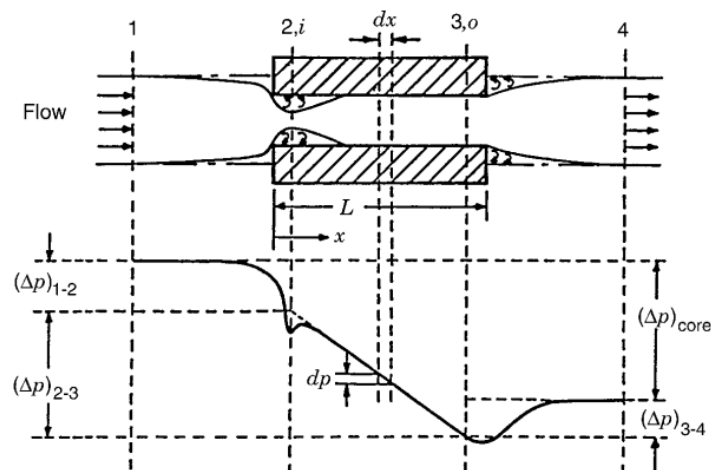


Figure 18 – Pressure drop along a heat exchanger channel. Adapted from (Shah; Sekulic, 2003).

Therefore, in its passage through the core, the fluid flow undergoes pressure drops, pressure rises and pressure losses. While pressure drops and rises are associated with the flow area change and momentum rate change (this last one is due to fluid density variation), pressure losses occur due to irreversibilities of the fluid flow, such as skin friction or irreversible expansions. These different contributions are calculated through the force and momentum balance for a differential element of the heat exchanger core, as described by (Shah; Sekulic, 2003). The contributions are shown hereafter.

i. Core channel pressure drop

Two different sources account for the core channel pressure drop,  $\Delta P_{23} = p_2 - p_3$ , (1) friction losses at the wall, and (2) momentum rate change due to fluid flow acceleration or deceleration, according to the temperature change. The core pressure drop is given by:

$$\Delta P_{23} = \frac{G^2}{2\rho_{in}} \left[ f \frac{4L}{D_h} \rho_{in} \left( \frac{1}{\rho} \right)_m + 2 \left( \frac{\rho_{in}}{\rho_{out}} - 1 \right) \right] \quad (4.14)$$

where  $f$  is the Fanning friction factor and  $\left( \frac{1}{\rho} \right)_m$  is the mean specific volume, evaluated as  $\left( \frac{1}{\rho} \right)_m = \frac{1}{2} \left( \frac{1}{\rho_i} - \frac{1}{\rho_o} \right)$  for a liquid with any flow arrangement or an ideal gas with  $C_r = 1$ , or as  $\left( \frac{1}{\rho} \right)_m = \frac{\tilde{R}}{p_{avg}} T_{lm}$ , for a perfect gas with  $C_r = 0$ , where  $\tilde{R}$  [ $J \cdot kg^{-1} \cdot K^{-1}$ ] is the gas constant. As described in (Shah; Sekulic, 2003), the core frictional pressure drop generally accounts for 90% or more of the pressure drop for gas flows in many compact heat exchangers.

ii. Entrance pressure drop

The core entrance pressure drop,  $\Delta P_{12} = p_1 - p_2$ , consists of two contributions: (1) the pressure drop due to the fluid flow area contraction, and (2) the pressure losses associated with the free expansion of the fluid due to the sudden contraction, as seen in Figure 18, generating a *vena contracta*. Its value is given by:

$$\Delta P_{12} = \frac{G^2}{2\rho_i} (1 - \sigma^2 + K_c) \quad (4.15)$$

where  $\sigma$  is the ratio of the free flow area of the channel and  $K_c$  is the contraction loss coefficient, evaluated from (Kays; London, 1998) diagram available in (Shah; Sekulic, 2003).

iii. Exit pressure rise

The core exit pressure rise,  $\Delta P_{34} = p_4 - p_3$ , is composed of two contributions: (1) the pressure rise due to the deceleration caused by the area increase and (2) the pressure loss associated with the free expansion, and it is given by:

$$\Delta P_{34} = \frac{G^2}{2\rho_o} (1 - \sigma^2 - K_e) \quad (4.16)$$

where  $K_e$  is the expansion loss coefficient, evaluated from (Kays; London, 1998) diagram available in (Shah; Sekulic, 2003).

Therefore, the total core pressure drop is given by the sum of the aforementioned contributions, as:

$$\Delta P_{total\ core} = \Delta P_{12} + \Delta P_{23} - \Delta P_{34}. \quad (4.17)$$

As aforementioned, other pressure drops may be accounted for by the heat exchanger measurement equipment, such as (a) pipe losses or (b) inlet/outlet headers. These portions are calculated following the methodology presented in (Shah; Sekulic, 2003), and their contributions are given below.

(a) Pipe losses

A pipe of constant cross-section offers the following frictional pressure drop:

$$\Delta P_{pipe} = \left( f \frac{4L}{D_h} \frac{\rho u_m^2}{2} \right)_{pipe} \quad (4.18)$$

where  $f$ ,  $L$  and  $D_h$  are evaluated according to the pipe characteristics, and  $\rho$  and  $u_m$  are the fluid's density and velocity, respectively, evaluated at the pipe section.

(b) Inlet/outlet headers

If an inlet header (divergent nozzle) is used for connecting the fluid supplying pipe to the heat exchanger core and an outlet header (convergent nozzle) is used for discharging the fluid from the core back to a pipe, their pressure drop contributions can be calculated using a methodology similar to the one used for the core's entrance and exit pressure drops. As afore discussed, these pressure drops are based on two contributions, (1) the pressure drop due to the fluid flow area change, and (2) the pressure losses associated with the free expansion of the fluid. Therefore, the inlet and outlet headers pressure drop contributions are calculated from Eqs (4.15) and (4.16), respectively, for the appropriate area ratio,  $\sigma$ , as seen in:

$$\Delta P_{nozzles} = \left[ \frac{G_{pipe}^2}{2\rho_i} (1 - \sigma_{pipe}^2 + K_{e,pipe}) + \frac{G_{pipe}^2}{2\rho_o} (1 - \sigma_{pipe}^2 + K_{c,pipe}) \right]. \quad (4.19)$$

Therefore, the second term at the right of Equation (4.13) is written as:

$$\Delta P_{others} = \Delta P_{pipe} + \Delta P_{nozzles} \quad (4.20)$$

Finally, for a given heat exchanger pressure drop measurement, with aid of Eqs (4.13) to (4.19), the Fanning friction factor,  $f$ , for the unknown heat exchanger geometry is given by:

$$f = \frac{D_h}{4L} \frac{1}{\rho_i} \left( \frac{1}{\rho_i} \right)_m \left[ \Delta P_{measured} \frac{2\rho_i}{G^2} - (1 - \sigma^2 + k_c) - 2 \left( \frac{\rho_i}{\rho_o} - 1 \right) + \frac{\rho_i}{\rho_o} (1 - \sigma^2 - k_e) \right] - \Delta P_{others} \frac{2\rho_i}{G^2}. \quad (4.21)$$

On the other hand, the Fanning frictional factor may be represented as a function of the Reynolds number (Ngo et al., 2007), as:

$$f_{mod} = NRe^n \quad (4.22)$$

in which the subscript *mod* refers to model. Following a similar procedure as presented in Section 4.4, the unknowns  $N$  and  $n$  are solved using a non-linear regression method to minimize the difference between the experimental and the theoretical (model) Fanning friction factor,  $S_2$ , using the expression:

$$S_2 = \sum (f - NRe^n)^2. \quad (4.23)$$

The first term of the summation is calculated from Eq. (4.21). The constants  $N$  and  $n$  are unique for a certain geometry and experimental data available.

#### 4.6 HEAT LOSS AND UNCERTAINTY ANALYSIS

Due to heat losses, especially from the heat exchanger surfaces, and to measurement errors, the net balance between the fluid streams is unlike to be perfect. This last issue can be addressed by performing a rigorous calibration process of all the sensors. Besides, the heat dissipation can be minimized by covering the heat exchanger core and its inlet and outlet branches with insulation materials. Therefore, the total loss and ratio of the heat to the ambient losses are given by:

$$Q_{loss} = Q_h - Q_c, \quad (4.24)$$

$$Q_{loss\ ratio} = \frac{Q_{loss}}{Q_{avg}}. \quad (4.25)$$

The combined uncertainty of the direct and indirect measured parameters, calculated from the systematic errors from the measurement equipment and the random fluctuations in time during measurements reading, is evaluated according to the method presented in (Holman, 2011). The geometric parameters and the fluid's properties were considered as well-known values, therefore with null uncertainties and the expanded uncertainties were obtained for a

confidence interval of 95%. The complete uncertainty analysis procedure is presented in APPENDIX B – Uncertainty analysis.

The experimental data obtained in the tests performed are treated following the data reduction method presented in this chapter. The results are discussed in the next section, analyzing the main thermal and hydraulic parameters obtained.

## 5 RESULTS AND DISCUSSION

In the current chapter, the data obtained in this work is analyzed and discussed. Firstly, the main geometric parameters of the DBHE channel are evaluated previously than the mathematical analysis of the experimental data. Then the evaluation of the water-water results, with the discussion of the main thermal parameters of the heat exchanger is presented. The heat transfer correlation for this layout configuration, i.e. fluids and inlet conditions, is proposed. The available experimental and numerical data from the literature are used for comparison with the heat transfer characteristics of the current channel geometry with others. The equipment pressure drop is also briefly discussed. In a second part of the chapter, the air-water experimental results are presented, following a similar outline of the water-water discussion. Data from similar DBHEs previously tested at *Labtucal*, with different channel geometries, is revisited to be compared with the present results. Through the analysis of the thermal performance of all these equipment, Nusselt number correlations are proposed for each channel geometry. Then, the pressure drop data is analyzed and friction factor correlations are proposed. In both analyses, literature data for other channel geometries are used to validate the current analysis and compare the results obtained. Finally, the heat transfer and friction factor characteristics of the DBHEs tested at *Labtucal* are compared in a single chart.

### 5.1 PROTOTYPE REAL DIMENSIONS

It is expected that the tested DBHE actual plate and channel dimensions to be different from the project ones, due to the plastic deformations of the plates during the diffusion bonding process and to the irregularities in the water jet cutting processes. Therefore, the actual dimensions of height and width of the channels were verified through an analysis of a photograph made with a scale positioned in the entrance section of the exchanger, as seen in APPENDIX C – DBHEs inlet ports photos. The other dimensions, i.e. zigzag angle and pitch length, are assumed to be identical to those of the project. Table 3 indicates the channels' main dimensions, which are used for the evaluation of the thermal and hydraulic parameters in continuation.

Table 3 – Channels' dimension of the 90° zigzag angle prototype.

Parameters	90° zigzag angle prototype
Channel width, $w_c$	2.984 mm
Channel height, $E_p$	2.864 mm
Zigzag angle, $\alpha$	90°
Zigzag pitch, $p$	13.51 mm

## 5.2 WATER-WATER ANALYSIS

The primary measurements obtained from the heat exchanger experiments were the fluids inlet and outlet temperatures, their mass flow rates and the pressure of the water. The complete set of experimental data obtained in this dissertation is shown in APPENDIX A – Experimental data.

### 5.2.1 Water-water thermal analysis

Initially, the uncertainties of the main parameters evaluated in this section are shown in Table 4. From Table 1, there is a total of 8 sets of experiments with 7 tests each, totalizing 56 tests. The uncertainties are given as percentages of the assessed quantities, grouped in a unique average and maximum relative uncertainties from the total number of tests. It is interesting to highlight the low values of uncertainties obtained in the analysis of thermal parameters, with maximum values below 6%. Only the pressure drop presents a higher uncertainty, with a maximum relative uncertainty of 20.67%. This can be explained by the fact that a single pressure transducer was used for the whole test range. Therefore, the equipment presented a large span range, resulting in higher uncertainties for low measurements made. The complete uncertainty analysis of the parameters evaluated in the present section is presented in detail in APPENDIX B – Uncertainty analysis.

Besides the uncertainty evaluation, the heat losses can influence the data and so a brief analysis is presented here. The experimental heat balance and heat loss are evaluated employing Equations (3.8), (3.9), (4.24) and (4.25), which results are shown in Figure 19. On the left side, it is shown the plot of the heat transfer obtained from the cold stream data (vertical axis) with the hot stream (horizontal axis). As most of the data are very close to the diagonal curve, one can conclude that the setup produced quite good data, with a deviation lower than 5% (Figure

19(a)). This discrepancy is caused by measurement errors and heat losses to the ambient. Therefore, the average heat load, evaluated with Equation (3.10) is used in the thermal analysis. The ratio between the heat loss and the average heat load is plotted against the average heat load in Figure 19(b). As one can see, the heat lost to the ambient represents less than 4.0% for all the experimental data, with a mean value of 3.31%. The total heat load for the different experimental conditions varied from approximately 22 kW to 63 kW.

Table 4 – Water-water experimental uncertainties.

Parameters	Average relative uncertainty, (%)	Maximum relative uncertainty, (%)
Inlet/outlet temperatures, $T$	$\pm 0.59$	$\pm 0.62$
Hot/cold mass flow rate, $\dot{m}$	$\pm 2.61$	$\pm 2.89$
Heat transfer rate, $Q_{avg}$	$\pm 2.68$	$\pm 3.63$
Overall heat transfer coefficient, $U$	$\pm 2.94$	$\pm 4.01$
Effectiveness, $\epsilon$	$\pm 1.70$	$\pm 2.77$
Number of transfer units, $NTU$	$\pm 3.94$	$\pm 4.72$
Hot/cold Reynolds number, $Re$	$\pm 2.82$	$\pm 5.85$
Nusselt number, $Nu$	$\pm 2.08$	$\pm 3.83$
Pressure drop	$\pm 10.54$	$\pm 20.67$

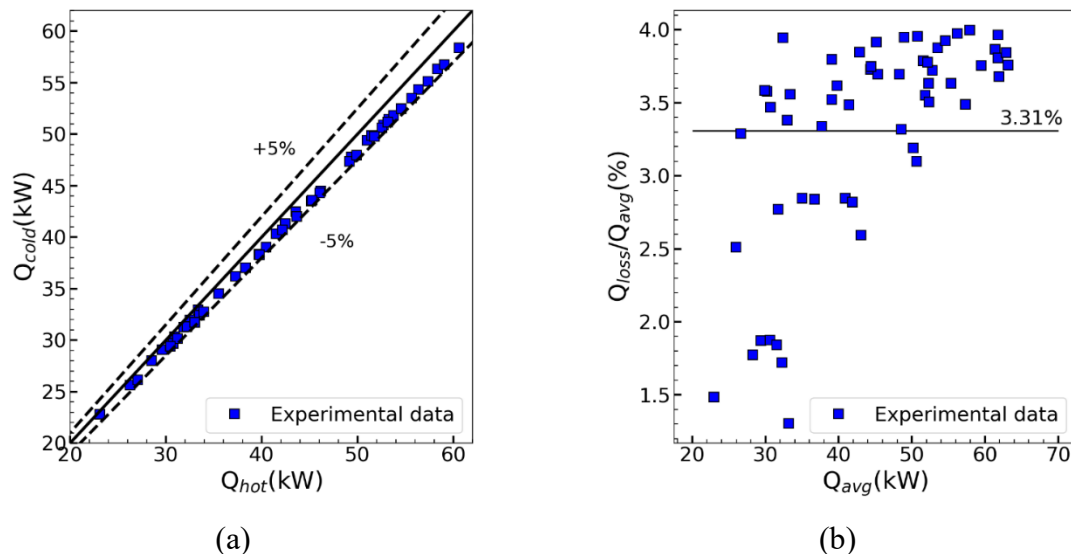


Figure 19 – Heat exchanger balance between the cold and hot streams (a) and heat loss ratio to the average heat load (b).

Figure 20 shows the experimental results for the total heat transfer rate (a) and the overall heat transfer coefficient (b), respectively, as a function of the hot stream Reynolds number, for the experimental data points of each set of experiments. To make the data analysis easier, dashed lines were plotted for sets of experiments number 1 and 8, which correspond to the lower and the upper cold fluid Reynolds number, of approximately 1312 and 6327, respectively. In both dashed line curves, it can be seen that, by increasing the hot stream Reynolds number, the overall heat transfer coefficient, and therefore the total heat transferred, also increases. For the tests with cold side Reynolds of approximately 1312, bottom dashed line, an increase of approximately 500% in the hot fluid Reynolds number rises by approximately 34% the overall heat transfer coefficient, and by 44% the total heat load, as indicated by the arrows. For the data set with a cold side Reynolds of approximately 6327, top dashed line, the increase of approximately 500% of the Reynolds number hot stream enhances by 48% and 89% the overall heat transfer coefficients and the total heat loads, respectively, as indicated by arrows in the figure. This means that these parameters are more sensitive to the high cold side Reynolds numbers.

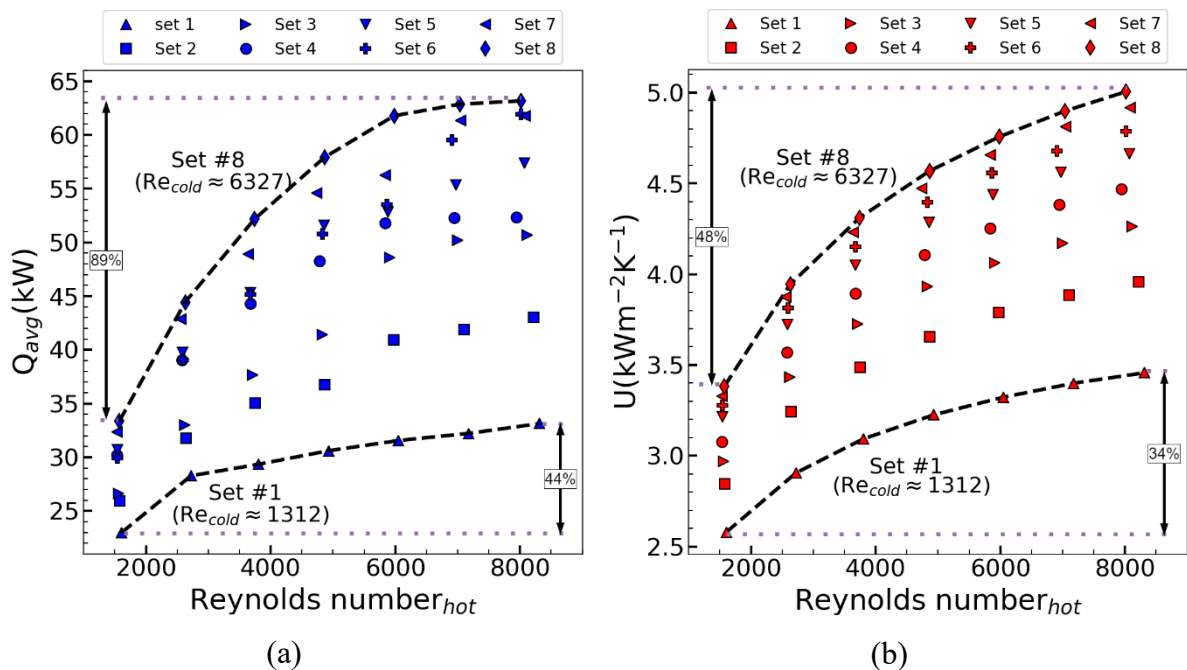


Figure 20 – Heat transfer rate (a) and overall heat transfer coefficient (b) vs. Reynolds number on the hot channel.

Figure 21 presents the experimental results for the effectiveness as a function of the NTU (a), and as a function of the hot channel Reynolds number (b). In Figure 21 (a), the theoretical effectiveness for a heat capacity ratio of  $C_r = 0.15$  and  $C_r = 1$  for a counter flow heat exchanger is also plotted (Bergman et al., 2011). Since the mass flow rate was adjusted separately for each stream, as presented in Table 1, the heat exchanger was tested under different heat capacity ratio ( $C_r$ ) conditions, from 0.18 to close to 1. The effectiveness varied from approximately 0.3 to 0.75, for NTU values from 0.5 to 1.5. Also, dashed lines for the set of experiments as described in Table 1 were plotted in Figure 21 (b) to enable the analysis of data. For set number 1 with a constant mass flow rate at the cold side, the hot mass flow increases by approximately 500% resulted in a continuous increase of the heat exchanger effectiveness. For sets number 2 to 6, it is observed a monotonical decrease of the effectiveness for the increase of the hot channel Reynolds number, until a minimum is reached and then the trend is inverted. Finally, for sets 7 and 8, it is observed a monotonic decrease of the effectiveness with the increase in the hot channel Reynolds numbers. The inversion points occur at different hot stream Reynolds values for every set, specifically when the heat capacity ratio is close to one. This behavior is expected because the maximum and the minimum heat exchanger effectiveness occur for  $C_r = 0$  and  $C_r = 1$ , respectively (Bergman et al., 2011). Therefore, by increasing the hot stream Reynolds number, the heat capacity ratio decreases, and the effectiveness increases, as seen in set number 1 as well as sets 2 to 6 after the inversion point. On the other hand, when the heat capacity ratio increases with the increase on the hot Reynolds number, the effectiveness decreases, as seen in sets 2 to 6 before the inversion point, and sets 7 to 8.

As discussed in Section 4.4, a Nusselt number correlation is proposed through the calculation of the fitting parameters from Equation (4.6). Using the Levenberg-Marquardt non-linear regression method (Moré, 1978) as implemented in (Virtanen et al., 2020), Equation (4.7) is minimized. The fitting constants  $C$ ,  $a$  and  $b$  are proposed based on the utilization of all sets of experimental data, not restricted to equal hot- and cold-side Reynolds numbers. The calculated overall heat transfer coefficient is compared to the experimental data using Equations (4.1) and (4.6), and the result is presented in Figure 22.

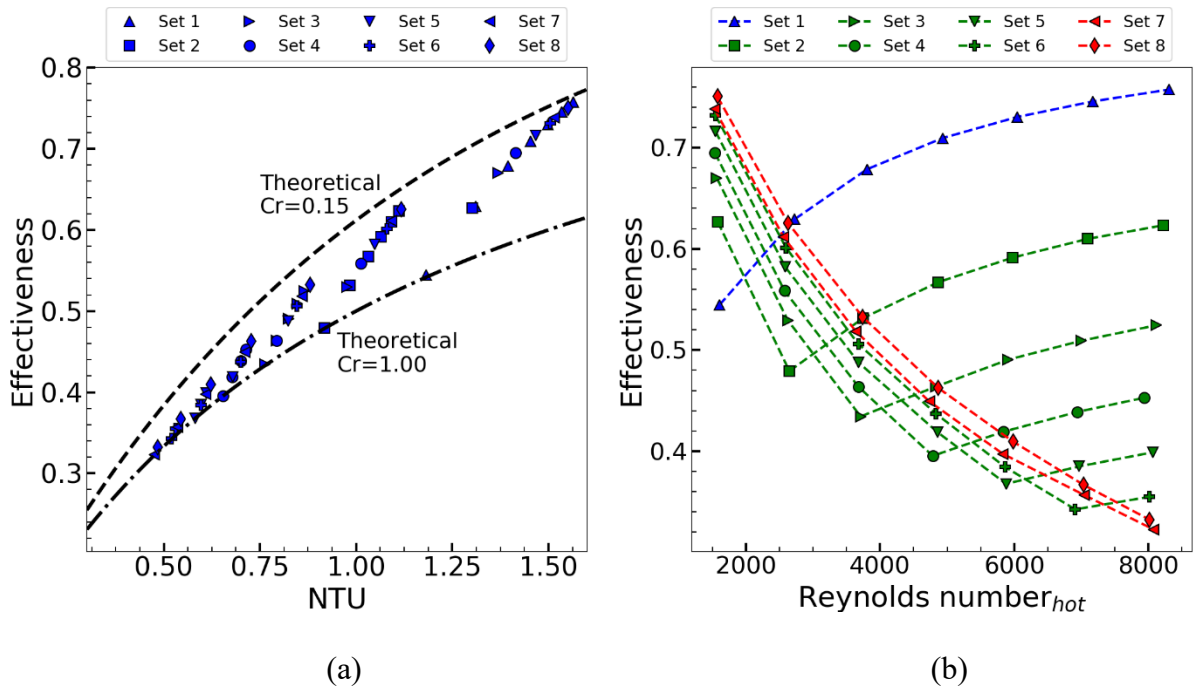


Figure 21 – Effectiveness vs. NTU, (a), and vs. the Reynolds number of the hot channel, (b).

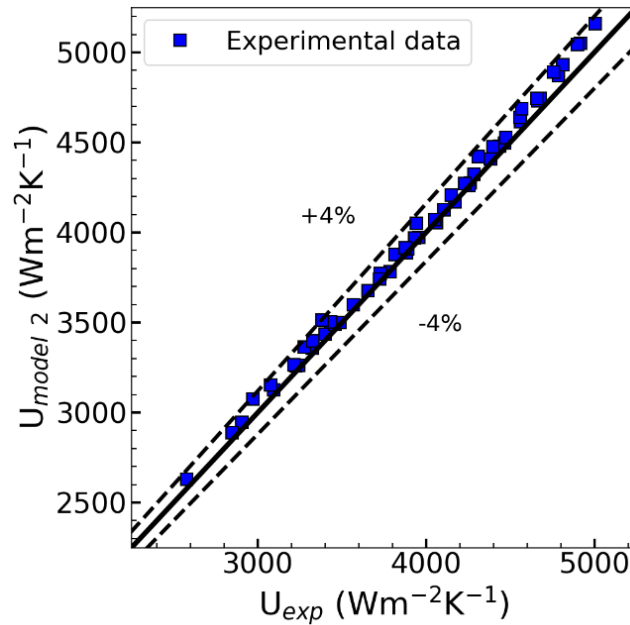


Figure 22 – Overall heat transfer coefficient comparison between the fitted model vs. experimental value.

As can be seen in Figure 22, the experimental and the model values show a good agreement for all sets of experimental data. The differences are within 4%. The fitted Nusselt correlation, as in Eq. (4.4), is:

$$Nu = 0.5656 Re^{0.5424} Pr^{0.01140}, 1299 \leq Re \leq 8313. \quad (5.1)$$

As seen in Eq. (5.1), the calculated constants  $C = 0.5656$ ,  $a = 0.5424$ , and  $b = 0.01140$ , specific for the present  $90^\circ$  zigzag channel geometry, operating with water, differ from previous correlations from the literature, e.g. Dittus-Boelter correlation for turbulent flow in a smooth duct, as described in (Shah; Sekulic, 2003), (Ngo et al., 2007) for a  $76^\circ$  zigzag channel PCHE operating with CO<sub>2</sub>, or (Saeed et al., 2020) for a  $100^\circ$  zigzag channel PCHE operating with water. This difference can be attributed to the fact that the channel geometries and the fluid properties have a great influence on the heat transfer rates.

In order to evaluate the heat transfer enhancement provided by a  $90^\circ$  zigzag angle channel, the experimental results obtained in this study are compared with theoretical predictions based on a literature model developed for a straight channel DBHE. The theoretical model, developed by (Sarmiento et al., 2020b), can accurately predict the thermal behavior of a straight channel DBHE with a semi-circular or square cross-section (Sarmiento; Milanez; Mantelli, 2020). The external dimensions of the present DBHE tested, as well as the experimental flow conditions, were set as input parameters in this model.

Figure 23 shows a comparison of the Nusselt number for the experimental DBHE  $90^\circ$  zigzag angle tested and a theoretical straight channel DBHE, operating in similar flow and temperature conditions. Figure 23 also compares the Nusselt number correlation proposed in this paper, Eq. (5.1), with the numerical results from (Li; Yu; Yu, 2020), for a  $90^\circ$  zigzag channel PCHE with semi-circular cross-section, operating with S-CO<sub>2</sub>. As can be seen from Figure 23, all Nusselt number curves present an increasing trend with the rising Reynolds numbers. The Nusselt number predictions using Li; Yu and Yu (2020) numerical results, developed for a  $90^\circ$  semi-circular zigzag channel, represent approximately 70% of the predicted values using the correlation proposed in the current work, for a  $90^\circ$  zigzag channel with a square cross-section. The different working fluids employed to get the data for these correlations can be responsible for this discrepancy.

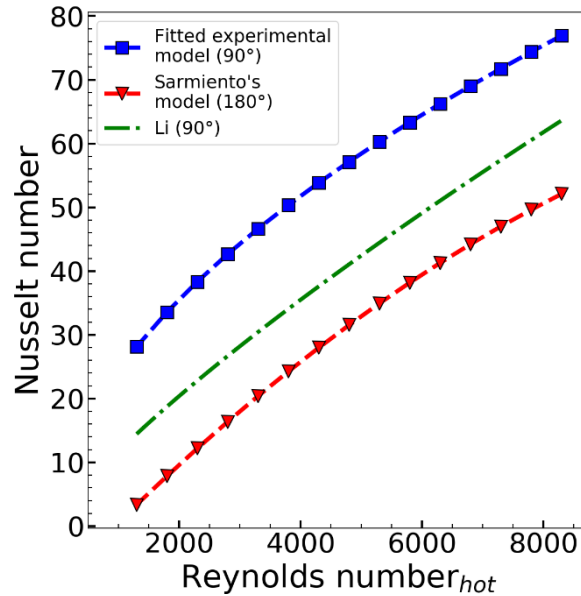


Figure 23 – Nusselt number comparison between the experimental data of the 90° zigzag channel DBHE, a theoretical straight channel DBHE, and a 90° zigzag channel from the literature.

Figure 23 also shows that the correlation proposed by Eq. (5.1) showed an average enhancement of the Nusselt numbers of approximately 2.2 times compared to a straight channel DBHE (180°), with similar input flow conditions and the same external geometric parameters. For low Reynolds numbers, an enhancement up to 3.5 is achieved. Therefore, this analysis demonstrates that the 90° DBHE has a better performance when compared to a similar straight channel heat exchanger. Moreover, the only 90° zigzag channel PCHE data from the literature, obtained for S-CO<sub>2</sub> working fluid, failed to match the results currently obtained with water. Therefore, Eq. (5.1) is proposed as a newly fitted correlation for DBHE's operating with water.

As aforementioned, there are only a few studies with DBHEs operating with water, and most of them regard Reynolds numbers below 850. Recently, Saeed et al. (2020) published a numerical analysis of the thermal and hydraulic characteristics of a zigzag channel of a PCHE operating under precooler conditions of an S-CO<sub>2</sub> Brayton cycle. From their investigation, a Nusselt number correlation for the water side, for larger values of Reynolds numbers was proposed for a semi-circular cross-section channel, with a zigzag angle of  $\alpha=100^\circ$ . Besides, Cheng et al. (2020) experimentally investigated a semi-circular zigzag PCHE, tested in an S-CO<sub>2</sub>-water configuration. Although large attention was given to the water side influence on the thermal performance of the heat exchanger, no heat transfer correlation was developed. The

experimental data from (Cheng et al., 2020) is revisited - the main geometric specifications and test conditions are resumed in Table 5. While the inlet flow conditions are used in (Cheng et al., 2020) to evaluate the thermophysical properties, in the present study they are evaluated at the average fluid temperature, resulting in a different Reynolds number range than that reported in (Cheng et al., 2020).

Table 5 - Cheng et al. (2020) PCHE geometry and test conditions. Adapted from (Cheng et al., 2020)

Parameters	Hot side (S-CO <sub>2</sub> )	Cold side (water)
Diameter of the semi-circle channel, mm	1.5	1.6
Angle of zigzag $\alpha$ , °	115	150
Pitch length P, mm	9	24.6
Dimensions of plates, mm	486x101x2	486x101x2
Inlet pressure, MPa	8.07-8.60	0.163-0.204
Inlet temperature, K	363.4-383.4	293.0-299.7

By recalling the data reduction method presented in Section (4.1), the Nusselt number for the water side in the (Cheng et al., 2020) experiment can be calculated, if the CO<sub>2</sub> heat transfer coefficient is known a priori (Song, 2007; Van Meter, 2008). Kim et al. (2016) correlations for zigzag channels PCHE operating at the S-CO<sub>2</sub> Brayton cycle were developed for a zigzag channel equal to (Cheng et al., 2020) in terms of the angle, the pitch length, and the cross-section shape, but for a diameter approximately 25% larger than in (Cheng et al., 2020). Furthermore, these correlations were used by (Zhou et al., 2020) in their experimental investigation, in a similar configuration to (Cheng et al., 2020). Therefore, in the present work, the heat transfer coefficient proposed in (Kim et al., 2016), for the CO<sub>2</sub>, is used as the hot side coefficient in Eq. (4.3), to evaluate the cold side heat transfer coefficient for the (Cheng et al., 2020) testing conditions and data. Analysis by Song (2007) showed that the thermal resistance due to the conduction on the wall separating the hot and cold channels is negligible for a similar PCHE. Therefore, it was not considered in the present analysis.

Figure 24 shows the proposed Nusselt correlation for the 90° zigzag channel, which is compared with the experimental data from (Cheng et al., 2020), for a 150° zigzag channel, together with results from the correlation of (Saeed et al., 2020) for a 100° zigzag angle

geometry, and the correlations from (Gnielinski, 2013) and (Sarmiento et al., 2020b) for straight ducts, all operating with water.

The obtained results are separated in the laminar-to-transition regimes (the experimental data from (Cheng et al., 2020) is only available for this regime), and in the turbulent regime. To make data analysis easier, Table 6 summarizes the Nusselt numbers ratios of the current experimental model of the 90° zigzag channel and the values from (Saeed et al., 2020), (Gnielinski, 2013), and (Sarmiento et al., 2020b) for straight channels (180°), for Reynolds number up to 4000.

From Figure 24(a), one can see that, for Reynolds number values up to 4000, the zigzag channel that presents the larger Nusselt numbers has a 90° angle, followed by the 100° and the 150°. From Table 6, all the zigzag channels evaluated provided a higher heat transfer rate in the laminar regime than the in transition. The 90° zigzag channel presents Nusselt numbers 4.1 times larger, on average, than the straight channel evaluated by Gnielinski's model, for  $1299 < Re < 2300$ , which is the largest ratio among the geometries and models evaluated. In the transition,  $2300 < Re < 4000$ , this heat transfer enhancement drops to 2.6 times. The Nusselt number for the 150° zigzag is only available for Reynolds numbers from 1573 to 2518, showing a small increase, of 6%, when compared to Gnielinski's correlation for a straight channel, and a decrease of 23% when compared to Sarmiento's correlation for a straight channel. While it is clear that the 90° and 100° zigzag channel geometries represent a considerable enhancement on the Nusselt number values compared to a straight channel, the 150° zigzag did not. This may occur because this channel is almost straight (large zigzag angle and pitch length). In Figure 24 (b), for Reynolds number equal to 4000, the 90° zigzag increases the Nusselt number in 1.8 times, compared with Gnielinski's and Sarmiento's correlations for straight channels, while, for the 100° channel, the enhancement is of 1.6 times. The 90° and the 100° curves intersect each other at Reynolds number around 5837, where they present an increase of 1.5 times of the Nusselt number to the straight channel. Besides, at Reynolds around 8313, the 90° and 100° enhancement in the Nusselt number is approximately 1.3 and 1.4 times larger than the straight channel, respectively.

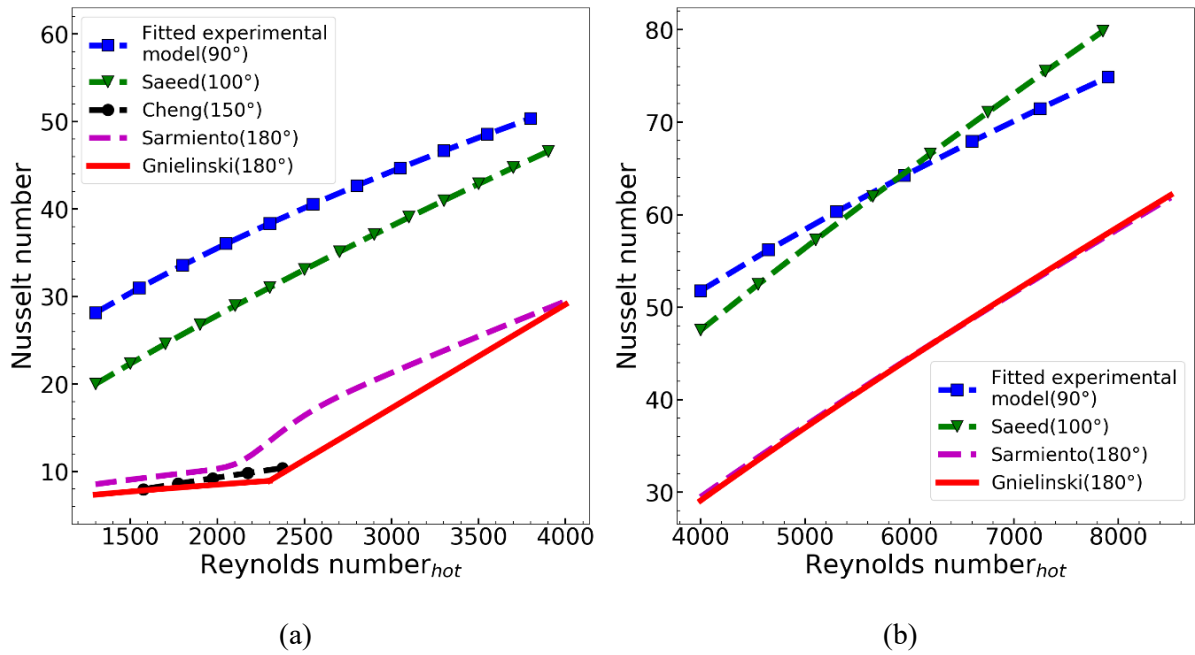


Figure 24 – Proposed Nusselt number correlation for 90° zigzag channel compared with models. (a) comparison with 150° and 100° zigzag channels and straight channel correlations for laminar and transition regimes. (b) comparison with 100° zigzag and straight channel correlations for turbulent flow regime.

Table 6 – Comparisons between the Nusselt number of the fitted experimental (90°) zigzag channel and (Saeed et al., 2020) zigzag model, with (Gnielinski, 2013) and (Sarmiento et al., 2020b) correlations for straight channels (180°).

	Reynolds range	
	$Re \leq 2300$	$2300 < Re \leq 4000$
Nusselt number ratio		
$\frac{\text{Fitted experimental model}(90^\circ)}{\text{Gnielinski}(180^\circ)}$	4.1	2.6
$\frac{\text{Fitted experimental model}(90^\circ)}{\text{Sarmiento}(180^\circ)}$	3.0	2.3
$\frac{\text{Saeed}(100^\circ)}{\text{Gnielinski}(180^\circ)}$	3.1	2.2
$\frac{\text{Saeed}(100^\circ)}{\text{Sarmiento}(180^\circ)}$	2.3	2.0

Manufacture requirements of different inlet and outlet ports for the different fluid streams lead to cross-flow at the entrance and the exit of the heat exchanger, as seen in Figure 10. This cross-flow region may be the cause of the intersection between the curves for 90° and 100° zigzag in Figure 24 (b). In the investigation of (Saeed et al., 2020), the 100° zigzag channels are counter-flow only. Since it is a numerical study, there are no manufacture restrictions of different inlet and outlet ports and, therefore, there is no impact on the total heat transfer. Other aspects may be the source of this discrepancy and further investigations are needed.

As it can be noticed, the Nusselt number calculated from Sarmiento's correlation presented in Figure 24 and Figure 23 differ. Sarmiento's Nusselt number correlation for a straight channel, seen in Figure 24, is slightly larger than the results obtained in the theoretical Nusselt number value for a similar DBHE with straight channels, as presented in Section 5.2. This is explained because the theoretical model takes into account the variations of the fluid's Prandtl number with temperature, while, in the straight channel Nusselt number correlation, the input parameter is the average Prandtl number. Furthermore, the influence of the cross-flow current aforementioned is considered in the theoretical straight model and so a decrease in the total heat transferred is predicted in the analysis of Section 5.2.

### 5.2.2 Water-water hydraulic analysis

Although the discontinuities on the fluid path of a zigzag channel provide a better fluid mixing, which could increase the heat transfer rate, they are also responsible for higher hydraulic losses, resulting in higher pressure loss in the channels. The pressure drop along the heat exchanger core was evaluated through the differential pressure transducer placed in the hot stream line. Figure 25 shows the experimental results obtained for the hot stream mass flow rate from  $0.9 \text{ kg}\cdot\text{s}^{-1}$  to  $1.9 \text{ kg}\cdot\text{s}^{-1}$ , for the cold mas flow rate of  $0.4 \text{ kg}\cdot\text{s}^{-1}$ . The result is compared with the correlation developed by Saeed (Saeed et al., 2020) for a 100° zigzag angle channel and the correlation of a circular straight channel by Bhatti and Shah, as described in (Shah; Sekulic, 2003). As it can be noticed from Figure 25, the zigzag channels offer a great increase in the heat exchanger's pressure drop, compared to a straight channel. For Reynolds number values near 3800, the pressure drops of 90° and 100° zigzag angle channels are close to each other and around 30 kPa, about 15 times larger, compared to a straight channel. For Reynolds number near 8300, the 90° zigzag angle pressure drop is 138 kPa, which means an increase of 1.39 times when compared to the 100° angle and 16 times compared to a straight

channel. The evaluation of the friction characteristics of the present heat exchanger will be developed on the next section.

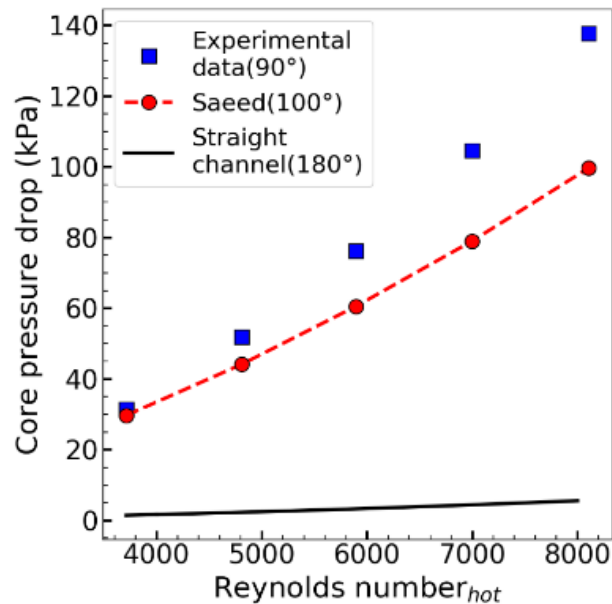


Figure 25 – Experimental 90° zigzag angle channel pressure drop comparison with 100° and 180° channels.

### 5.3 AIR-WATER ANALYSIS

The complete experimental data obtained during the air-water tests is presented in APPENDIX A –Experimental data.

The current experimental results are compared with the thermal and hydraulic results of similar DBHEs prototypes produced and tested at *Labtucal*. The experimental data from DBHEs, with the zigzag-angle channel of  $\alpha = 144^\circ$ , (Batista, 2017), and straight channels ( $\alpha = 180^\circ$ , (Carqueja, 2017), are revisited. As described in (Batista, 2017) and (Carqueja, 2017), these DBHEs followed a very similar manufacturing procedure, presenting heat exchanger cores with similar geometrical dimensions, including the metal sheet plate geometries, with the major difference being the zigzag angle,  $\alpha$ . Furthermore, as described in Section 4.2, (Batista, 2017) and (Carqueja, 2017) tests were performed at the same test facility of the current work, however, in a different configuration, in which hot-water and cold-air were used as the working

fluids, instead of the current hot-air and cold-water layouts. Although the fluid configuration is reversed, the thermal and hydraulic performance parameters of these DBHEs are of the same order of magnitude and so they can be compared. Thus, in the continuation of this work, these equipment will be referred to their zigzag angle, as DBHE 090, for the current air-water experiments, and DBHE 144 and DBHE 180, for (Batista, 2017) and (Carqueja, 2017) revisited experimental data, respectively.

An analysis of the channels' dimensions of DBHE 144 was elaborated similarly to the one performed for DBHE 90, as described in the previous section. The DBHE 144 inlet port photo is presented in APPENDIX C – DBHEs inlet ports photos. The channels' dimensions of DBHE 180 are considered equal to DBHE 144, since these prototypes were manufactured following a similar procedure. These parameters are shown in Table 7. Other main geometric dimensions of DBHEs 144 and 180 are also presented in Table 7.

Table 7 – DBHEs 144 and 180 main dimensions.

Parameters	DBHE 144	DBHE 180
Channel width, $w_c$	2.980 mm	2.980 mm
Channel height, $E_p$	2.801 mm	2.801 mm
Zigzag angle, $\alpha$	144°	180°
Zigzag pitch, $p$	13.51	N/A
Plate length, $L$	330 mm	330 mm
Number of hot/cold plates	9/9	9/9
Number of channels per plate	19	19

### 5.3.1 Air-water thermal analysis

In a two-fluid heat exchanger, the fluid with the smallest heat capacity is subject to the greatest temperature variation. In the same manner, the fluid with the highest heat capacity is subject to the smallest temperature variation, as it can be easily verified through Eqs. (3.8) and (3.9). The special case of a changing phase fluid can be seen as one fluid the heat capacity tending to infinity while its temperature variation tends to zero. In this case, the heat capacity ratio also tends to zero. Although the present experiment is not tested in a phase change situation, the experimental conditions are such that  $C_{air} \ll C_{water}$ , approaching this special case. Indeed, for the current fluid mass flows and specific heat capacities, the heat capacity ratio is near to zero for all the experimental data,  $C_r = C_{air}/C_{water} \approx 0$ . As a result, the temperature

increase in the cold fluid side, water, is as small as the sensor error, leading to uncertainties of up to 100% in the reading measurement. Thus, the heat balance evaluated by Equations (3.8) and (3.9), as seen in Figure 26(a), presents discrepancies of more than 50%, one order of magnitude larger than in the water-water layout. To mitigate this problem, the following thermal analysis is performed assuming the heat transfer calculated from the hot side, from Eq. (2.8), as the actual heat transferred by the equipment, instead of the heat load average of the streams.

At the same time as the cold fluid water presented a very small temperature increase, the hot fluid stream, air, experienced a major temperature drop. As seen in Figure 26(b), in most of the experimental data, the hot outlet temperature reached values very close to the cold inlet temperature. The limiting case, for a counter-flow arrangement, is the hot outlet temperature to be equal to the cold inlet temperature. However, the temperature sensors used were unable to measure the fluid's temperature with the necessary accuracy for the current experiment, leading to cases in which the hot outlet temperature was incorrectly read below the cold inlet temperature. Understanding that these were reading errors, such cases were modified with a temperature correction parameter  $CT$ , calculated as showed in:

$$T_{h,out} = T_{c,in} + CT, \quad (5.2)$$

in which the correction parameter is a fixed value, calculated as the mean temperature difference between the hot outlet temperature and cold inlet temperature of the remaining cases,  $CT = \text{mean}(T_{h,out} - T_{c,in})$ . The modified data following this procedure corresponded to 22% of the total experimental points, and they are highlighted in red in Figure 26. Figure 26 (b) also shows how the inlet cold temperature varied for the different tests, from approximately 18.6°C to 24.9°C. As described in Section 4, this occurs because the water-cooling tower is outside the laboratory building, subject to climatic conditions.

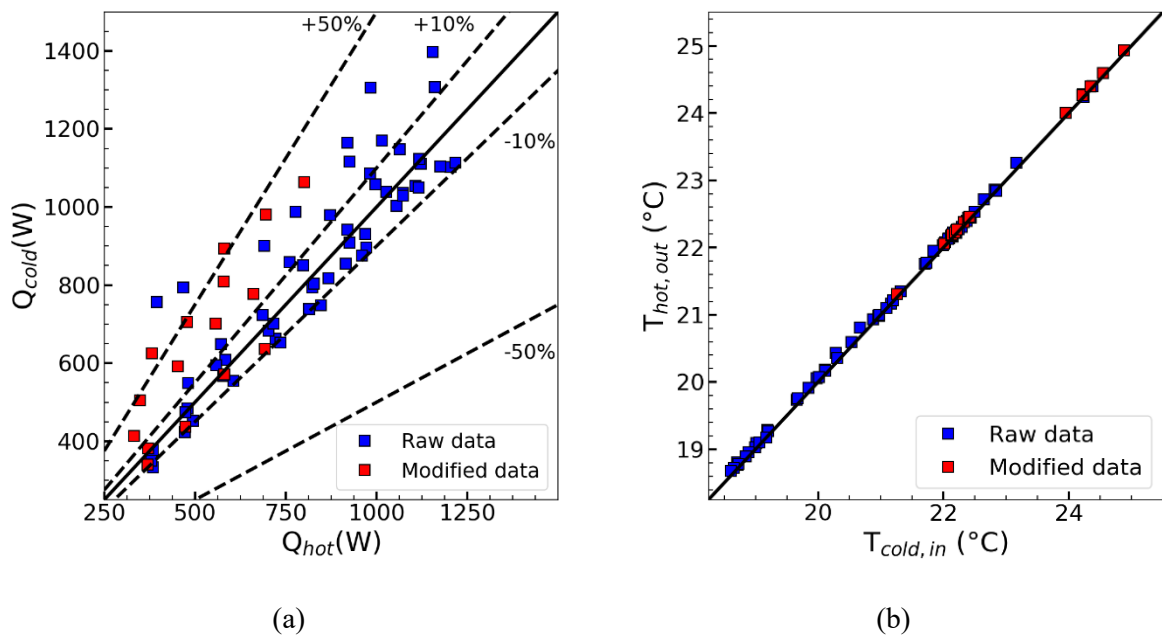


Figure 26 – Heat exchanger balance between the cold and hot streams (a) and outlet hot temperature vs. cold inlet temperature. Modified data following correction parameter from Eq. (5.2) in red and unmodified data in blue.

Figure 27 shows the experimental heat transfer rate plotted against the hot stream Reynolds number (a), for the different sets of experiments, and the cold stream Reynolds number (b), by grouping the curves by their similar air Reynolds number. As seen in (a), the heat transfer monotonically increases with the rise in the hot side Reynolds number, similarly for all Sets of experiments. As an example, for Set number 1, an increase of approximately three times in the hot fluid Reynolds number rises by approximately 300% the overall heat transfer coefficient, as indicated by the arrow on the figures. On the other hand, when the heat transfer rate is plotted against the cold stream Reynolds number by grouping similar air mass flow rates, (b), one can see that the curves tend to remain constant. Figure 27 (b) shows that the minimum water flow is capable of absorbing all the heat rejected from the hot stream. Therefore, in the point of view of the thermal analysis, increasing the water mass flow rate was not necessary. The heat transferred fluctuations seen in Figure 27 (b) for a determined air Reynolds number is caused by variations in the water inlet temperature, since the water-cooling tower is positioned at the outside of the laboratory, causing the inlet cold temperature in the heat exchanger to vary, as previously discussed.

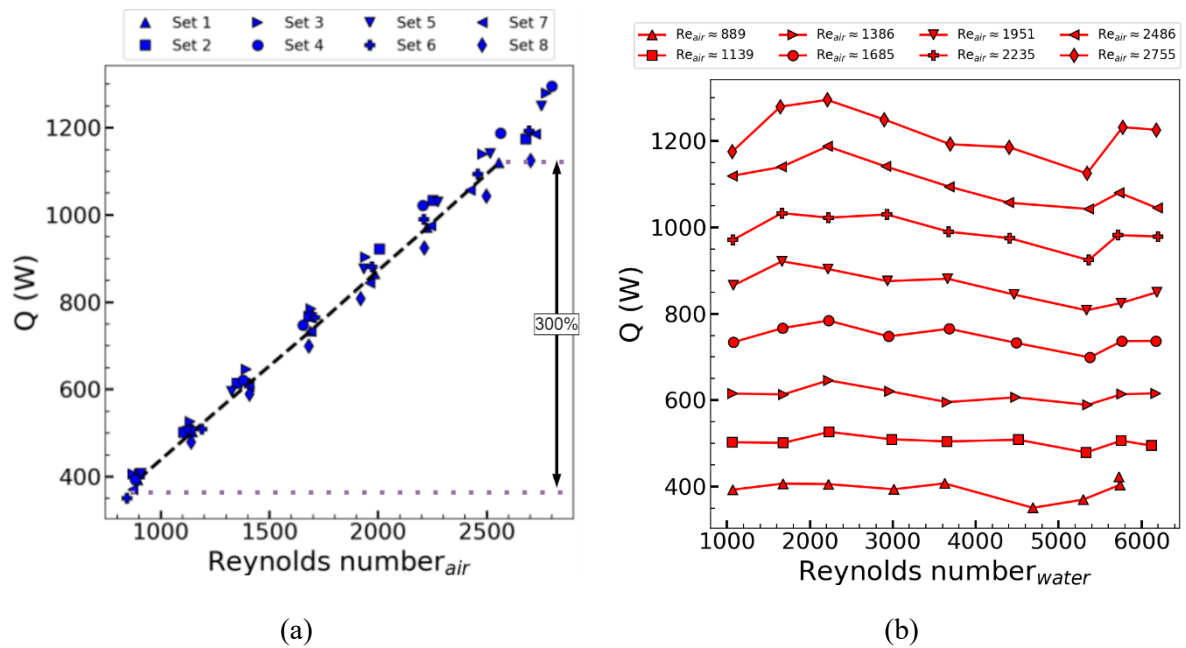


Figure 27 – Heat transfer rate vs. (a) air Reynolds number, and (b) water Reynolds number.

Figure 28(a) shows a schematic of the fluid arrangement tested in the DBHE 90 prototype, specifying its inlet and outlet ports, as well as the position of thermocouples that were fixed over the prototype surface. Figure 28(b) shows the readings of these thermocouples for the minimum water mass flow rate test condition, set number 1, and maximum air mass flow rate. The first fluid layer above the prototype surface is a hot stream sheet. The thermocouples reading in Figure 28(b) show that the external surface of the prototype reaches a terminal temperature approximately half its length. Although the fluids stream exchange heat along the whole flow length, it can be assumed that the majority of heat exchange between the fluids occurs in the first half of the prototype. In its final half, the thermocouples are not precise enough to measure the temperature decrease. This occurs in the case in which the minimum water mass flow rate and maximum air mass flow rate are used. Therefore the same occurs for all remaining tests, in which higher water mass flow rates and lower air mass flow rates are used.

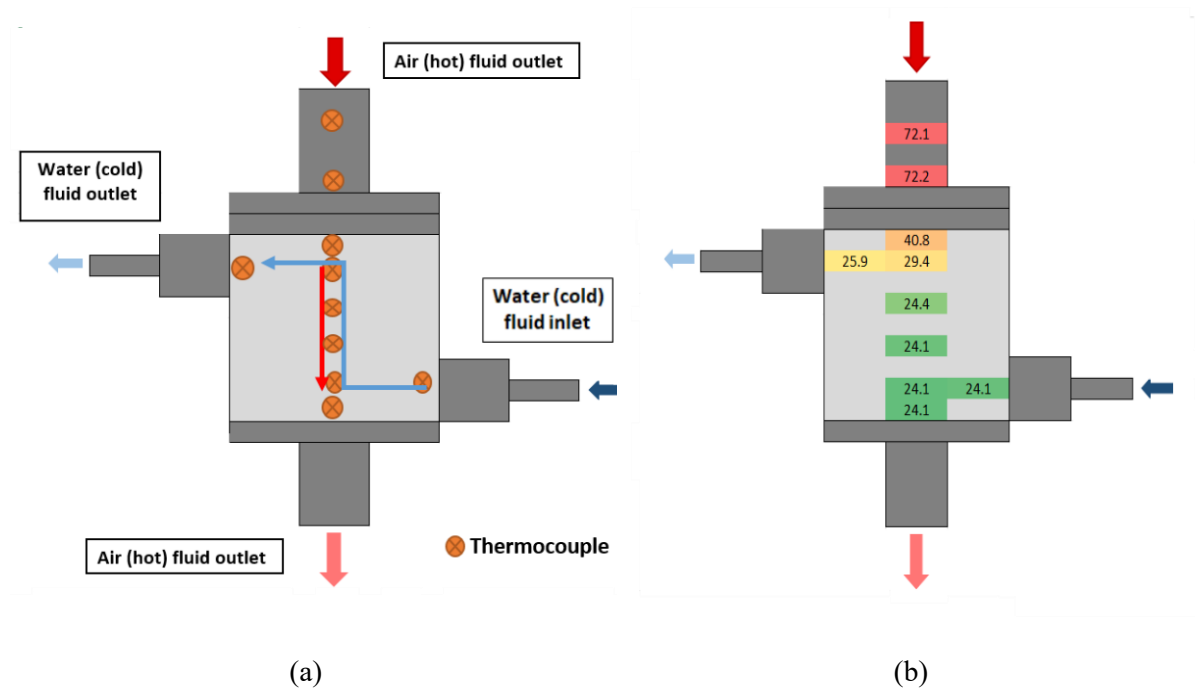


Figure 28 – DBHE 90 representation. (a) Fluids arrangement and thermocouples positioning. (b) Thermocouples reading on the prototype surface.

These results show that, for the air-water testing conditions, i.e. the fluids used and their mass flow and temperature conditions, the prototype is over-dimensioned to be tested in the current facility, jeopardizing the thermal analysis. From Figure 28(b), it can be observed that at least half of the prototype length is in excess. Moreover, the hot and cold temperature differences between the fluids inlet and outlet port are so close they cannot be precisely measured with the sensors used. As a result, the overall heat transfer coefficient,  $U$ , is expected to be much smaller than in a proper operating condition, and its associated uncertainty is expected to be very high. The NTU and the Nusselt number, parameters that depend on the overall heat transfer coefficient measurement, will also have their accuracy compromised.

To circumvent this issue, from the complete air-water experimental data disposed of in APPENDIX A –Experimental data, only the tests in which the overall heat transfer coefficient relative uncertainty was below 100% were used in the continuation of the thermal analysis. Following this criterion 15 tests out of the total 72 were discarded. Although the remaining 57 tests are maintained, the thermal performance of DBHE 90 under the air-water experiments should not be extended to other operating conditions and are presented solely as a comparison with the results from DBHE 144 and 180.

The uncertainty of the parameters evaluated in the present section was calculated according to the analysis presented in APPENDIX B – Uncertainty analysis, and the results for the current prototype tested, DBHE 90, are shown in Table 8. The uncertainty of the revisited data from DBHEs 144 and 180 are equally calculated, and their results are shown in Table 9 and Table 10, respectively.

Table 8 – DBHE 90 air-water experimental uncertainties.

Parameters	Average relative uncertainty, (%)	Maximum relative uncertainty, (%)
Inlet/outlet temperatures, $T$	$\pm 0.15$	$\pm 0.15$
Hot/cold mass flow rate, $\dot{m}$	$\pm 2$	$\pm 2$
Heat transfer rate, $Q_{avg}$	$\pm 4.28$	$\pm 4.29$
Overall heat transfer coefficient, $U$	$\pm 60.6$	$\pm 91.0$
Effectiveness, $\varepsilon$	$\pm 0.36$	$\pm 0.40$
Number of transfer units, $NTU$	$\pm 47.6$	$\pm 78.6$
Hot/cold Reynolds number, $Re$	$\pm 2$	$\pm 2$
Nusselt number, $Nu$	$\pm 50.5$	$\pm 83.6$
Pressure drop	$\pm 10.1$	$\pm 28.7$
Fanning friction factor, $f$	$\pm 11.7$	$\pm 29.1$
Colburn factor, $j$	$\pm 50.7$	$\pm 83.7$

Table 9 – DBHE 144 air-water experimental uncertainties.

Parameters	Average relative uncertainty, (%)	Maximum relative uncertainty, (%)
Inlet/outlet temperatures, $T$	$\pm 0.23$	$\pm 0.28$
Hot/cold mass flow rate, $\dot{m}$	$\pm 1.94$	$\pm 2.0$
Heat transfer rate, $Q_{avg}$	$\pm 2.10$	$\pm 2.47$
Overall heat transfer coefficient, $U$	$\pm 11.2$	$\pm 14.5$
Effectiveness, $\varepsilon$	$\pm 0.92$	$\pm 1.53$
Number of transfer units, $NTU$	$\pm 11.6$	$\pm 15.0$
Hot/cold Reynolds number, $Re$	$\pm 1.9$	$\pm 2.0$
Nusselt number, $Nu$	$\pm 11.2$	$\pm 14.5$
Pressure drop	$\pm 8.97$	$\pm 21.0$
Fanning friction factor, $f$	$\pm 9.32$	$\pm 21.1$
Colburn factor, $j$	$\pm 13.9$	$\pm 18.8$

Table 10 – DBHE 180 air-water experimental uncertainties.

Parameters	Average relative uncertainty, (%)	Maximum relative uncertainty, (%)
Inlet/outlet temperatures, $T$	$\pm 0.23$	$\pm 0.29$
Hot/cold mass flow rate, $\dot{m}$	$\pm 1.98$	$\pm 2.08$
Heat transfer rate, $Q_{avg}$	$\pm 2.14$	$\pm 2.46$
Overall heat transfer coefficient, $U$	$\pm 3.01$	$\pm 3.83$
Effectiveness, $\varepsilon$	$\pm 0.96$	$\pm 1.56$
Number of transfer units, $NTU$	$\pm 3.02$	$\pm 3.81$
Hot/cold Reynolds number, $Re$	$\pm 1.98$	$\pm 2.07$
Nusselt number, $Nu$	$\pm 3.00$	$\pm 3.84$
Pressure drop	$\pm 14.8$	$\pm 42.5$
Fanning friction factor, $f$	$\pm 15.0$	$\pm 42.56$
Colburn factor, $j$	$\pm 8.5$	$\pm 10.6$

As discussed, in the current fluid layout and testing conditions, the heat exchanger operates with no noticeable temperature change in the water stream. For the thermal resistance analysis, this fluid's convective thermal resistance is negligible when compared to the remaining thermal resistance of the air stream, as discussed in the second case of Section 4.4, named *model 2*. Therefore, the fitting parameters of Eq. (4.9) are calculated using the Levenberg-Marquardt non-linear regression method (Moré, 1978) as implemented in (Virtanen et al., 2020), minimizing Eq. (4.10). Since the Prandtl number does not vary significantly during the different experiments, its contribution is incorporated into the constant  $\mathbb{C}$ . The fitting constants  $\mathbb{C}$  and  $a$  and for the current case are proposed based on the utilization of all sets of experimental data.

The theoretical overall heat transfer coefficient from Eq. (4.9) is compared with its experimental value, Eq. (4.1), which is showed in Figure 29. The experimental and theoretical values difference is within 20%, as seen in Figure 29. The fitted Nusselt number correlation for the current fluid, air, at the tested conditions is given below:

$$Nu = 0.004948 \cdot Re^{1.0541}, 988 \leq Re \leq 3175. \quad (5.3)$$

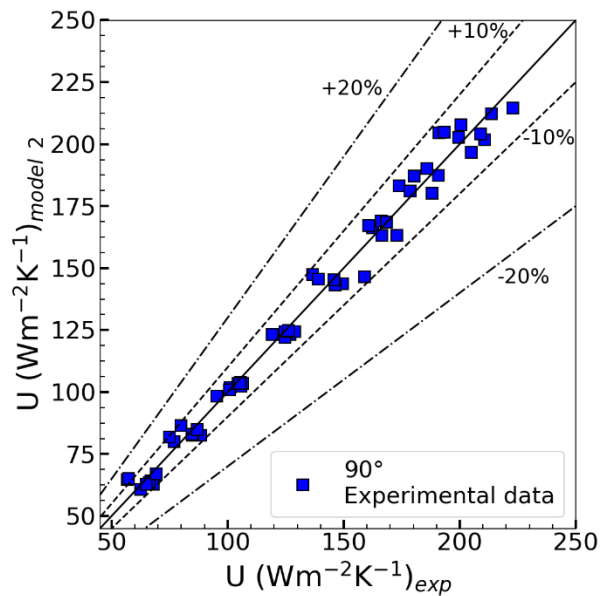


Figure 29 – Overall heat transfer coefficient comparison between the fitted model vs. experimental value for the DBHE 90 air-water experiment.

The negligible convective water thermal resistance assumption, discussed in detail in Section 4.4 under the name of *model 2*, is verified below. The air-side heat transfer coefficient is re-calculated now following *model 3*. In this methodology, the cold fluid heat transfer coefficient in Eq. (4.11) is evaluated through the Nusselt number correlation proposed in Section 5.2- Water-water analysis, through Eq. (5.1). The airside fitting constants on Eq. (4.11) are calculated using the Levenberg-Marquardt non-linear regression method (Moré, 1978) as implemented in (Virtanen et al., 2020), minimizing Eq. (4.14), based on the complete experimental data. Figure 30 compares the different overall heat transfer coefficients obtained through *models 2* and *3*. As seen in Figure 30, the maximum difference among the theoretical overall heat transfer coefficients between *models 2* and *3* is less than 3%, confirming the assumption made, in which the waterside thermal resistance can be neglected for the current experiment.

DBHEs 144 and 180 were tested in similar conditions to the current prototype, i.e. air-water under pressure and temperature conditions close to the present experiment. Batista (2017) and Carqueja (2017) data was revisited, and just like in the present experiment, the water temperature variation is negligible. Consequently, following the same procedure above described, neglecting the water-side convective thermal resistance, the theoretical overall heat

transfer coefficient from Eq. (4.9) is evaluated and compared with its experimental value, Eq. (4.1). The results obtained are shown in Figure 31.

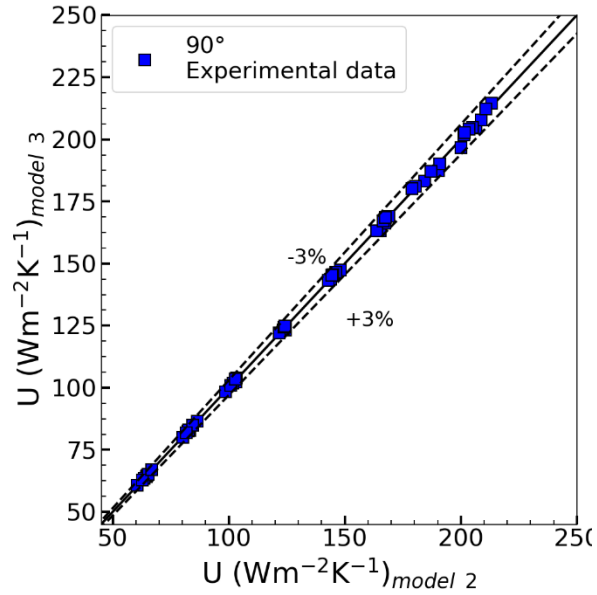


Figure 30 – Comparison of the theoretical overall heat transfer coefficient calculated through model 2 and model 3.

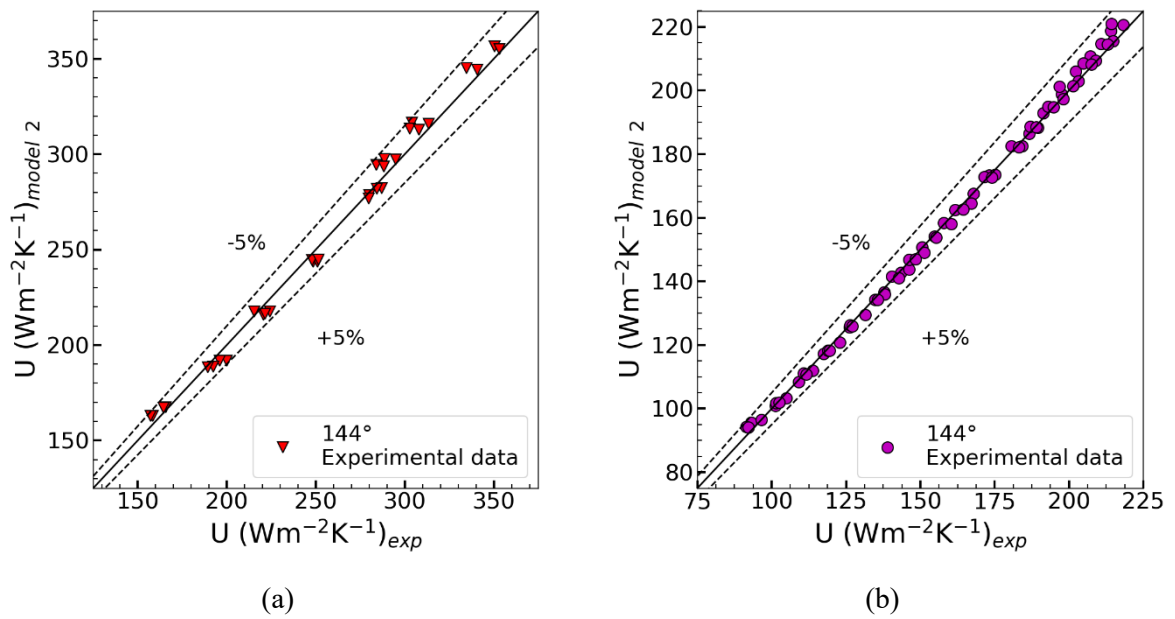


Figure 31 – Overall heat transfer coefficient comparison between the fitted model vs. experimental for (a) DBHE 144 and (b) DBHE 180 air-water experiments.

As seen from Figure 31, both DBHE 144 (a) and DBHE 180 (b) present a low deviation between the theoretical overall heat transfer coefficient and the experimental one. The fitted Nusselt number correlations for the airside for both zigzag channel geometries, i.e. zigzag angle of  $144^\circ$  and  $180^\circ$ , are given by:

$$\begin{aligned} \text{DBHE 144: } Nu &= 0.04617 Re^{0.7546}, 2459 \leq Re \leq 6700, \\ \text{DBHE 180: } Nu &= 0.01160 Re^{0.8460}, 2853 \leq Re \leq 7971. \end{aligned} \quad (5.4)$$

In the continuation, the thermal results of the current prototype, DBHE 90, are compared with the results from prototypes DBHE 144 and 180, (Batista, 2017) and (Carqueja, 2017), respectively. Figure 32 shows the overall heat transfer coefficient vs. the air-side Reynolds number (a), the effectiveness vs. the NTU (b), and the effectiveness vs. air-side Reynolds number (c) for the present experimental data, for DBHEs 90, 144, and 180. As seen in Figure 32(a), rising the air-side Reynolds number increases the overall heat transfer coefficient for all the zigzag DBHEs, but at different rates. The  $180^\circ$  prototype is the less susceptible, with approximately 2.5 times increase in the heat transfer coefficient for a 2.9 times Reynolds number increase, while the  $90^\circ$  is the most susceptible, with almost 4 times heat transfer coefficient rise for a 3.5 times Reynolds number increase. Beyond that, the  $90^\circ$  and  $144^\circ$  zigzag channels seem to offer a similar average increase of approximately 2 times in the heat transfer coefficient, with respect to the straight channel,  $180^\circ$  zigzag. The fact that DBHE 90 prototype is over-dimensioned for the current test facility layout may be at the origin of this result since higher heat transfer rates are expected for sharper zigzag angle channels. Further analysis is necessary to verify this result.

As it can be seen from Figure 32(b), the DBHE 90 prototype effectiveness is very close to one for all experimental data, for an NTU range from approximately 5.9 to 8. The DBHE 144 effectiveness is on average 0.98, for NTU ranging from 3.5 to 4.5 and the DBHE 180 effectiveness ranges from 0.83 to 0.89 for NTU values from 1.8 to 2.2. Besides that, the similarity between the experimental conditions of the different prototypes tested is visible, since the experimental data for all the prototypes present a heat capacity ratio close to  $Cr = 0.08$ , as seen by the theoretical curve also plotted. The high NTU and effectiveness values obtained for

DBHE 144 and especially for DBHE 90 are indications of the prototype over-sizing, tested with low air mass flow rates. The previously explained rollover effect is expected to occur.

Finally, from Figure 32(c) it is seen that the air Reynolds number does not influence the effectiveness of the 90° zigzag prototype, which maintains values close to 1 for all experimental data, while both 144° and 180° prototype effectiveness decrease for increasing values of the air Reynolds number, with the DBHE 180 decrease been more accentuated.

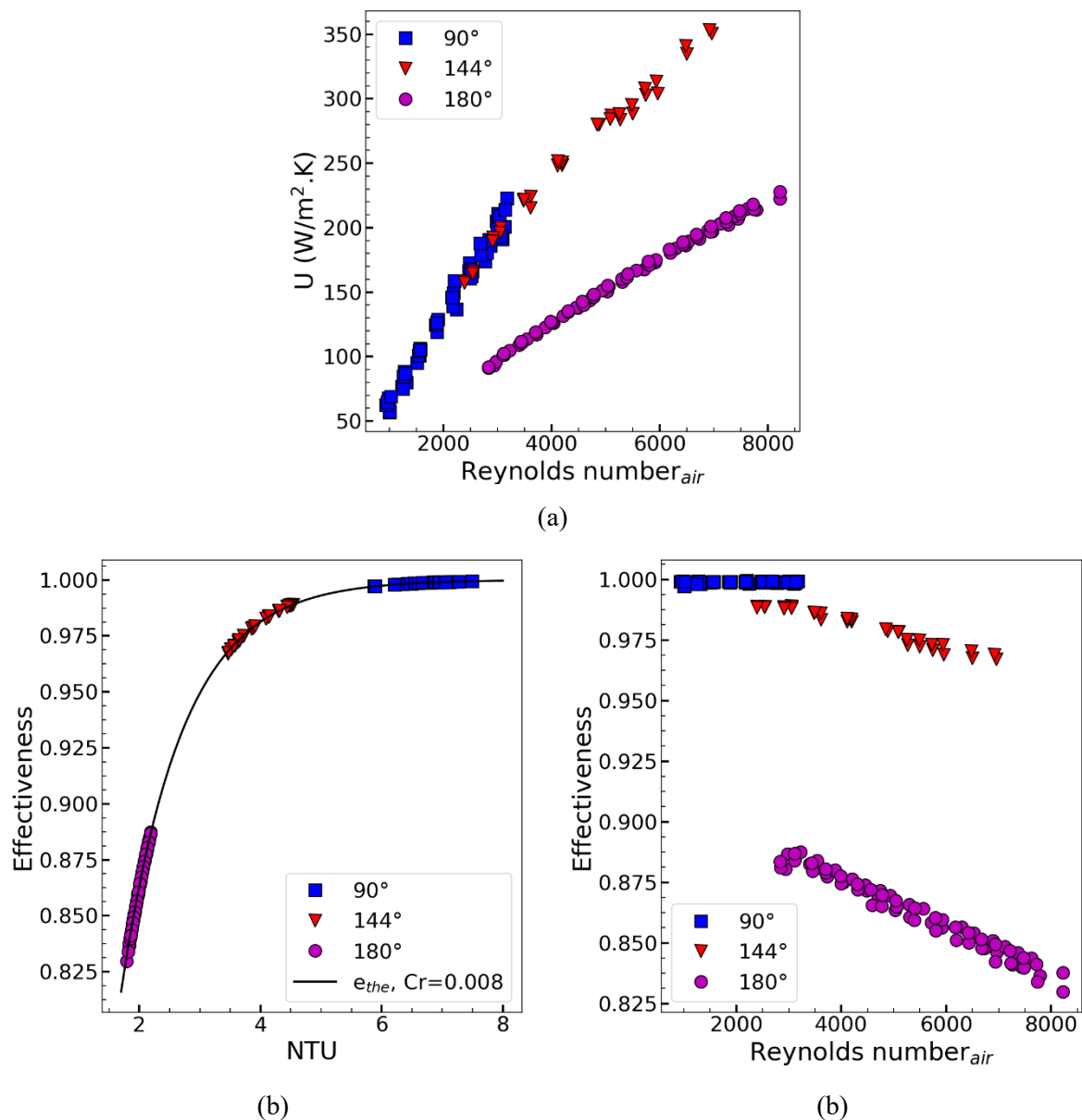


Figure 32 – Thermal results comparison between DBHEs 90, 144 and 180. (a) Overall heat transfer coefficient vs. air side Reynolds number. (b) Effectiveness vs. NTU. (c) Effectiveness vs. air side Reynolds number.

Figure 33 compares the Nusselt number correlation developed in the current experiment, for the 90° zigzag channel, with the revisited data from (Batista, 2017) and (Carqueja, 2017), for the 144° and 180°. Correlations from the literature are also compared: (Kim et al., 2016), for a 100° zigzag angle PCHE numerically studied with CO<sub>2</sub>, (Chen et al., 2016b), for a 150° zigzag channel PCHE tested with He, and (Gnielinski, 2013), for a straight channel fluid flow with Prandtl number equal to the air Prandtl number in DBHE 180. All the Nusselt number correlations present an increasing tendency with rising Reynolds number, with the 90° being the most susceptible, with an increase of 3.7 times in the  $Nu$  with 3.4 times rise in the  $Re$  and the 180° the less susceptible, with 2.4 times  $Nu$  increase with 2.9 times rise in the  $Re$ . The 180° zigzag channel prototype tested in the laboratory presents good accordance with Gnielinski's straight channel Nusselt number, with a small over-estimation for low Reynolds number and small under-estimation for high Reynolds number. The under-estimation can be attributed to the fact that the prototype tested has cross-flow regions at its entrance and exit ports, due to the manufacture restrictions described in Section 4.1, therefore it is not a pure counter-current exchanger. The over-estimation for low  $Re$  needs further investigation. From the overlapping range of  $Re$  values for all the data presented in Figure 33, it can be noticed that the Nusselt number is higher for lower zig-zag angle values. This tendency is expected since higher turbulent flow is expected for more accentuated zigzag curves. Although the DBHE 90 does not seem to offer a great increase in the  $Nu$  when compared to DBHE 144, these results can be caused due to the over-dimensioning of the prototype, as previously discussed. Indeed, the relative uncertainty of the 90°  $Nu$  correlation is as high as 91%, as shown in Table 8, while the 144° and 180°  $Nu$  correlations maximum uncertainties, Table 9 and Table 10, is 14.5% and 3.8%, respectively.

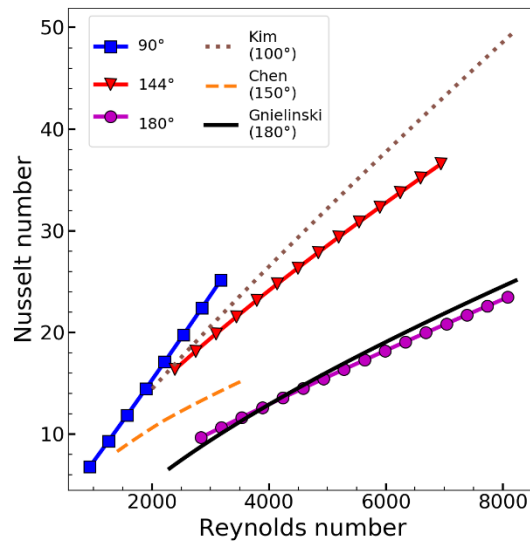


Figure 33 – Nusselt number correlations comparison between the present 90° zigzag channel, 144° zigzag channel (DBHE 144), 180° zigzag channel (DBHE 180), (Kim et al., 2016) 100° zigzag channel, (Chen et al., 2016b) 150° zigzag channel, and (Gnielinski, 2013) straight duct.

### 5.3.2 Air-water hydraulic analysis

The hot stream core pressure drop was evaluated during the experiments. Figure 34 shows the current core pressure drop and also data from DBHEs with 144° zigzag channel (Batista, 2017) and 180° (Carqueja, 2017). It is important to note that, for the current DBHE 90 experiments, the measured pressure drop corresponds solely to the heat exchanger core since the pressure transducers are positioned downstream to the inlet header and upstream to the outlet header. The pressure drop data from (Batista, 2017) and (Carqueja, 2017) were obtained from pressure transducers positioned upstream the inlet header and downstream the outlet header, therefore, their measured data comprises pipes and headers. Their influence was calculated through the methodology described in Section 4.5, using Eqs. (4.18) and (4.19), with expansion and contraction constants estimated as  $K_e = 0.46$  and  $K_c = 0.31$ . As it can be seen, the pressure drops increase monotonically with rising Reynolds number values, for all DBHEs evaluated. For a fixed Reynolds number value, DBHE 90 presents the highest pressure drop values, followed by DBHE 144 and by DBHE 180, respectively. DBHE 90 also presents the highest pressure drop increase, from approximately 1.4 kPa to 9.6 kPa, for Reynolds values from approximately 991 to 3069. DBHE 180 has the lowest pressure drop increase, from approximately 0.8 kPa to 7.2 kPa, for a Reynolds number increase from approximately 2895 to 7975.

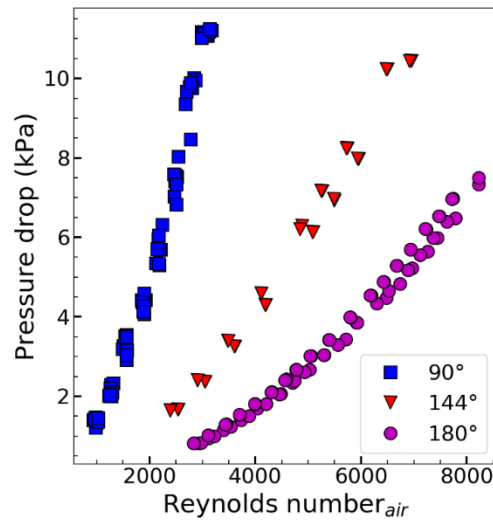


Figure 34 – Core pressure drop along the air-side of DBHEs 90, 144 and 180.

As mentioned, for the current experiment, the measured pressure drop corresponds solely to the heat exchanger core, i.e. the core's channel, and entrance contraction and the exit expansion effects, estimated as  $K_c = 0.56$  and  $K_e = 0.53$ , respectively. For the 144° and 180° zigzag DBHEs, the core entrance and exit effects are estimated as  $K_c = 0.52$  and  $K_e = 0.54$ . The Fanning friction factor is calculated from Eq. (4.21) for the three DBHEs, and their results are shown in Figure 35. As it can be seen, the 90° and the 144° zigzag channels present decreasing Fanning friction factors for rising Reynolds numbers, while the 180° channel Fanning friction factor increases for Reynolds number values up to near 5000, and then remains constant.

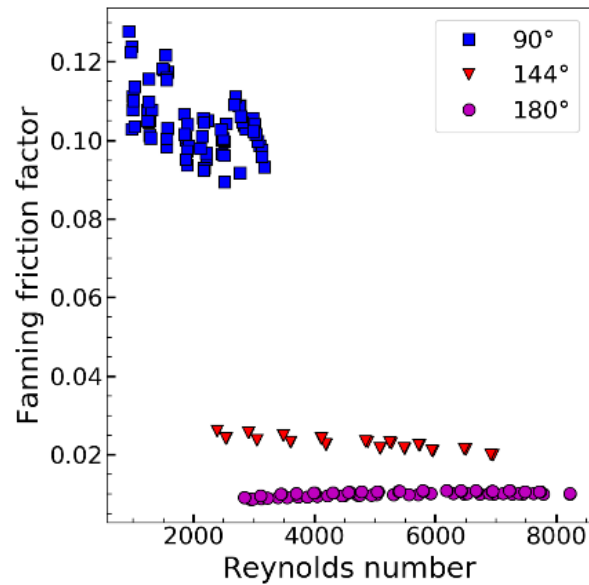


Figure 35 – Fanning friction factor experimental data for DBHEs 90, 144 and 180.

Friction correlations are proposed based on the presented Fanning friction factor data for the three DBHEs evaluated. The fitting parameters of Eq. (4.22) are calculated using the Levenberg-Marquardt non-linear regression method (Moré, 1978) as implemented in (Virtanen et al., 2020), minimizing Equation (4.23) and the fitting constants  $N$  and  $n$  are calculated. The calculated Fanning friction factor is compared to the experimental data using Eqs. (4.22) and (4.21) and the result is presented in Figure 36, for DBHEs 90, 144. Noticing that the DBHE 180 Fanning friction factor presents two tendencies, its corresponding data was split into two ranges, (1) for  $Re < 5000$  and (2)  $Re > 5000$ .

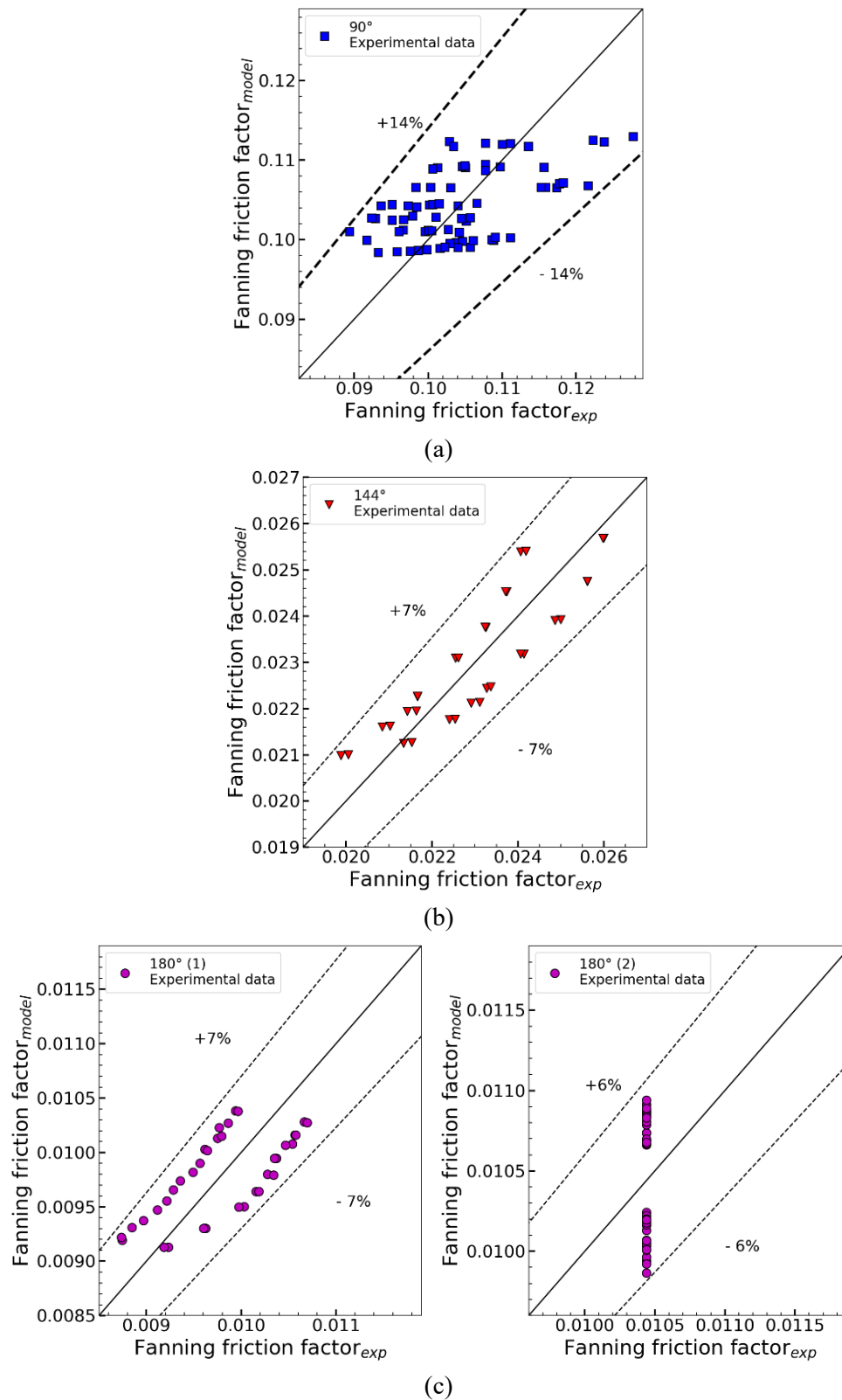


Figure 36 – Experimental and model Fanning friction factor comparison for (a) DBHE 90, (b) DBHE 144, (c) DBHE 180.

As can be seen in Figure 36, the experimental and the model values show a good agreement for all sets of experimental data. The maximum difference, 14%, occurs for DBHE 90, and the minimum, 6%, for the second Reynolds number range of DBHE 180. The fitted Fanning friction factor correlations, as shown in Eq. (4.21), with their corresponding constants, is shown below:

$$\begin{aligned}
 \text{DBHE 90: } f &= 0.2442 \cdot Re^{-0.1127}, 928 \leq Re \leq 3175, \\
 \text{DBHE 144: } f &= 0.1123 \cdot Re^{-0.1897}, 2383 \leq Re \leq 6944, \\
 \text{DBHE 180 (1): } f &= 0.001782 \cdot Re^{0.2055}, 2769 \leq Re \leq 5171, \\
 \text{DBHE 180 (2): } f &= 0.01044, 5171 \leq Re \leq 8220.
 \end{aligned} \tag{5.5}$$

Figure 37 compares the obtained Fanning frictional factor curves within each other and with the following correlations available in the Literature: (Chen et al., 2016b) for a 150° zigzag channel operating with He, (Kim et al., 2016) correlation for a 100° zigzag channel operating with CO<sub>2</sub>, and Shah correlation for a straight duct (Shah; Sekulic, 2003). It can be noticed a good agreement between the proposed correlation from DBHE 180 and Shah's correlation for a straight tube. The proposed Fanning friction factor for the 90° zigzag channel presents close values to (Kim et al., 2016) correlation for a 100° zigzag channel. Moreover, it is also seen that lower zigzag angles result in higher Fanning friction factor coefficients. This tendency is expected since passing from a straight duct to a sharper zigzag angle, e.g. 180° to 90°, generates discontinuities in the fluid path. As noticed from Figure 37, the sharper the zigzag angle, the higher the Fanning friction factor values. In the overlapping Reynolds number for the DBHEs tested at LABTUCAL, the 90° zigzag channel Fanning frictional factor is about 4 times larger than the 144° zigzag, and 11 times larger when compared to the 180° channel.

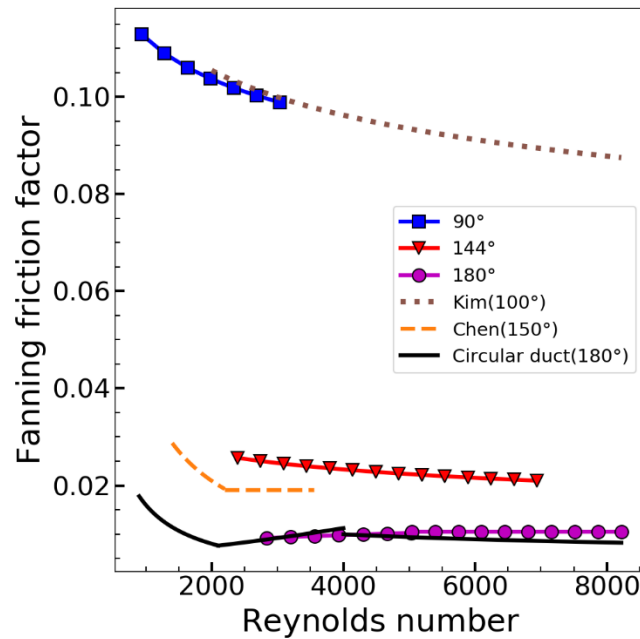


Figure 37 – Fanning friction factor correlation comparison with circular straight tube (Shah; Sekulic, 2003), (Chen et al., 2016b) for a 150° zigzag channel and (Kim et al., 2016) for a 100° zigzag channel

### 5.3.3 Air-water thermal and hydraulic comparison: DBHEs 90, 144 and 180

The dimensionless heat transfer and pressure drop characteristics of the different zigzag channel configurations from DBHEs 90, 144 and 180 are gathered together for comparison. The Colburn factor and the Fanning friction factor are shown in Figure 38, as a function of the Reynolds number. The curves of  $j$  vs.  $Re$  and  $f$  vs.  $Re$  curves are expected to be parallel (Shah; Sekulic, 2003). This is the case for the 144° zigzag channel data in which the ratio between  $f$  and  $j$  is approximately 3.5 for all  $Re$  range tested. For the 180° channel, the  $f$  curve increasing tendency is far from a parallel relative to  $j$ , for  $Re < 5000$ , which may occur due to the transition in the flow regime. For the 90° zigzag channel, the rollover effect on the  $j$  curve may be at the origin of the non-parallelism with the  $f$  curve. Indeed, as previously described and as seen in Figure 17, the drop-off on the  $j$  curve is expected for low air mass flow rates in experimental setups. Table 11 shows the Colburn factor and Fanning friction factor ratios between the three DBHEs, for their respective overlapping Reynolds number ranges. As it can be seen, the 90° zigzag channel increases the Colburn factor on average 1.2 times when

compared to the 144° zigzag, and 2.3 times when compared to the straight channel. On the other hand, the Fanning friction factor rise for the same geometries is 4.1 times and 9.9 times higher, respectively. Therefore, it can be concluded that the 90° zigzag angle tested in the current work offers a similar heat transfer rate increase than the 144° zigzag, at the cost of a much higher Fanning friction factor rise. However, as noted earlier, the thermal results of the present 90° geometry should be further investigated through a properly sized test bench and prototype.

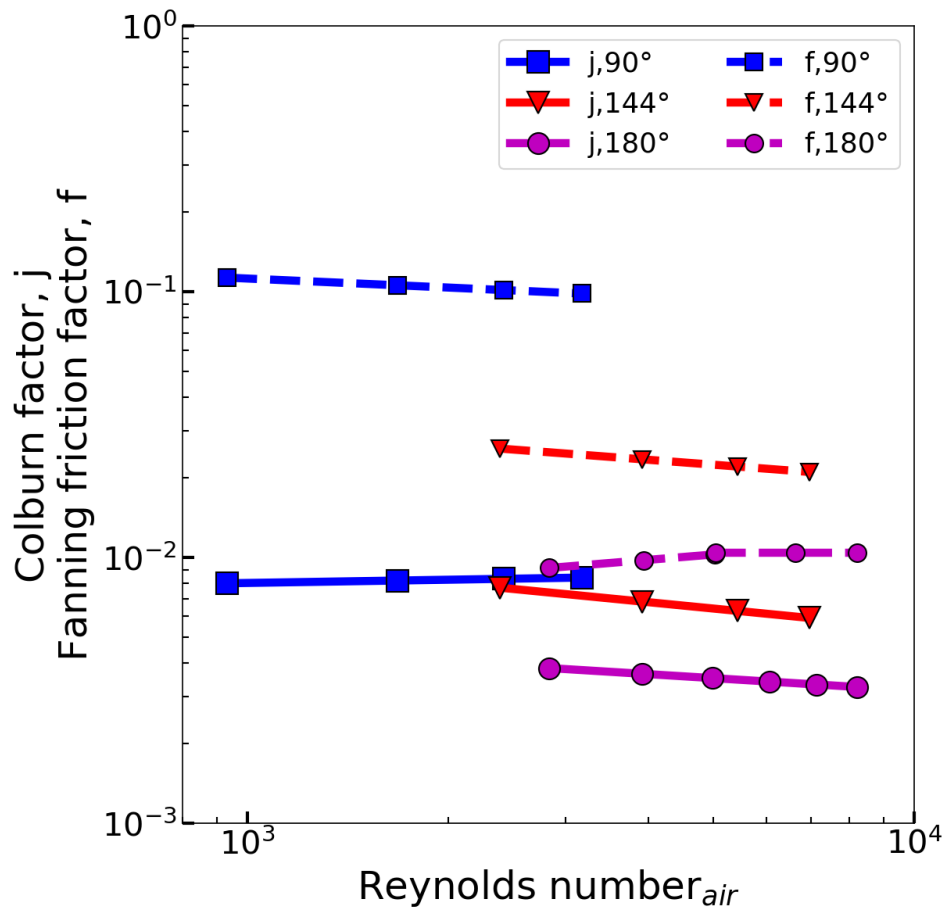


Figure 38 – Colburn factor and Fanning friction factor vs. air Reynolds number for DBHEs 90, 144 and 180.

Table 11 – DBHEs 90, 144 and 180 Colburn and Fanning friction factors average ratio.

	$\frac{j_{90}}{j_{144}}$	$\frac{f_{90}}{f_{144}}$	$\frac{j_{90}}{j_{180}}$	$\frac{f_{90}}{f_{180}}$	$\frac{j_{144}}{j_{180}}$	$\frac{f_{144}}{f_{180}}$
<b>2769 &lt; Re &lt; 3175</b>	1.2	4.1	2.3	9.9	1.9	2.4
<b>5171 &lt; Re &lt; 8220</b>	N/A	N/A	N/A	N/A	1.8	2.0

## 6 CONCLUSIONS AND FUTURE WORK

A diffusion-bonded heat exchanger prototype was thermally and hydraulically tested in an experimental facility, with two different fluid streams configuration, i.e. water-water and air-water. In the first configuration presented, in which water was used in both fluid streams at different mass flow conditions, the heat exchanger presented a correct functioning. The effects on thermal performance caused by the variation of fluids inlet conditions were presented, and their behavior was analyzed. The heat transfer characteristic of the equipment surface, a non-straight square cross-section channel, with a zigzag angle of  $90^\circ$ , was evaluated through an analysis of the heat exchanger's overall thermal resistance. Thus, a Nusselt number correlation was proposed as a function of the Reynolds and Prandtl numbers, for water flowing from the transition to turbulent flow regime. Finally, the result obtained by the correlation for the current geometry is compared to other channel configurations in the literature. The main results obtained from this stage of the work are:

- The Nusselt number curve obtained for a  $90^\circ$  zigzag channel is compared with a theoretical model of a diffusion-bonded heat exchanger with a straight channel, operating in similar conditions as the present prototype. An enhancement of up to 3.5 times was observed for the current  $90^\circ$  zigzag channel compared to the straight channel, for lower Reynolds numbers.
- The Nusselt number correlation proposed for the  $90^\circ$  zigzag channel geometry was compared with the only zigzag Nusselt number correlation for water available for a printed circuit heat exchanger in the literature, for the transition to turbulent regimes. Moreover, the experimental literature data from a  $150^\circ$  zigzag channel geometry of a printed circuit heat exchanger operating as a pre-cooler in an S-CO<sub>2</sub>-water Brayton cycle was used for comparison. For Reynolds number up to 2300, an average enhancement of 4.1 times is achieved for the  $90^\circ$  zigzag channel when compared to Gnielinki's model for a straight channel, while the  $100^\circ$  zigzag channel enhancement is 3.1 times. For the  $150^\circ$ , no apparent improvement with respect to the straight channel was noticed.

In its second testing configuration with air and water fluid streams, the diffusion-bonded heat exchanger did not present a proper functioning, due to being over-dimensioned for

the tested bench capabilities. Indeed, for the current fluid mass flows and specific heat capacities, the heat capacity ratio is near to zero for all the experimental data,  $C_r = C_{air}/C_{water} \approx 0$ . As a result, two major difficulties were faced. First, the temperature increase in the cold fluid side, water, is as small as the sensor error, leading to uncertainties of up to 100% in the reading measurement, influencing the thermal parameters subsequently calculated. Second, the heat exchanger size is too large, causing the air side stream to reach values very close to its final temperature long before the end of the equipment, again impacting the thermal performance of the heat exchanger. The Nusselt number correlation developed for the air stream is expected to be lower than the actual value this geometry may achieve. On the other hand, the hydraulic performance of the diffusion-bonded heat exchanger is not influenced by this setback. Through the pressure drop analysis during the different sets of experiments, the Fanning friction factor correlation is proposed in terms of the Reynolds number, for a laminar flow to transition regimes. Both the thermal and hydraulic characteristics for the 90° zigzag channel operating with air were compared with data from other similar manufactured equipment from *Labtucal*. These diffusion-bonded heat exchangers had channels with zigzag angles of 144° and 180° (this last a straight channel), tested in with hot-water and cold-air, i.e. the inverse fluid configuration than the actual tests. The main results obtained for the air-water tests are:

- The high values of effectiveness and NTU for the current prototype tested in this work are indicators of its over-dimensioned size. The high NTU occurs at low airflow values, in which both temperature and mass flow measurements become more inaccurate.
- Through the comparison of the different Nusselt number reduction methods presented, the initial assumption that the water-side thermal resistance may be neglected face to the air-side convective resistance was confirmed. Next, Nusselt number correlations were proposed from the current zigzag heat exchanger tested and the other two equipment tested in the laboratory which experimental data was revisited.
- The correlations for the zigzag channels of 90°, 144° and 180° are proposed in terms of Reynolds number, and compared with each other and with other correlations from the literature, for different zigzag angles. It is shown that the Nusselt number correlation, and consequently the heat transfer capabilities of the channels, are directly related to the zigzag angles of the channels, the 90° channel (the sharpest zigzag evaluated) presenting the highest values.

- The pressure drops data of the diffusion-bonded heat exchangers analyzed were reduced to the dimensionless Fanning friction factor, and correlations were proposed in terms of the Reynolds number.
- The friction factor correlations for the current prototype and the revisited data are compared with each other and with other zigzag geometries correlations available in the literature. Similarly, as in the heat transfer, sharper zigzag angles have higher friction factors, leading to greater pressure losses.
- From the comparison between Colburn and Fanning friction factors for the zigzag geometries tested in *Labtucal*, the 90° zigzag seems to offer similar heat transfer enhancement to the 144° zigzag, when compared to the 180° channel. However, the 90° channel offers a much higher increase in the friction factor than the 144°, when compared with the straight channel.

While the thermal results for the current layout should not be extended beyond the results here presented, due to the experimental accuracy problem related, the hydraulic results are reliable, and were not impacted by the testing conditions.

For future works, further investigation on the thermal performance of the 90° zigzag angle channel diffusion-bonded heat exchanger is suggested in the air-water layout. Reducing the number of channels on the water side or shortening the heat exchanger length are possibilities to increase the accuracy of the thermal-related parameters. Beyond that, the following topics are suggested:

- Development of a single Nusselt number (or Colburn factor) and Fanning friction factor correlations in terms of the zigzag angle of the channel, besides the Reynolds and Prandtl numbers.
- Although it is clear that sharper zigzag channels result in higher heat-transfer coefficients when compared to straight channels, they are also responsible for energy losses augment due to larger pressure drops along discontinuities. However, the analysis of individual augmentation parameters does not allow one to conclude how they combine, for good or for worse, from an energetic point of view. The key question that arises is: which of these factors play a major role in an entropic point of view? If this question is addressed, the

Engineer would be able to compare designs and select the most efficient for a specific application, achieving an optimal design.

## BIBLIOGRAPHY

AHN, Y.; LEE, J. I. Study of various Brayton cycle designs for small modular sodium-cooled fast reactor. **Nuclear Engineering and Design**, 276, p. 128-141, 2014.

BAIK, S.; KIM, S. G.; LEE, J.; LEE, J. I. Study on CO<sub>2</sub> – water printed circuit heat exchanger performance operating under various CO<sub>2</sub> phases for S-CO<sub>2</sub> power cycle application. **Applied Thermal Engineering**, 113, p. 1536-1546, 2017.

BATISTA, J. V. C. **Modelagem e Análise Experimental de um Trocador de Calor Compacto de Canais em Zigue-Zague**. Undergraduate Thesis. (Bachelor). Department of Mechanical Engineering - Federal University of Santa Catarina, Florianópolis, 2017.

BEJAN, A.; KRAUS, A. D. **Heat Transfer Handbook**. Hoboken, USA: John Wiley & Sons, 2003.

BELL, I. H.; WRONSKI, J.; QUOILIN, S.; LEMORT, V. Pure and Pseudo-pure Fluid Thermophysical Property Evaluation and the Open-Source Thermophysical Property Library CoolProp. **Ind Eng Chem Res**, 53, n. 6, p. 2498-2508, Feb 2014.

BERGMAN, T. L.; INCROPERA, F. P.; DEWITT, D. P.; LAVINE, A. S. **Fundamentals of Heat and Mass Transfer**. 8th edition. Hoboken, USA: John Wiley and Sons, 2017.

CARQUEJA, G. G. **Modelagem e Análise Experimental de Trocador de Calor Compacto com Canais de Perfil Quadrado**. Undergraduate Thesis. (Bachelor). Department of Mechanical Engineering - Federal University of Santa Catarina, Florianópolis, 2017.

CAVALCANTI ALVAREZ, R.; SARMIENTO, A.; Batista, J. V. C.; MANTELLI, M. B. H. Entropy Generation Analysis Applied to Diffusion-Bonded Compact Heat Exchangers. *In*: AIAA Aviation 2019 Forum, 2019, Dallas, TX, USA.

CHAI, L.; TASSOU, S. A. A review of printed circuit heat exchangers for helium and supercritical CO<sub>2</sub> Brayton cycles. **Thermal Science and Engineering Progress**, 18, p. 100543, 2020.

CHEN, M.; SUN, X.; CHRISTENSEN, R. N.; SHI, S. et al. Experimental and numerical study of a printed circuit heat exchanger. **Annals of Nuclear Energy**, 97, p. 221-231, 2016a.

CHEN, M.; SUN, X.; CHRISTENSEN, R. N.; SKAVDAHL, I. et al. Pressure drop and heat transfer characteristics of a high-temperature printed circuit heat exchanger. **Applied Thermal Engineering**, 108, p. 1409-1417, 2016b.

CHENG, K.; ZHOU, J.; ZHANG, H.; HUAI, X. et al. Experimental investigation of thermal-hydraulic characteristics of a printed circuit heat exchanger used as a pre-cooler for the supercritical CO<sub>2</sub> Brayton cycle. **Applied Thermal Engineering**, 171, p. 115116, 2020.

CHU, W.-x.; LI, X.-h.; MA, T.; CHEN, Y.-t. et al. Experimental investigation on SCO<sub>2</sub>-water heat transfer characteristics in a printed circuit heat exchanger with straight channels. **International Journal of Heat and Mass Transfer**, 113, p. 184-194, 2017.

DAVID SOUTHALL, R. L. P., Stephen John Dewson. Design Considerations for Compact Heat Exchangers. *In: International Congress on Advances in Nuclear Power Plants*, 2008, Anaheim, CA, USA.

DOSTAL, V. **A supercritical carbon dioxide cycle for next generation nuclear reactors**. Doctoral dissertation (Sc.D.). Department of Nuclear Engineering - Massachusetts Institute of Technology, USA, 2004.

FERREIRA, D. d. S. **Análise Experimental do Comportamento Termo-Hidráulico de um Trocador de Calor do Tipo Placas Corrugadas**. Master's Thesis (M.Sc.). Postgraduate Program in Mechanical Engineering - Federal University of Santa Catarina, Florianópolis, 2019.

GATTI, G. M. **Análise Termo-Hidráulica e Efeitos do Escalonamento em Trocadores de Calor Compactos Unidos por Difusão**. Master's Thesis (M.Sc.). Postgraduate Program in Mechanical Engineering - Federal University of Santa Catarina, Florianópolis, 2020.

GNIELINSKI, V. On heat transfer in tubes. **International Journal of Heat and Mass Transfer**, 63, p. 134-140, 2013.

GUO, J.; HUAI, X. Performance Analysis of Printed Circuit Heat Exchanger for Supercritical Carbon Dioxide. **Journal of Heat Transfer**, 139, n. 6, p. 061801, 2017.

HARATYK, G.; SHIRVAN, K.; KAZIMI, M. S. Compact Steam Generator For Nuclear Application. *In: NURETH-16, International Topical Meeting on Nuclear Reactor Thermal Hydraulics*, 2015, Chicago, IL, USA.

HEATRIC. Corporate Brochure. <https://www.heatric.com/home/resources/brochures-downloads/>, Access date: May 27, 2021.

HERMES, C. J. L. Trocadores de Calor Compactos. **Class lecture**, 2018.

HESSELGREAves, J. E.; LAW, R.; REAY, D. **Compact heat exchangers: selection, design and operation**. 2nd edition. [s.l.]: Butterworth-Heinemann, 2016.

HOLMAN, J. P. **Experimental methods for engineers**. Boston, MA, United States: McGraw-Hill Education, 2011.

HUANG, C.; CAI, W.; WANG, Y.; LIU, Y. et al. Review on the characteristics of flow and heat transfer in printed circuit heat exchangers. **Applied Thermal Engineering**, 153, p. 190-205, 2019.

HULSE, P. M. **Fabricação e Análise Estrutural, Morfológica e Termo Hidráulica de um Trocador de Calor Tipo Circuito Impresso**. Master's Thesis (M.Sc.). Postgraduate Program in Mechanical Engineering - Federal University of Santa Catarina, Florianópolis, 2020.

KAKAÇ, S.; LIU, H.; PRAMUANJAROENKIJ, A. **Heat Exchangers: Selection, Rating, and Thermal Design**. 3rd edition. Taylor & Francis, 2012.

KAYS, W. M.; LONDON, A. L. **Compact Heat Exchangers**. 3rd edition. USA: Krieger Publishing Company, 2018.

KIM, D. E.; KIM, M. H.; CHA, J. E.; KIM, S. O. Numerical investigation on thermal-hydraulic performance of new printed circuit heat exchanger model. **Nuclear Engineering and Design**, 238, n. 12, p. 3269-3276, 2008.

KIM, I. H.; NO, H. C. Thermal hydraulic performance analysis of a printed circuit heat exchanger using a helium-water test loop and numerical simulations. **Applied Thermal Engineering**, 31, n. 17-18, p. 4064-4073, 2011.

KIM, I. H.; NO, H. C. Physical model development and optimal design of PCHE for intermediate heat exchangers in HTGRs. **Nuclear Engineering and Design**, 243, p. 243-250, 2012.

KIM, I. H.; NO, H. C. Thermal-hydraulic physical models for a Printed Circuit Heat Exchanger covering He, He-CO<sub>2</sub> mixture, and water fluids using experimental data and CFD. **Experimental Thermal and Fluid Science**, 48, p. 213-221, 2013.

KIM, S. G.; LEE, Y.; AHN, Y.; LEE, J. I. CFD aided approach to design printed circuit heat exchangers for supercritical CO<sub>2</sub> Brayton cycle application. **Annals of Nuclear Energy**, 92, p. 175-185, 2016.

LEE, H. S. **Thermal Design: Heat Sinks, Thermoelectrics, Heat Pipes, Compact Heat Exchangers, and Solar Cells**. Hoboken, USA: John Wiley & Sons, 2010.

LI, W.; YU, G.; YU, Z. Bioinspired heat exchangers based on triply periodic minimal surfaces for supercritical CO<sub>2</sub> cycles. **Applied Thermal Engineering**, 179, p. 115686, 2020.

LIENHARD, I., J. H.; Lienhard, V, J. H. **A Heat Transfer Textbook**. Cambridge, MA: Phlogiston Press, 2020.

MORÉ, J. J. The Levenberg-Marquardt algorithm: Implementation and theory. *In*: Watson G.A. (eds) Numerical Analysis. **Lecture Notes in Mathematics**, 630. Springer, Berlin, Heidelberg, 1978.

MORTEAN, M. V. V. **Trocadores de calor compactos soldados por difusão: fabricação e modelagem**. Doctoral Dissertation (Ph.D.) Postgraduate Program in Mechanical Engineering - Federal University of Santa Catarina, Florianópolis, 2017.

MORTEAN, M. V. V.; CISTERNA, L. H. R.; PAIVA, K. V.; MANTELLI, M. B. H. Development of diffusion welded compact heat exchanger technology. **Applied Thermal Engineering**, 93, p. 995-1005, 2016.

MORTEAN, M. V. V.; CISTERNA, L. H. R.; PAIVA, K. V.; MANTELLI, M. B. H. Thermal and hydrodynamic analysis of a cross-flow compact heat exchanger. **Applied Thermal Engineering**, 150, p. 750-761, 2019.

MORTEAN, M. V. V.; MANTELLI, M. B. H. Nusselt number correlation for compact heat exchangers in transition regimes. **Applied Thermal Engineering**, 151, p. 514-522, 2019.

MORTEAN, M. V. V.; PAIVA, K. V.; MANTELLI, M. B. H. Diffusion bonded cross-flow compact heat exchangers: Theoretical predictions and experiments. **International Journal of Thermal Sciences**, 110, p. 285-298, 2016.

MYLAVARAPU, S. K.; SUN, X.; GLOSUP, R. E.; CHRISTENSEN, R. N. et al. Thermal hydraulic performance testing of printed circuit heat exchangers in a high-temperature helium test facility. **Applied Thermal Engineering**, 65, n. 1-2, p. 605-614, 2014.

NGO, T. L.; KATO, Y.; NIKITIN, K.; ISHIZUKA, T. Heat transfer and pressure drop correlations of microchannel heat exchangers with S-shaped and zigzag fins for carbon dioxide cycles. **Experimental Thermal and Fluid Science**, 32, n. 2, p. 560-570, 2007.

NIKITIN, K.; KATO, Y.; NGO, L. Printed circuit heat exchanger thermal-hydraulic performance in supercritical CO<sub>2</sub> experimental loop. **International Journal of Refrigeration**, 29, n. 5, p. 807-814, 2006.

SAEED, M.; BERROUK, A. S.; SALMAN SIDDIQUI, M.; ALI AWAIS, A. Numerical investigation of thermal and hydraulic characteristics of sCO<sub>2</sub>-water printed circuit heat exchangers with zigzag channels. **Energy Conversion and Management**, 224, p. 113375, 2020.

SAEED, M.; KIM, M.-H. Thermal and hydraulic performance of SCO<sub>2</sub> PCHE with different fin configurations. **Applied Thermal Engineering**, 127, p. 975-985, 2017.

SARKAR, J. Second law analysis of supercritical CO<sub>2</sub> recompression Brayton cycle. **Energy**, 34, n. 9, p. 1172-1178, 2009.

SARMIENTO, A. P. C.; MILANEZ, F. H.; MANTELLI, M. B. H. Theoretical models for compact printed circuit heat exchangers with straight semicircular channels. **Applied Thermal Engineering**, p. 115435, 2020.

SARMIENTO, A. P. C.; SOARES, V. H. T.; CARQUEJA, G. G.; BATISTA, J. V. C. et al. Thermal performance of diffusion-bonded compact heat exchangers. **International Journal of Thermal Sciences**, 153, p. 106384, 2020a.

SARMIENTO, A. P. C.; SOARES, V. H. T.; MILANEZ, F. H.; MANTELLI, M. B. H. Heat transfer correlation for circular and non-circular ducts in the transition regime. **International Journal of Heat and Mass Transfer**, 149, p. 119165, 2020b.

SEO, J.-W.; KIM, Y.-H.; KIM, D.; CHOI, Y.-D. et al. Heat Transfer and Pressure Drop Characteristics in Straight Microchannel of Printed Circuit Heat Exchangers. **Entropy**, 17, n. 5, p. 3438-3457, 2015.

SHAH, R. K.; SEKULIC, D. P. **Fundamentals of heat exchanger design**. Hoboken, USA: John Wiley & Sons, 2003.

SONG, H. **Investigations of a printed circuit heat exchanger for supercritical CO<sub>2</sub> and water**. Master's Thesis (M.Sc.). Department of Mechanical and Nuclear Engineering, Kansas State University, 2007.

TSUZUKI, N.; KATO, Y.; ISHIDUKA, T. High performance printed circuit heat exchanger. **Applied Thermal Engineering**, 27, n. 10, p. 1702-1707, 2007.

VAN METER, J. **Experimental investigation of a printed circuit heat exchanger using supercritical carbon dioxide and water as heat transfer media**. Master's Thesis (M.Sc.). Department of Mechanical and Nuclear Engineering, Kansas State University, 2008.

VIRTANEN, P.; GOMMERS, R.; OLIPHANT, T. E.; HABERLAND, M. et al. SciPy 1.0: fundamental algorithms for scientific computing in Python. **Nat Methods**, 17, n. 3, p. 261-272, Mar 2020.

WANG, W.-Q.; QIU, Y.; HE, Y.-L.; SHI, H.-Y. Experimental study on the heat transfer performance of a molten-salt printed circuit heat exchanger with airfoil fins for concentrating solar power. **International Journal of Heat and Mass Transfer**, 135, p. 837-846, 2019.

ZHOU, J.; CHENG, K.; ZHANG, H.; LIU, B. et al. Test platform and experimental test on 100 kW class Printed Circuit Heat Exchanger for Supercritical CO<sub>2</sub> Brayton Cycle. **International Journal of Heat and Mass Transfer**, 148, p. 118540, 2020.

## APPENDIX A –Experimental data

The experimental data collected in the current work for the heat exchanger prototype, DBHE 90. is shown hereafter for the two test facilities' layouts, i.e. water-water and air-water.

Table 12 – DBHE 90 water-water experimental data.

Set	Test	$\dot{m}_{h,in}$ , kg/s	$\dot{m}_{c,in}$ , kg/s	$T_{h,in}$ , °C	$T_{c,in}$ , °C	$T_{h,out}$ , °C	$T_{c,out}$ , °C	$P_{h,in}$ , bar	$P_{c,in}$ , bar
1	1	0.401	0.409	48.45	23.30	34.65	36.63	1.1	1.5
1	2	0.649	0.408	49.54	23.17	39.02	39.61	1.1	1.5
1	3	0.899	0.408	48.66	23.28	40.78	40.34	1.1	1.5
1	4	1.151	0.408	48.65	23.34	42.23	41.12	1.1	1.5
1	5	1.400	0.408	48.62	23.27	43.18	41.61	1.1	1.5
1	6	1.649	0.408	48.65	23.29	43.94	42.04	1.1	1.5
1	7	1.904	0.406	48.61	22.85	44.42	42.24	1.1	1.5
2	8	0.402	0.653	48.41	23.75	32.76	33.15	1.1	1.6
2	9	0.650	0.652	48.55	24.14	36.69	35.63	1.2	1.6
2	10	0.900	0.652	48.51	24.33	39.07	37.00	1.2	1.6
2	11	1.152	0.652	48.49	24.71	40.76	38.00	1.2	1.6
2	12	1.405	0.654	48.59	23.28	41.52	38.03	1.2	1.6
2	13	1.653	0.654	48.64	23.50	42.49	38.61	1.2	1.6
2	14	1.903	0.655	48.67	23.44	43.19	38.96	1.2	1.6
3	15	0.399	0.910	48.59	24.76	32.36	31.65	1.2	2.1
3	16	0.646	0.912	48.61	25.55	36.20	34.06	1.2	2.1
3	17	0.898	0.912	48.49	25.38	38.29	35.10	1.4	2.1
3	18	1.153	0.912	48.59	25.14	39.84	35.83	1.4	2.1
3	19	1.405	0.906	48.60	22.44	40.19	35.05	1.4	2.1
3	20	1.652	0.906	48.52	22.47	41.13	35.52	1.4	2.1
3	21	1.903	0.905	48.43	22.90	41.97	36.08	1.4	2.1
4	22	0.400	1.153	48.61	22.58	30.20	28.74	1.4	2.5
4	23	0.648	1.154	48.55	22.75	33.88	30.70	1.4	2.5
4	24	0.902	1.154	48.66	23.30	36.68	32.32	1.4	2.5
4	25	1.156	1.155	48.60	23.32	38.42	33.13	1.6	2.5
4	26	1.404	1.154	48.22	22.61	39.24	33.15	1.6	2.5
4	27	1.655	1.152	48.14	23.39	40.44	34.05	1.6	2.5
4	28	1.904	1.152	47.27	23.25	40.57	33.93	1.6	2.5
5	29	0.403	1.404	48.52	23.07	29.98	28.21	1.6	1.6
5	30	0.653	1.404	48.47	23.45	33.64	30.10	1.6	1.6
5	31	0.905	1.404	48.59	24.02	36.39	31.60	1.6	1.6
5	32	1.160	1.404	49.60	24.17	38.75	32.80	1.6	1.6
5	33	1.406	1.404	48.64	24.18	39.50	33.01	1.8	1.6
5	34	1.653	1.404	48.60	24.10	40.44	33.36	1.8	1.6

5	35	1.902	1.404	48.54	24.04	41.20	33.64	1.8	1.6
6	36	0.401	1.657	48.75	24.32	30.56	28.56	1.8	2.2
6	27	0.650	1.658	48.88	24.96	34.23	30.49	1.8	2.2
6	28	0.903	1.657	48.64	24.99	36.44	31.38	1.8	2.2
6	29	1.155	1.657	49.42	25.37	38.69	32.56	1.8	2.2
6	40	1.404	1.656	48.69	24.96	39.39	32.54	1.8	2.2
6	41	1.653	1.657	48.47	23.32	39.69	31.75	2.1	2.2
6	42	1.903	1.658	48.45	23.27	40.52	32.04	2.1	2.2
7	43	0.404	1.907	48.50	22.51	28.94	26.49	2.1	2.8
7	44	0.653	1.908	48.55	22.87	32.54	28.14	2.1	2.8
7	45	0.906	1.908	48.41	23.49	35.23	29.50	2.1	2.8
7	46	1.158	1.907	48.55	23.46	37.06	30.17	2.1	2.8
7	47	1.406	1.907	48.52	24.44	38.76	31.35	2.1	2.8
7	48	1.653	1.908	49.68	24.78	40.63	32.33	2.1	2.8
7	49	1.901	1.907	48.99	24.88	41.06	32.48	2.5	2.8
8	50	0.401	2.162	50.65	24.14	30.40	27.77	2.5	3.5
8	51	0.649	2.161	50.66	24.45	33.97	29.28	2.5	3.5
8	52	0.901	2.162	50.72	24.72	36.61	30.38	2.5	3.5
8	53	1.155	2.162	50.58	24.65	38.35	30.94	2.5	3.5
8	54	1.405	2.162	50.46	24.77	39.73	31.47	2.5	3.5
8	55	1.656	2.163	49.59	24.83	40.33	31.65	2.5	3.5
8	56	1.903	2.165	48.56	24.67	40.47	31.52	2.5	3.5

Table 13 – DBHE 90 air-water experimental data.

Set	Test	$\dot{m}_{h,in}$ , kg/s	$\dot{m}_{c,in}$ , kg/s	$T_{h,in}$ , °C	$T_{c,in}$ , °C	$T_{h,out}$ , °C	$T_{c,out}$ , °C	$\Delta P_{h,core}$ Pa	$P_{h,out}$ Pa	$P_{c,in}$ , bar
1	0	7.341E-03	0.4005	75.316	22.121	22.047	22.324	1332	101325	1.3
1	1	9.404E-03	0.4007	75.167	22.008	21.979	22.269	2121	101325	1.3
1	2	1.156E-02	0.4010	75.068	22.125	22.100	22.465	3550	101325	1.3
1	3	1.386E-02	0.4015	75.007	22.329	22.311	22.708	4351	101325	1.3
1	4	1.632E-02	0.4017	74.925	22.202	22.221	22.641	5693	101325	1.3
1	5	1.826E-02	0.4017	74.851	21.990	22.031	22.499	7426	101325	1.3
1	6	2.095E-02	0.4011	74.824	21.705	21.759	22.303	10019	101325	1.3
1	7	2.199E-02	0.3994	74.848	21.732	21.779	22.363	11175	101325	1.3
2	8	7.377E-03	0.6571	75.224	20.278	20.433	20.399	1382	101325	1.6
2	9	9.057E-03	0.6605	75.155	20.104	20.189	20.257	2013	101325	1.6
2	10	1.107E-02	0.6635	75.114	19.981	20.059	20.186	3263	101325	1.6
2	11	1.377E-02	0.6652	75.046	19.656	19.733	19.895	4300	101325	1.6
2	12	1.643E-02	0.6683	75.008	19.190	19.290	19.482	6321	101325	1.6
2	13	1.847E-02	0.6673	74.851	19.206	19.275	19.527	7527	101325	1.6
2	14	2.033E-02	0.6689	74.816	19.008	19.092	19.379	9842	101325	1.6

2	15	2.270E-02	0.6682	74.803	18.712	18.806	19.106	11079	101325	1.6
3	16	7.160E-03	0.9014	75.324	18.990	19.031	19.083	1205	101325	2.0
3	17	9.324E-03	0.9019	75.216	19.060	19.101	19.180	2004	101325	2.0
3	18	1.143E-02	0.9030	75.089	18.892	18.958	19.038	2913	101325	2.0
3	19	1.388E-02	0.9030	75.035	18.847	18.895	19.020	4067	101325	2.0
3	20	1.596E-02	0.9028	75.011	18.719	18.764	18.917	5301	101325	2.0
3	21	1.810E-02	0.9045	74.921	18.730	18.781	18.961	7024	101325	2.0
3	22	2.102E-02	0.9017	74.861	18.661	18.728	18.939	9948	101325	2.0
3	23	2.294E-02	0.9011	74.780	18.608	18.681	18.904	11177	101325	2.0
4	24	7.236E-03	1.1547	75.370	21.258	21.252	21.337	1481	101325	1.1
4	25	9.326E-03	1.1547	75.198	20.878	20.931	20.978	2289	101325	1.1
4	26	1.131E-02	1.1546	75.130	20.531	20.592	20.657	3516	101325	1.1
4	27	1.358E-02	1.1550	75.043	20.305	20.355	20.446	4428	101325	1.1
4	28	1.587E-02	1.1544	74.981	20.120	20.169	20.284	5949	101325	1.1
4	29	1.866E-02	1.1545	74.897	20.013	20.076	20.206	8029	101325	1.1
4	30	2.062E-02	1.1540	74.883	19.845	19.916	20.058	9764	101325	1.1
4	31	2.254E-02	1.1526	74.840	19.677	19.757	19.906	11066	101325	1.1
5	32	7.423E-03	1.4091	75.338	20.665	20.817	20.729	1387	101325	1.5
5	33	9.237E-03	1.4105	75.247	20.966	20.986	21.047	2037	101325	1.5
5	34	1.093E-02	1.4095	75.129	20.971	20.986	21.072	3198	101325	1.5
5	35	1.412E-02	1.4120	75.036	21.165	21.170	21.284	4427	101325	1.5
5	36	1.621E-02	1.4121	75.019	20.970	21.001	21.106	5695	101325	1.5
5	37	1.825E-02	1.4127	74.998	21.095	21.100	21.249	7413	101325	1.5
5	38	2.024E-02	1.4116	74.931	21.195	21.214	21.371	9781	101325	1.5
5	39	2.213E-02	1.4112	74.888	21.316	21.353	21.504	11139	101325	1.5
6	40	6.919E-03	1.6510	75.301	24.885	24.770	24.945	1405	101325	2.0
6	41	9.732E-03	1.6537	75.153	23.163	23.262	23.242	2332	101325	2.0
6	42	1.155E-02	1.6540	75.058	22.816	22.862	22.910	3505	101325	2.0
6	43	1.397E-02	1.6558	74.957	22.845	22.848	22.950	4585	101325	2.0
6	44	1.607E-02	1.6541	74.907	22.641	22.713	22.764	6054	101325	2.0
6	45	1.839E-02	1.6540	74.896	22.156	22.223	22.292	7566	101325	2.0
6	46	1.989E-02	1.6535	74.886	22.026	22.082	22.179	9673	101325	2.0
6	47	2.236E-02	1.6525	74.821	22.096	22.139	22.259	11117	101325	2.0
7	48	7.156E-03	1.9055	75.341	23.946	23.929	24.009	1438	101325	2.7
7	49	9.351E-03	1.9057	75.142	24.216	24.162	24.291	2198	101325	2.7
7	50	1.156E-02	1.9061	75.036	24.343	24.300	24.431	3502	101325	2.7
7	51	1.378E-02	1.9061	74.975	24.546	24.529	24.644	4376	101325	2.7
7	52	1.583E-02	1.9054	74.956	24.231	24.241	24.339	5705	101325	2.7
7	53	1.819E-02	1.9085	74.879	24.377	24.399	24.500	7586	101325	2.7
7	54	2.055E-02	1.9077	74.810	24.383	24.400	24.520	9889	101325	2.7
7	55	2.214E-02	1.9074	74.738	24.225	24.278	24.369	11019	101325	2.7
8	56	7.595E-03	2.1454	75.257	22.325	22.298	22.394	1370	101325	3.4
8	57	9.541E-03	2.1466	75.165	22.394	22.367	22.472	2095	101325	3.4
8	58	1.159E-02	2.1468	75.062	22.411	22.410	22.501	3149	101325	3.4
8	59	1.393E-02	2.1467	74.990	22.436	22.440	22.536	4272	101325	3.4
8	60	1.559E-02	2.1471	74.965	22.370	22.396	22.480	5358	101325	3.4
8	61	1.850E-02	2.1463	74.874	22.077	22.129	22.202	7333	101325	3.4

8	62	2.039E-02	2.1485	74.815	22.142	22.163	22.272	8460	101325	3.4
8	63	2.341E-02	2.1456	74.809	22.496	22.533	22.641	11208	101325	3.4
9	64	7.486E-03	2.3099	75.304	19.173	19.179	19.251	1451	101325	3.9
9	65	9.225E-03	2.3126	75.233	21.842	21.950	21.924	2042	101325	3.9
9	66	1.154E-02	2.3147	75.208	22.140	22.140	22.232	3042	101325	3.9
9	67	1.384E-02	2.3140	75.144	22.176	22.172	22.277	4128	101325	3.9
9	68	1.601E-02	2.3149	74.986	22.215	22.211	22.325	5336	101325	3.9
9	69	1.848E-02	2.3162	74.926	22.290	22.304	22.410	6830	101325	3.9
9	70	1.972E-02	2.3148	74.892	22.236	22.273	22.371	9360	101325	3.9
9	71	2.315E-02	2.3136	74.868	22.205	22.251	22.350	11243	101325	3.9

---

## APPENDIX B – Uncertainty analysis

The mean value of a directly measured parameter  $x$  and its number of degrees of freedom is given by, respectively,

$$\bar{x} = \frac{1}{n} \sum_{i=1}^n x_i, \quad (\text{B.1})$$

$$\nu = n - 1, \quad (\text{B.2})$$

where  $n$  is the number of measurements. A systematic uncertainty in the measured parameter,  $s(x)$ , accounts for fixed errors in the measurement equipment, and its value is given by the sensors' manufacturers. A random source of uncertainty,  $r(x)$ , accounts for fluctuations in time during measurements reading and is evaluated as shown in

$$r = \left[ \frac{1}{n-1} \sum_{i=1}^n (x_i - \bar{x})^2 \right]^{1/2}. \quad (\text{B.3})$$

The combined uncertainty,  $u(x)$ , of the contributions above cited is given by

$$u(x) = \sqrt{[s(x)]^2 + [r(x)]^2}. \quad (\text{B.4})$$

An indirectly measured parameter, evaluated through mathematical operations involving directly measured parameters, as in  $y(x) = f(x_1, \dots, x_q)$ , has a combined uncertainty calculated by

$$u(y) = \left[ \sum_{j=1}^q \left( \frac{\partial y}{\partial x_j} \right)^2 \right]^{\frac{1}{2}}. \quad (\text{B.5})$$

The number of degrees of freedom of  $y$  is calculated as shown in

$$\frac{\left[ \frac{u(y)}{y} \right]^4}{\nu_y} = \sum_{j=1}^q \frac{\left[ \frac{u(x_j)}{x_j} \right]^4}{\nu_j}. \quad (\text{B.6})$$

Finally, the expanded uncertainty of a direct or indirect measured parameter is calculated by

$$E = u \cdot t \quad (\text{B.7})$$

where  $t$  accounts for the t-Student parameter, determined by the number of degrees of freedom of the variable evaluated, for a confidence interval of 95%.

The uncertainty of the main parameters was calculated using the method above presented, in which the geometric parameters and the fluid's properties were considered as well-known values, therefore with null uncertainties. The simplified combined uncertainties are presented below.

Heat transfer rate,  $Q$ :

$$\begin{aligned}
 u(Q) &= \sqrt{\left[\frac{\partial Q}{\partial m} u(m)\right]^2 + \left[\frac{\partial Q}{\partial c_p} u(c_p)\right]^2 + \left[\frac{\partial Q}{\partial T} u(\Delta T)\right]^2} = \\
 &= Q \sqrt{\left[\frac{u(m)}{m}\right]^2 + \left[\frac{u(\Delta T)}{\Delta T}\right]^2}.
 \end{aligned}
 \tag{B.8}$$

Overall heat transfer coefficient,  $U$ :

$$\begin{aligned}
 u(U) &= \sqrt{\left[\frac{\partial U}{\partial Q} u(Q)\right]^2 + \left[\frac{\partial U}{\partial A} u(A)\right]^2 + \left[\frac{\partial U}{\partial \Delta T} u(\Delta T_{lm})\right]^2} = \\
 &= U \sqrt{\left[\frac{u(Q)}{Q}\right]^2 + \left[-\frac{u(\Delta T_{lm})}{\Delta T_{lm}}\right]^2}.
 \end{aligned}
 \tag{B.9}$$

Effectiveness,  $\varepsilon$ :

$$\begin{aligned}
 u(\varepsilon) &= \sqrt{\left[\frac{\partial \varepsilon}{\partial Q_{avg}} u(Q_{avg})\right]^2 + \left[\frac{\partial \varepsilon}{\partial Q_{max}} u(Q_{max})\right]^2} = \\
 &= \varepsilon \sqrt{\left[\frac{u(Q)}{Q}\right]^2 + \left[-\frac{u(Q_{max})}{Q_{max}}\right]^2}.
 \end{aligned}
 \tag{B.10}$$

Number of transfer units,  $NTU$ :

$$\begin{aligned}
 u(NTU) &= \sqrt{\left[\frac{\partial NTU}{\partial UA} u(UA)\right]^2 + \left[\frac{\partial \varepsilon}{\partial C_{min}} u(C_{min})\right]^2} = \\
 &= NTU \sqrt{\left[\frac{u(UA)}{UA}\right]^2 + \left[-\frac{u(C_{min})}{C_{min}}\right]^2}.
 \end{aligned}
 \tag{B.11}$$

$$u(C_{min}) = C_{min} \frac{u(m)}{m}.$$

Reynolds number,  $Re$ :

$$\begin{aligned}
 u(Re) &= \sqrt{\left[\frac{\partial Re}{\partial m} u(m)\right]^2 + \left[\frac{\partial Re}{\partial d_h} u(d_h)\right]^2 + \left[\frac{\partial Re}{\partial \mu} u(\mu)\right]^2 + \left[\frac{\partial Re}{\partial A_c} u(A_c)\right]^2} = \\
 &= Re \frac{u(m)}{m}.
 \end{aligned} \tag{B.12}$$

Nusselt number,  $Nu$ :

$$\begin{aligned}
 u(Nu) &= \sqrt{\left[\frac{\partial Nu}{\partial h} u(h)\right]^2 + \left[\frac{\partial Nu}{\partial d_h} u(d_h)\right]^2 + \left[\frac{\partial Nu}{\partial k} u(k)\right]^2} = \\
 &= Nu \frac{u(h)}{h},
 \end{aligned} \tag{B.13}$$

where  $h$  is calculated considering that the hot and the cold side heat transfer coefficients in Eq. (4.3) are equal and that the thermal resistance due to conduction in the wall can be disregarded. resulting in similar uncertainties than the overall heat transfer coefficient, as shown in:

$$\begin{aligned}
 u(h) &= \sqrt{2 \left[\frac{\partial h}{\partial U} u(U)\right]^2} = \\
 &= 2 u(U).
 \end{aligned} \tag{B.14}$$

Colburn factor,  $j$ :

$$\begin{aligned}
 u(j) &= \sqrt{\left[\frac{\partial j}{\partial Nu} u(Nu)\right]^2 + \left[\frac{\partial j}{\partial Pr} u(Pr)\right]^2 + \left[\frac{\partial j}{\partial Re} u(Re)\right]^2} = \\
 &= j \sqrt{\left[\frac{u(Nu)}{Nu}\right]^2 + \left[-\frac{u(Re)}{Re}\right]^2}.
 \end{aligned}
 \tag{B.15}$$

Fanning friction factor,  $f$ :

$$\begin{aligned}
 u(f) &= \sqrt{\left[\frac{\partial f}{\partial \Delta p} u(\Delta p)\right]^2 + \left[\frac{\partial f}{\partial u_m} u(u_m)\right]^2} \\
 &= f \sqrt{\left[\frac{u(\Delta p)}{\Delta p}\right]^2 + \left[-\frac{u(u_m)}{\partial u_m}\right]^2},
 \end{aligned}
 \tag{B.16}$$

where the uncertainty on the Fanning friction factor was analyzed based on the simplified form of the heat exchanger core friction pressure drop, given by:  $f = \frac{\Delta p}{2} \frac{d_h}{L} \frac{1}{\rho u_m^2}$ .

**APPENDIX C – DBHEs inlet ports photos.**

Photos of the 90° and 144° DBHEs inlet ports with scale.



(a)



(b)

Figure 39 – Cold (a) and hot (b) inlet ports of the 90° zigzag channel DBHE.

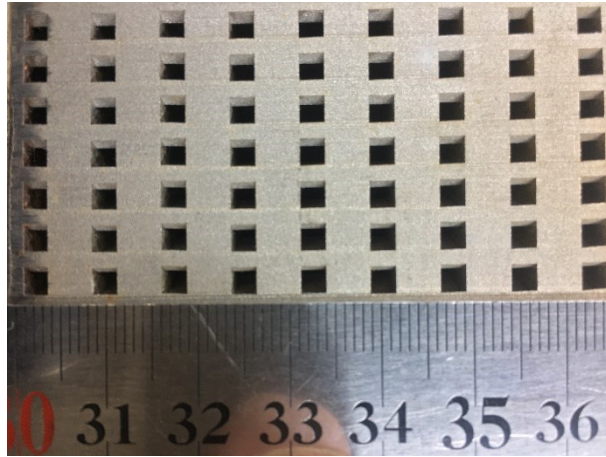


Figure 40 – Cold inlet ports of the  $144^\circ$  zigzag channel DBHE.

### ANNEX A – Experimental data DBHEs 144 and 180

The data from (Carqueja, 2017) and (Batista, 2017) for DBHEs 144 and 180 was revisited in the current work. Their experimental data is shown hereafter.

Table 14 – DBHE 144 air-water experimental data.

Set	Test	$\dot{m}_{h,in}$ , kg/s	$\dot{m}_{c,in}$ , kg/s	$T_{h,in}$ , °C	$T_{c,in}$ , °C	$T_{h,out}$ , °C	$T_{c,out}$ , °C	$\Delta P_{h,core}$ , Pa	$P_{h,out}$ , Pa	$P_{c,out}$ , Pa
1	0	8.930E-01	0.0250	69.697	27.088	69.398	69.218	1745	101325	101325
1	1	8.961E-01	0.0300	69.819	28.504	69.478	69.365	2482	101325	101325
1	2	8.945E-01	0.0355	69.836	31.525	69.428	69.200	3413	101325	101325
1	3	8.967E-01	0.0413	69.817	36.168	69.411	69.233	4509	101325	101325
1	4	8.958E-01	0.0503	69.644	42.340	69.237	69.055	6446	101325	101325
1	5	8.979E-01	0.0541	69.868	38.718	69.345	69.003	7277	101325	101325
1	6	8.979E-01	0.0587	69.920	42.218	69.412	69.060	8374	101325	101325
1	7	8.919E-01	0.0689	69.976	48.586	69.540	69.269	10998	101325	101325
2	8	1.355E+00	0.0249	69.702	27.056	69.496	69.216	1745	101325	101325
2	9	1.357E+00	0.0300	69.721	28.977	69.481	69.236	2475	101325	101325
2	10	1.353E+00	0.0355	69.742	31.955	69.481	69.218	3407	101325	101325
2	11	1.356E+00	0.0413	69.887	36.086	69.609	69.333	4511	101325	101325
2	12	1.353E+00	0.0502	69.675	42.976	69.400	69.092	6430	101325	101325
2	13	1.358E+00	0.0540	69.801	38.671	69.457	69.022	7306	101325	101325
2	14	1.355E+00	0.0586	69.659	41.991	69.326	68.910	8381	101325	101325
2	15	1.352E+00	0.0685	69.651	49.050	69.362	69.011	10977	101325	101325
3	16	8.938E-01	0.0239	79.743	25.124	79.371	79.126	1723	101325	101325
3	17	8.937E-01	0.0291	79.563	27.037	79.137	78.960	2519	101325	101325
3	18	8.942E-01	0.0348	80.043	32.486	79.564	79.382	3547	101325	101325
3	19	8.918E-01	0.0412	79.661	36.817	79.130	78.918	4806	101325	101325
3	20	8.966E-01	0.0490	79.930	42.562	79.391	79.130	6584	101325	101325
3	21	8.950E-01	0.0529	79.762	43.048	79.144	78.766	7509	101325	101325
3	22	8.966E-01	0.0575	79.648	42.800	78.987	78.569	8643	101325	101325
3	23	8.816E-01	0.0654	79.833	50.374	79.241	78.875	10735	101325	101325
4	24	1.351E+00	0.0239	79.818	25.285	79.566	79.187	1724	101325	101325
4	25	1.350E+00	0.0290	79.607	27.614	79.311	78.981	2511	101325	101325
4	26	1.352E+00	0.0350	79.758	32.375	79.430	79.108	3552	101325	101325
4	27	1.351E+00	0.0412	79.620	36.932	79.267	78.927	4804	101325	101325
4	28	1.352E+00	0.0486	79.609	41.689	79.235	78.829	6494	101325	101325
4	29	1.352E+00	0.0527	79.668	42.764	79.257	78.747	7505	101325	101325
4	30	1.353E+00	0.0574	79.519	42.691	79.085	78.530	8639	101325	101325

4	31	1.342E+00	0.0652	79.495	50.427	79.104	78.635	10734	101325	101325
---	----	-----------	--------	--------	--------	--------	--------	-------	--------	--------

Table 15 – DBHE 180 air-water experimental data.

Set	Test	$\dot{m}_{h,in}$ , kg/s	$\dot{m}_{c,in}$ , kg/s	$T_{h,in}$ , °C	$T_{c,in}$ , °C	$T_{h,out}$ , °C	$T_{c,out}$ , °C	$\Delta P_{h,core}$ , Pa	$P_{h,out}$ , Pa	$P_{c,out}$ , Pa
1	0	8.930E-01	0.0283	69.490	27.650	69.270	64.490	920	101325	101325
1	1	8.940E-01	0.0302	69.690	29.940	69.430	65.130	1062	101325	101325
1	2	8.950E-01	0.0328	69.770	30.440	69.480	65.150	1284	101325	101325
1	3	8.940E-01	0.0360	69.680	31.160	69.360	64.960	1567	101325	101325
1	4	8.940E-01	0.0391	69.720	32.230	69.410	65.030	1877	101325	101325
1	5	8.900E-01	0.0432	69.690	29.880	69.330	64.580	2291	101325	101325
1	6	8.990E-01	0.0455	69.740	33.080	69.380	64.910	2589	101325	101325
1	7	8.910E-01	0.0486	69.710	32.550	69.300	64.640	2960	101325	101325
1	8	8.990E-01	0.0515	69.820	35.720	69.430	65.070	3359	101325	101325
1	9	8.930E-01	0.0552	69.520	31.930	69.070	64.200	3789	101325	101325
1	10	8.950E-01	0.0574	69.730	35.990	69.320	64.880	4236	101325	101325
1	11	8.900E-01	0.0626	69.430	34.530	68.970	64.270	4928	101325	101325
1	12	8.980E-01	0.0652	69.700	35.640	69.240	64.520	5323	101325	101325
1	13	8.900E-01	0.0676	69.460	37.850	68.980	64.600	5749	101325	101325
1	14	8.950E-01	0.0705	69.990	37.780	69.490	64.870	6217	101325	101325
1	15	8.890E-01	0.0724	69.690	40.430	69.220	65.010	6595	101325	101325
1	16	8.950E-01	0.0757	69.590	40.300	69.100	64.800	7139	101325	101325
1	17	8.870E-01	0.0803	69.680	44.530	69.190	65.400	8065	101325	101325
2	18	1.354E+00	0.0286	69.564	24.965	69.389	64.513	931	101325	101325
2	19	1.360E+00	0.0310	69.553	25.520	69.359	64.596	1118	101325	101325
2	20	1.373E+00	0.0341	69.604	26.412	69.402	64.592	1379	101325	101325
2	21	1.359E+00	0.0374	69.422	27.398	69.195	64.378	1676	101325	101325
2	22	1.372E+00	0.0406	69.734	28.304	69.499	64.607	2007	101325	101325
1	23	1.359E+00	0.0430	69.562	29.811	69.314	64.548	2272	101325	101325
2	24	1.370E+00	0.0459	69.473	33.284	69.226	64.824	2643	101325	101325
2	25	1.357E+00	0.0479	69.433	36.049	69.188	65.074	2887	101325	101325
2	26	1.364E+00	0.0514	69.563	35.795	69.300	65.035	3357	101325	101325
2	27	1.357E+00	0.0539	69.353	35.094	69.072	64.697	3643	101325	101325
2	28	1.357E+00	0.0574	69.573	35.861	69.287	64.844	4239	101325	101325
2	29	1.358E+00	0.0610	69.365	36.675	69.062	64.674	4766	101325	101325
2	30	1.360E+00	0.0633	69.372	38.193	69.072	64.824	5124	101325	101325
2	31	1.362E+00	0.0669	69.463	39.328	69.158	64.969	5695	101325	101325
2	32	1.362E+00	0.0692	69.566	40.365	69.259	65.140	6106	101325	101325
2	33	1.362E+00	0.0718	69.522	41.573	69.215	65.218	6583	101325	101325
2	34	1.362E+00	0.0743	69.619	42.605	69.312	65.399	7033	101325	101325
2	35	1.362E+00	0.0804	69.608	46.029	69.314	65.783	8240	101325	101325
3	36	9.136E-01	0.0277	79.562	26.488	79.272	73.252	916	101325	101325
3	37	9.187E-01	0.0303	79.488	27.453	79.157	73.454	1137	101325	101325
3	38	9.196E-01	0.0337	80.017	26.970	79.650	73.635	1440	101325	101325

3	39	9.052E-01	0.0362	79.611	30.194	79.244	73.635	1697	101325	101325
3	40	9.047E-01	0.0392	79.500	31.249	79.088	73.441	2001	101325	101325
3	41	9.162E-01	0.0422	79.348	31.231	78.916	73.186	2326	101325	101325
3	42	9.129E-01	0.0449	79.714	32.224	79.230	73.336	2675	101325	101325
3	43	9.168E-01	0.0469	79.592	35.290	79.130	73.624	2938	101325	101325
3	44	9.166E-01	0.0497	79.449	36.251	79.007	73.619	3318	101325	101325
3	45	8.938E-01	0.0529	79.376	35.123	78.842	73.154	3754	101325	101325
3	46	8.844E-01	0.0570	79.267	36.554	78.700	73.073	4364	101325	101325
3	47	9.121E-01	0.0608	79.745	36.527	79.164	73.312	4974	101325	101325
3	48	9.029E-01	0.0632	79.400	37.876	78.831	73.176	5350	101325	101325
3	49	8.928E-01	0.0657	79.526	38.986	78.956	73.357	5798	101325	101325
3	50	8.856E-01	0.0683	79.680	39.800	79.053	73.390	6247	101325	101325
3	51	9.133E-01	0.0712	79.577	40.578	78.984	73.401	6800	101325	101325
3	52	9.131E-01	0.0737	79.756	40.908	79.154	73.532	7163	101325	101325
3	53	8.891E-01	0.0763	79.800	42.190	79.150	73.556	7660	101325	101325
4	54	1.374E+00	0.0277	79.325	26.607	79.122	73.191	912	101325	101325
4	55	1.370E+00	0.0304	79.407	27.409	79.181	73.524	1137	101325	101325
4	56	1.378E+00	0.0336	79.638	27.283	79.376	73.509	1428	101325	101325
4	57	1.369E+00	0.0362	79.602	30.108	79.336	73.684	1701	101325	101325
4	58	1.365E+00	0.0390	79.417	31.393	79.138	73.536	1999	101325	101325
4	59	1.378E+00	0.0421	79.376	31.281	79.073	73.327	2322	101325	101325
4	60	1.365E+00	0.0447	79.411	33.344	79.104	73.517	2646	101325	101325
4	61	1.368E+00	0.0469	79.427	35.148	79.114	73.656	2943	101325	101325
4	62	1.369E+00	0.0495	79.278	36.523	78.961	73.607	3311	101325	101325
4	63	1.367E+00	0.0530	79.248	34.456	78.890	73.169	3762	101325	101325
4	64	1.374E+00	0.0569	79.272	36.628	78.912	73.322	4376	101325	101325
4	65	1.380E+00	0.0607	79.362	36.788	78.980	73.253	4975	101325	101325
4	66	1.367E+00	0.0631	79.378	37.698	78.989	73.307	5357	101325	101325
4	67	1.363E+00	0.0656	79.345	38.968	78.951	73.352	5800	101325	101325
4	68	1.359E+00	0.0683	79.314	39.747	78.913	73.359	6251	101325	101325
4	69	1.377E+00	0.0711	79.386	40.563	78.978	73.441	6806	101325	101325
4	70	1.358E+00	0.0737	79.557	41.094	79.131	73.552	7164	101325	101325
4	71	1.321E+00	0.0762	79.428	42.358	78.998	73.540	7637	101325	101325

---